

Exploiting Nonclassical Crystallization to Tailor Molecular Diffusion in Zeolite

Catalysts

by

Heng Dai

A dissertation submitted to the Department of Chemical and Biomolecular
Engineering

Cullen College of Engineering

in partial fulfillment of the requirements for the degree of

Doctor of Philosophy

in Chemical Engineering

Chair of Committee: Dr. Jeffrey D. Rimer

Committee Member: Dr. Jeremy C. Palmer

Committee Member: Dr. Praveen Bollini

Committee Member: Dr. Allan J. Jacobson

Committee Member: Dr. Chris Nicholas

University of Houston

December 2021

Copyright 2021, Heng Dai

ACKNOWLEDGMENTS

I am very grateful for my Ph.D. advisor, Dr. Jeffrey D. Rimer, for his countless support and guidance over the last 5 years. This dissertation would have been impossible without his mentorship. Thanks Jeff for giving me the opportunity to collaborate with numerous world-leading researcher teams, making my dissertation comprehensive and diverse.

Besides my advisor, I would like to thank the rest of my committee members for evaluating my work and giving me insightful comments, Dr. Jeremy Palmer, Dr. Praveen Bollini, Dr. Allan Jacobson, and Dr. Chris Nicholas. I would also like to acknowledge my collaborators for their contributions to our work.

It has been a great pleasure to work with our wonderful research group at the University of Houston. I would like to express special thanks to our catalysis subgroup, Dr. Yufeng Shen, Dr. Yunwen Zhou, Dr. Seung Hyeok Cha, Dr. Thuy T. Le, Shilpa Kumari and Deependra Parmar for their inspiring scientific discussions.

Lastly, I would like to thank my parents, brother, and my wife for everything you have done for me. Without you, I would not be who I am today. I love you as always.

ABSTRACT

Confined channels and cages of zeolites have been widely used as shape-selective heterogeneous catalysts in the petro(chemical) industry. To develop commercial-viable zeolite catalysts, it is critical to understand the mechanism of crystallization to guide the rational design of zeolite catalysts with improved mass-transport properties. This dissertation aims to improve the catalytic performance and synthesis efficiency of zeolite catalysts by capitalizing on the fundamental understanding of zeolite crystallization mechanisms.

Nonclassical crystallization pathways involve multiple species that consist of (but are not limited to) multi-ion complexes, oligomers (or clusters), nanoparticles or liquid droplets, and nanocrystallites. Engineering zeolite materials with desired properties often requires the controlled assembly and structural evolution of colloidal precursors to tailor nucleation and growth processes. In this dissertation, we demonstrate that several quaternary amines serve as efficient zeolite growth modifiers (ZGMs) to modulate the kinetics of zeolite SSZ-13 (**CHA**) crystallization. Notably, polydiallyldimethylammonium (PDDA) was found to have the most pronounced impact on the induction period during nucleation, leading to a 4-fold reduction in crystallization time. A combination of light scattering techniques revealed that PDDA can both induce bridging flocculation of amorphous precursors and promote the precipitation of soluble silicates in a certain narrow range of polymer concentration. Thus, the overall efficiency of SSZ-13 synthesis can be improved by selecting the appropriate additives.

The small micropores of zeolite catalysts inherently suffer from severe coke formation, which impedes catalytic performance owing to internal diffusion limitations. The advent of two-dimensional, self-pillared, and hierarchical zeolites have led to materials with superior catalytic performance compared to conventional analogues; however, synthesizing zeolite crystals with sizes less than 100 nm is nontrivial, and often requires the use of complex organics with relatively low yield. In this dissertation, we discovered an alternative and versatile approach to improve the internal mass transport properties by the epitaxial growth of fin-like protrusions on seed crystals, inspired by the phenomenon of nonclassical 3-dimensional nucleation and growth on the surfaces of **MFI** zeolites. We validated this generalizable practice on two common three-dimensional frameworks (**MFI** and **MEL**) and extended the concept to a two-dimensional framework (**FER**) where it was confirmed in all cases that fins are in crystallographic registry with the underlying seeds. Molecular modeling and time-resolved acid site titration experiments of finned zeolite decoded the internal diffusion and provided more in-depth understanding to explain the remarkable improvements in mass transport (e.g., less coke and/or changes in selectivity), consistent with catalytic tests of benchmark methanol-to-hydrocarbon and 1-butene isomerization reactions showing that these unique finned structures behave as pseudo nanocrystals. This approach can be used to upgrade the performance of commercial catalysts and serve as a generalized platform for the rational design of zeolites across a broad range of framework types for diverse applications in the (petro)chemical industry.

TABLE OF CONTENTS

ACKNOWLEDGMENTS	iii
ABSTRACT.....	iv
TABLE OF CONTENTS.....	vi
LIST OF TABLES	viii
LIST OF FIGURES	ix
Chapter 1.....	1
1.1 Zeolites as Catalysts	1
1.2 Zeolite Synthesis and Growth Mechanisms	3
1.3 Zeolite Catalyst Deactivation	7
1.4 Recent Developments in Mitigating Diffusion Limitation over Zeolite ..	11
1.5 Dissertation Outline.....	16
Chapter 2.....	18
2.1 Motivation	18
2.2 Experimental Methods.....	19
2.2.1 Material	19
2.2.2 Synthesis of SSZ-13 Materials.....	20
2.2.3 Characterization	21
2.3 Results and Discussion	23
2.3.1 SSZ-13 Synthesis with Polyquatarnary Amines	23
2.3.2 Putative Arrangements of Amorphous Precursor on SSZ-13 Nucleation	29
2.4 Summary.....	34
Chapter 3.....	36
3.1 Motivation	36
3.2 Experimental Methods.....	37
3.2.1 Material	37
3.2.2 Synthesis of Finned ZSM-11 and ZSM-5 materials.....	38
3.2.3 Characterization	40
3.2.4 Catalytic Measurements	46
3.2.5 Kinetic Monte Carlo Simulation	47
3.2.6 Steered Molecular Dynamics Simulations	49

3.3 Results and Discussion	51
3.3.1 One-pot Synthesis of Finned Zeolites	51
3.3.2 Preparation of finned zeolites by secondary growth	53
3.3.3 Impact of Fins on Catalytic Performance.....	58
3.3.4 Mass-transport Properties of Finned Zeolites	61
3.4 Summary.....	65
Chapter 4.....	67
4.1 Motivation	67
4.2 Experimental Methods.....	69
4.2.1 Material	69
4.2.2 Zeolite Catalyst Preparation	70
4.2.3 Characterization	71
4.2.4 Catalytic Measurements	74
4.3 Results and Discussion	75
4.3.1 Preparation of Finned Ferrierite Zeolites	75
4.3.2 Catalytic Testing of Finned Ferrierite Catalysts	81
4.4 Summary.....	88
Chapter 5.....	90
5.1 Current Research Summary.....	90
5.2 Future Outlook.....	92
5.2.1 Hierarchical ZSM-5 Catalyst Comparison.....	92
5.2.2 Finned Zeolite with One-dimensional Pores.....	97
References.....	100
Appendix A Supplementary Information for Chapter 2.....	121
Appendix B Supplementary Information for Chapter 3	129
Appendix C Supplementary Information for Chapter 4.....	144
Appendix D Supplementary Information for Chapter 5.....	153

LIST OF TABLES

Table 3.1. Elemental analysis of zeolite catalyst samples.....	64
Table 4.1. Physicochemical properties of seed and finned H-form zeolite FER samples.....	82
Table 5.1. Physicochemical properties of nanosized and hierarchical ZSM-5 zeolites.	93
Table B1. Characterization of conventional and finned ZSM-11 samples prepared by a one-pot synthesis.....	140
Table B2. Synthesis conditions for conventional and finned ZSM-11 samples by a one-pot synthesis.....	140
Table B3. Characterization of seeds and finned ZSM-11 and ZSM-5 samples prepared by seeded synthesis.	141
Table B4. Synthesis conditions for seeds and growth solutions for finned ZSM-11 and ZSM-5 samples prepared by seeded synthesis.....	141
Table B5. Characterization of commercial and finned H-ZSM-5 catalysts.....	142
Table B6. Kinetic Monte Carlo rate constants for benzene transport in silicalite-1 at 300 K.....	142
Table B7. Kinetic Monte Carlo (kMC) simulation results for benzene transport in silicalite-1 at 300 K for seed and finned crystals with linear dimensions of $\alpha \approx 50$ nm and $\beta \approx 500$ nm.....	142
Table C1. Synthesis conditions and growth solution of seed and finned ferrierite samples prepared by seeded synthesis.	152

LIST OF FIGURES

- Figure 1.1.** Summary of synthesis approaches for nanosized zeolites. The figure is adapted from previous work(68).....4
- Figure 1.2.** Multiple pathways of crystallization. The figure is adapted from previous work(91).....6
- Figure 1.3.** Plot of the effectiveness factor η as a function of the Thiele modulus ϕ for porous materials. The effective factor η is the rate of reaction within the catalyst interior divided by the reaction rate at the external surface. The Thiele modulus ϕ is the reaction rate to diffusion rate. The figure is adapted from previous work(148)..... 13
- Figure 2.1.** (A) Modifiers of SSZ-13 crystallization: (I) TMAda, (II) PDDAM, (III) PB, (IV) EMP, (V) PDDA, and (VI) PEIM. (B and C) Crystallization times estimated from time-resolved powder XRD patterns as a function of modifier concentration for syntheses at 180 °C.25
- Figure 2.2.** (A and B) Samples extracted from a control synthesis after 36 h by (A) FE-SEM and (B) TEM. Arrows denote amorphous precursors. (C) Powder XRD patterns of samples extracted from a growth solution with 0.2 wt.% PDDA heated at 180 °C. (D) Powder XRD patterns of samples extracted from the same growth solution heated at 170 °C.....27
- Figure 2.3.** (A) Precursor size in solids extracted from growth solutions containing 0.2 wt.% PDDA (orange), 0.5 wt.% PDDA (blue), 0.2 wt.% EMP (purple), and no additive (grey). (B and C) Transmission electron micrographs (TEM) of amorphous precursors extract from a growth solution (B) without modifier and (C) with 0.5 wt.% PDDA after heating at 170 °C for 36 h.....29
- Figure 2.4.** (A) DLS measurements of colloidal silica particle hydrodynamic diameter after 5 min. (B and C) OIM studies in clear solutions prepared from soluble silica source (sodium silicate) at a molar composition of 1 Na₂SiO₃: 1760 H₂O: 0.1 TMAda with (B) 0.05 wt.% PDDA (corresponding to C_{opt}) after 30 min, and (C) 0.5 wt.% PDDA after 60 min.....30
- Figure 2.5.** Putative arrangements of amorphous precursor suspensions (left) prior to the onset of SSZ-13 nucleation at the following conditions: (i) absence of modifier (control); (ii) low modifier coverage; (iii) intermediate coverage corresponding to an optimal ZGM concentration, C_{opt}, only observed for PDDA (see Figure 2.1C); and (iv) high modifier coverage.33
- Figure 3.1.** (a) Idealized schematic of a finned zeolite with fin and interior dimensions of α and β , respectively, and fin pitch γ . (b) SEM of zeolite ZSM-11 crystals with finned surfaces prepared from a one-pot synthesis (Table B2). (c) TEM of a representative finned ZSM-11 crystal. (d) Corresponding SAED pattern of the crystal in panel C showing a single-crystal pattern behaviour. (e) High-magnification TEM image from panel c (dashed box) showing the parallel alignment of fins. (f) TOS MTH conversion for H-ZSM-11 catalysts at 350 °C with WHSV = 9 h⁻¹.53

Figure 3.2. Electron micrographs of zeolite ZSM-11 (a – c) and ZSM-5 (e – g) crystals. SAED patterns (d and h) reveal that the finned zeolites are single crystals. (i and j) TEM tomography images of finned (i) ZSM-11 and (j) ZSM-5 crystals showing cross-sectional images from Movies B2 and B3, respectively. Scale bars equal 200 nm. (k) Idealized schematic of a finned zeolite in which the fins have the same crystallographic registry as the seed. (l) Illustration of a finned zeolite that comprised of continuous channels throughout the seed (size β) and fins (size α).55

Figure 3.3. Plots of sub-complete methanol conversion over zeolite (a) H-ZSM-11 and (b) H-ZSM-5 catalysts during MTH catalysis as a function of time-on-stream (TOS). (c and d) Selectivities of hydrocarbon products for seed and finned (c) H-ZSM-11 and (d) H-ZSM-5 samples. (e) Ratio of ethylene to 2MBu (2-methylbutane and 2-methyl-2-butene) for the four set of samples. (f and g) Operando UV-Vis diffuse reflectance spectroscopy after 4 h TOS for (f) H-ZSM-11 and (g) H-ZSM-5 catalysts. (h and i) TEM images and SAED patterns of (h) Zeolyst CBV5524G and (i) the corresponding finned material prepared by secondary growth (see Figure B12 for additional images). Scale bars equal 100 nm (insets: scale bars equal 5 nm⁻¹). (j) TOS methanol conversion over as-received and finned commercial H-ZSM-5.59

Figure 3.4. (a) KMC lattice representation of the pore network for the **MFI** unit cell. (b and c) Renderings along the b direction (b) and a direction (c) showing the KMC pore network superimposed on an atomistic unit cell. (d) Log probability density distribution of the benzene diffusion path length r for a finned zeolite and a seed crystal with a cubic geometry. (e) Time-resolved titration of Brønsted acid sites for H-ZSM-11 seed and finned samples. (f) Differential plot of titrated Brønsted acid sites in Zeolyst ZSM-5 (**MFI** type) seed and finned samples and SPP zeolite. (g) TMPyr structure and a snapshot from a molecular dynamics simulation (Movie B4) showing TMPyr within a **MEL** channel. Cage hopping in MFI is observed to proceed via a similar process (Movie B5).63

Figure 4.1. (a) Idealized schematic of a finned ferrierite (**FER**) zeolite. (b) Fins located on basal (200) facets are isolated nanoparticles with pore networks disconnected from the seed crystal. (c) Illustration of a finned zeolite along a cross-sectional (200) plane with fins located on the (020) and (002) facets.76

Figure 4.2. (a) Tunable fin size on **FER** crystals. (a – d) Scanning electron micrographs of (a) seed and (b – d) finned crystals prepared at three different synthesis temperatures: (b) 120 °C (FSF1), (c) 130 °C (FSF2), and 140 °C (FSF3). Scale bars equal 500 nm. Insets: high magnification images of representative crystals. Scale bars equal 200 nm. (e) Comparison of fin size α for the three finned **FER** samples. (f) Solid state ¹H MAS NMR analysis of H-form zeolites prepared for catalyst testing.78

Figure 4.3. (a) Transmission electron micrographs of sample FSF1 along the (a) facing the sheet and (c) from the edge, respectively. SAED patterns (b and d, respectively) reveal a single crystal. (e, f) TEM tomography images of representative crystals from samples (e) FSF2 and (f) FSF3 showing cross-sectional images along the z direction (see Movies C2 and C3, respectively). Scale bars equal 500 nm unless otherwise denoted.80

Figure 4.4. (a) Reaction of 1-butene to isobutene and byproducts (propene, pentene, etc.). (b) Comparison of turnover number (units of $molCmolH^{-1}h^{-1}$) for the seed (FS, gray) and finned (FSF1, FSF2, and FSF3) catalysts in the isomerization reaction at subcomplete conversion of 1-butene ($\leq 60\%$). Reactions were performed at $400\text{ }^{\circ}\text{C}$ with $WHSV = 12\text{ h}^{-1}$ (evaluated between $45 - 55\%$ conversion, Figure C10). (c) Corresponding isobutene selectivity for each catalyst (evaluated at 50% 1-butene conversion). The complete product selectivity distribution is provided in Figure C11.84

Figure A1. Powder X-ray diffraction patterns of SSZ-13 syntheses at $180\text{ }^{\circ}\text{C}$ with the following modifiers: (A) PDDAM, (B) PB, (C) PEIM, (D) EMP, and (E) BMP. 121

Figure A2. SSZ-13 crystallization time as a function of TMAda concentration for syntheses at $180\text{ }^{\circ}\text{C}$. The gel composition is $0.052\text{ Al(OH)}_3 : 1\text{ SiO}_2 : 0.2\text{ NaOH} : 44\text{ H}_2\text{O} : (0.1+x)\text{ TMAda} : x\text{ HCl}$ where x is the increased molar concentration of TMAda and/or HCl compared with the control. 121

Figure A3. Powder X-ray diffraction patterns of SSZ-13 syntheses at $180\text{ }^{\circ}\text{C}$ with the following modifiers: (A) PDDAM, (B) PB, (C) PEIM, (D) EMP, and (E) BMP. 122

Figure A4. Powder X-ray diffraction patterns of SSZ-13 syntheses with PDDA at $180\text{ }^{\circ}\text{C}$ ranging (A) from $0.05\text{wt}\%$ to $0.3\text{wt}\%$ and (B) from $0.35\text{wt}\%$ to $1.6\text{wt}\%$ 122

Figure A5. Scanning electron micrographs (SEM) of a partially crystalline SSZ-13 sample taken after 42 h of heating at $180\text{ }^{\circ}\text{C}$. The images are replotted from the previous literature.⁽⁹⁶⁾ 123

Figure A6. (A) Transmission electron micrographs (TEM) of a partially crystalline SSZ-13 sample taken after 42 h of heating at $180\text{ }^{\circ}\text{C}$. Two population regions were found: (i) spheroidal crystals and (ii) WLP precursors. Selected area electron diffraction (SAED) patterns of regions i and ii in panel (A) demonstrate that (B) WLP precursors are amorphous and (C) spheroidal particles are crystalline, respectively. The images are replotted from the previous literature.⁶ 123

Figure A7. Powder X-ray diffraction patterns of samples extracted from a growth solution in the absence of additives at $180\text{ }^{\circ}\text{C}$ from periodic times: 30, 36, 42, 44 and 144 h. 124

Figure A8. Powder X-ray diffraction patterns of samples extracted from a growth solution (A) in the absence of additives and (B) in the presence of PDDA with $0.5\text{ wt}\%$ heating at $170\text{ }^{\circ}\text{C}$ 124

Figure A9. Relationship between SSZ-13 crystallization time and PDDA concentration at $180\text{ }^{\circ}\text{C}$ using an alternative silicon source (LUDOX AS-40). 125

Figure A10. SSZ-13 crystallization time as a function of PDDA (450 kDa) concentration for syntheses at $180\text{ }^{\circ}\text{C}$ using fumed silica as the silicon source. 125

Figure A11. Liquid ^1H NMR spectrum (A) before and (B) after hydrothermal treatment using D_2O as solvent. PDDA was mixed with DI water to obtain a solution with similar pH as the synthesis condition and heated at $180\text{ }^\circ\text{C}$ for 1 day.....	126
Figure A12. TEM images of SSZ-13 crystals prepared at $170\text{ }^\circ\text{C}$ using the following concentrations of additives: (A) 0wt% for 6 h; (B) 0wt% for 24 h; (C) 0.2wt% EMP for 6 h; (D) 0.2wt% EMP for 22.5 h; (E) 0.2wt% PDDA for 12 h; (F) 0.2wt% PDDA for 13 h; (G) 0.5wt% PDDA for 24h. All scale bars equal to 100 nm.....	126
Figure A13. Elemental analysis of extracted solids using inductively coupled plasma-optical emission spectrometry (ICP-OES) for syntheses at $170\text{ }^\circ\text{C}$	127
Figure A14. (A) Dynamic light scattering (DLS) measurements of colloidal silica particle size with different concentrations of polymer (PDDAM, PB and PEIM) or monomer (EMP). (B) Table for the overlapping data (PEIM, PB, and EMP) in panel A that exhibit no appreciable change in hydrodynamic diameter with increasing modifier concentration.....	127
Figure B1. Scanning electron micrographs of conventional zeolite H-ZSM-11 samples listed in Table B1 with different crystal sizes: (A) MEL-C ₁ , (B) MEL-C ₂ , and (C) MEL-C ₃ , respectively.	129
Figure B2. Nitrogen adsorption/desorption isotherm for the finned ZSM-11 sample prepared by a one-pot synthesis (sample MEL-F ₁ in Table B1).....	129
Figure B3. Transmission electron microscopy (TEM) tomography reveals the presence of isolated mesopores within the interior of finned ZSM-11 particles prepared via a one-pot synthesis (sample MEL-F ₁).....	130
Figure B4. (A) Scanning electron microscopy (SEM) shows a typical “blackberry” morphology of MFI aggregates. (B) Transmission electron microscopy (TEM) shows clusters of small nanoparticles. (C) SAED pattern of a particle from the one-pot MFI synthesis reveals a polycrystalline sample. (D) An idealized scheme of a blackberry zeolite where the lines indicate crystallographic orientation.	130
Figure B5. Powder X-ray diffraction patterns show that all as-synthesized ZSM-11 samples prepared for catalytic testing are fully crystalline.....	131
Figure B6. Powder X-ray diffraction patterns show that all as-synthesized ZSM-5 samples prepared for catalytic testing are fully crystalline.....	131
Figure B7. N_2 sorption isotherms for seed (black) and finned (red) samples of (A) H-ZSM-11 and (B) H-ZSM-5 catalysts. Each finned sample was prepared by seeded synthesis.....	132
Figure B8. Calculated percent increase in specific surface area for finned zeolites compared to their original seeds as a function of seed crystal size, β . The relative increase in specific area is reported for four cases of varying fin size α and pitch γ along with the total number of fins per seed surface area, N	132

Figure B9. Solid state ^{27}Al NMR analysis for seed (black) and finned (red) samples of zeolite (A) H-ZSM-11 and (B) H-ZSM-5 catalysts. Each finned sample was prepared by seeded synthesis.	133
Figure B10. The results of methanol-to-hydrocarbon (MTH) reactions showing the product selectivities (bar graphs, left y-axes) and methanol conversion (red circles, right y-axes) as a function of time on stream (TOS) for the following H-form zeolites: (A) MEL-Seed, (B) MEL-Finned, (C) MFI-Seed, and (D) MFI-Finned. All reactions were performed at a weight hourly space velocity of 20 h^{-1}	133
Figure B11. Operando UV-Vis diffuse reflectance spectroscopy data within 3 min TOS for zeolites (A) MEL-Seed, (B) MFI-Seed, (C) MEL-Finned, and (D) MFI-Finned. The spectra were measured in 30 s intervals.	134
Figure B12. Scanning electron microscopy (SEM) images of (A) commercial H-ZSM-5 (Zeolyst CBV 5524G) and (B) the corresponding finned H-ZSM-5 sample prepared by secondary growth.	134
Figure B13. The results of methanol-to-hydrocarbon (MTH) reactions showing the product selectivities (bar graphs, left y-axes) and methanol conversion (red circles, right y-axes) as a function of time-on-stream (TOS) for the following H-form zeolites: (A) Zeolyst and (B) Finned Zeolyst. All reactions were performed at a weight hourly space velocity of 9 h^{-1}	135
Figure B14. Simplified schematic of FTIR spectroscopy where 2,4,6-trimethylpyridinium is constantly flowed into the cell to be dosed onto the catalyst sample.	135
Figure B15. (A) Raw FTIR spectra of a catalyst sample highlighting peaks of interest. The percentage of Brønsted acid sites titrated corresponds to integration of 1565 cm^{-1} peak areas. (B) Temporal changes in the FTIR spectra showing an increased peak area at 1565 cm^{-1} over time.	136
Figure B16. Parity plot showing loss of Brønsted acid sites (BAS) is linearly correlated to the increase in 2,4,6-trimethylpyridinium ions. The parameters A_x and $A_{x,0}$ are peak areas of the FTIR spectra at a particular time and the initial time, respectively, where $x = 1565\text{ cm}^{-1}$ for TMPyr-occupied BAS and $x = 3605\text{ cm}^{-1}$ for vacant BAS.	136
Figure B17. Time-resolved titration of Brønsted acid sites for (A) H-ZSM-5 seed/finned samples and (B) Zeolyst (CBV 5524G)/finned Zeolyst samples.	137
Figure B18. Differential plot of titrated Brønsted acid sites in (A) H-ZSM-11 seed/finned samples and (B) H-ZSM-5 seed/finned samples.	137
Figure B19. Snapshot from an SMD simulation (Supplementary Video B5) showing TMPyr within a MFI channel.	138
Figure B20. Uptake data of (A) MEL-Seed, (B) MFI-Seed, (C) MEL-Finned and (D) MFI-Finned from Brønsted acid site (BAS) titrations by 2,4,6-trimethylpyridine for two separate runs indicating run-to-run repeatability.	138

Figure B21. (A) Time-resolved Brønsted acid sites titrated in the MEL-Seed and MEL-Finned samples for two separate runs. (B) Derivative of Brønsted acid sites titrated for the MEL-Finned sample, with colors corresponding to the plots in panel A. 139

Figure C1. Powder X-ray diffraction patterns of all as-synthesized ferrierite zeolite samples (see Table S1 for synthesis conditions and Table 4.1 in the manuscript for physicochemical properties of each sample). 144

Figure C2. Nitrogen adsorption/desorption isotherms for the seed (FS) and corresponding finned ferrierite samples (FSF1, FSF2, and FSF3). 144

Figure C3. TEM images of sample FS viewed (a) facing the sheet (normal to the [100] direction) and (c) from the edge. (b and d) SAED patterns of respective images. 145

Figure C4. Electron diffraction patterns of (a) a^* , (b) b^* and (c) c^* direction, (d) (hk1), (e) (h1l), (f) (1kl), (g) (hk0), (h) (h0l) and (i) (0kl) face confirm the *Immm* space group of the FER framework for the FS sample. The corresponding unit cell parameter is $a = 19.11 \text{ \AA}$, $b = 14.45 \text{ \AA}$, $c = 7.40 \text{ \AA}$, $\alpha = 90.4^\circ$, $\beta = 89.5^\circ$, $\gamma = 89.5^\circ$. See Movie C4 for the 3D electron diffraction. 145

Figure C5. TEM images of sample FSF2 in two orientations: (a) facing the sheet (normal to the [100] direction); and (c) from the edge. SAED patterns of respective images (b, d) reveal that FSF2 is a single crystal. 146

Figure C6. TEM images of sample FSF3 in two orientations: (a) facing the sheet (normal to the [100] direction); and (c) from the edge. SAED patterns of respective images (b and d) reveal that FSF3 is a single crystal. 146

Figure C7. Scanning electron micrographs of samples (a) FC and (b) corresponding finned FCF. 146

Figure C8. (a) Transmission electron micrograph of FCF. SAED patterns of respective images (b) reveal that FCF is a single crystal. 147

Figure C9. Solid state ^{27}Al MAS NMR analysis for samples (a) FS, (b) FSF1, (c) FSF2, (d) FSF3, (e) FC, and (f) FCF. See Table C1 for synthesis conditions and Table 4.1 for physicochemical properties of each sample (including the analysis of extra-framework Al species from these spectra). 147

Figure C10. Conversion of 1-butene as a function of time on stream (TOS) for the seed (FS, square symbols) and finned ferrierite samples (FSF1, FSF2, and FSF3). . 148

Figure C11. The results of isomerization of 1-butene reaction showing the product selectivities (bar graphs, left y-axes) and 1-butene conversion (red circles, right y-axes) as a function of time on stream (TOS) for the following H-form catalysts: (a) FS, (b) FSF1, (c) FSF2, (d) FSF3, (e) FC, and (f) FCF. 148

Figure C12. Titration of Brønsted acid sites (BAS) by 2,3-dimethylpyridine in sample FS over time. Three runs were performed to assess the reproducibility of the technique measured BAS titration within 2.5% error.	149
Figure C13. Derivative of Brønsted acid sites (BAS) titration by 2,3-dimethylpyridine on FSF2 over time, normalized by each run's respective peak at fast time-scale (τ_{fp}). Technique reproducibly measures τ_{fp} within 1.2% error.	149
Figure C14. Derivative of Brønsted acid sites (BAS) titration by 2,3-dimethylpyridine over time. The area under the peaks represents the cumulative amount of Brønsted acid sites titrated at different time points, with the first peak's maxima indicated by τ_{fp} , or peak at fast time-scale. The derivative plot was obtained via the following procedure - fitting smoothing spline function over BAS titration over time, taking discrete derivative between each point, fitting the derivative plot with peak fitting function in MATLAB.	150
Figure C15. (a) Titration of Brønsted acid sites (BAS) by 2,3-dimethylpyridine in seed and finned ferrierite samples (FS, FSF1, FSF2 and FSF3) over time. (b) Derivative of BAS titration.	150
Figure C16. (a) Titration of Brønsted acid sites (BAS) by 2,3-dimethylpyridine in FC and FCF over time. (b) Derivative of BAS titration.	151
Figure C17. Absolute and relative peak areas of BAS titrated in fins and bulk catalyst. Technique reproducibly measures percentage of BAS uptake within 0.25% error. Error bars were computed from the sampling of three separate runs of different samples from the same synthesis batch.	151
Figure D1. ^{27}Al MAS NMR of (a) Al-FDP (5), (b) Al-FDP (5)-A-1d, and (c) Al-FDP (5)-A-3d. Note that samples (b) and (c) are post-annealed for 1 and 3 days respectively. The intensity of resonance assigned to extra-framework Al species at ca. 0 ppm decreased after annealing, indicating the depletion of extra-framework Al species.	153

Chapter 1

Zeolite Crystallization and Catalytic Applications

1.1 Zeolites as Catalysts

Zeolites (or zeotypes) are crystalline, nanoporous material with confined channels and cages built up from XO_4 tetrahedra framework coordinated by oxygen bridges, where X can be trivalent (e.g., Al, B, Ga), tetravalent (e.g., Ge, Si), or pentavalent (e.g., P) (1–4). The origin of name *zeolite* traces back to 1756, when the Swedish chemist Axel Fredrik Cronstedt noticed mineral stilbite appeared to boil upon heating and named it as “boiling stone” or zeolites. In the 1950s, synthetic zeolites started drawing much attention as industrial adsorbent and catalysts after Linde Type A zeolite (LTA) was first discovered(5). To date, 253 zeolite framework has been successfully synthesized and each of them is documented with a 3-letter code determined by the International Zeolite Association (IZA)(6). Synthetic zeolites have been extended to systems beyond aluminosilicates. This zeotype family includes aluminophosphates (AlPO), silicoaluminophosphates (SAPO), or metal-substituted aluminophosphate (MeAPO)(2, 4, 7). In a conventional synthesis, the substitution of Si with Al as one tetrahedral (T) site creates a negative charge on the neighboring oxygens, which is counterbalanced by an extra-framework cation such as an alkali or alkaline earth metal (e.g., Na^+ , K^+ , Mg^{2+} , Ca^{2+} , Sr^{2+}) or the cations of organic structure-directing agents (OSDAs). The as-synthesized zeolite can be ion-exchanged into proton-form or metal-form, inducing Brønsted acid sites (BAS) or Lewis acid sites (LAS), respectively. The unique acid site chemical environment (e.g., proton, Ag (I), Ga (III), and Zn (II)) or the

combination of two acid site types (Brønsted and/or Lewis acid sites) make zeolites versatile catalysts with tunable acidity(8).

Zeolites also have unique porosity and size/shape selectivity, which can be utilized in diverse catalytic applications. Micropore size and pore/channel connectivity make each zeolite framework unique in crystal topology. Almost all zeolites are comprised of micropore openings, which can be categorized as small-pore (8-ring, ca. 4. Å), medium-pore (10-ring, ca. 5-6 Å), large-pore (12-ring, ca. 7Å) and extra-large pore (> 12-ring). Corma and coworkers discovered a series of ITQ-series extra-large pore zeolites up to 30 membered-rings (e.g., ITQ-37), expanding the zeolite family and emerging application for catalysis and adsorption(9–14). Zeolites exhibit pore networks with one-dimensional (1D), 2-dimensional (2D), or 3-dimensional (3D) channels. The size/shape of the cages and/or the cavities between the intersections of the channels endow zeolites with unique shape selectivity towards reactants, products or transition states(8, 15, 16).

Tunable solid acidity, unique porosity, and shape selectivity, along with excellent (thermo)stability and large surface area make zeolites ideal candidates for many applications, such as adsorption, selective separation, catalysis, sensor technologies, and biomedical devices(17–26). Among the known zeolite structures, on the order of 20 are reported to be used in commercial applications (e.g., catalyst, adsorption, ion exchange)(27). This dissertation focuses on the applications of zeolites in catalysis. Catalysts are defined as compounds that speed up the reaction rate(s) of chemical reactions by reducing the activation barrier(s) of the elementary reaction steps without any mass consumption(28). Catalysts can be divided into two classes: homogeneous

and heterogeneous. Homogeneous catalysts occupy the same phase as the reaction mixture (e.g., typically in liquid phase), while heterogeneous catalysts are not in the same phase as the reactants and products. One advantage of heterogeneous catalysts is facile recycling, which empower them to be heavily used in many chemical and energy industries. One of the most common heterogeneous catalysts is zeolite-based materials, which have been extensively used in refining (e.g., fluid catalytic cracking (FCC)(29–32), naphtha isomerization(33, 34), and dewaxing(35, 36)), petrochemical (e.g., ethylbenzene(37, 38) and xylene isomerization(39, 40)) and chemical processes (e.g., amination(41) and acylation(42)). The discovery of zeolite USY (FAU based) catalyst in FCC processes, which replaced amorphous silica-alumina catalysts, was indeed a revolution in the refinery industry, as it accounts for 95% of large-scale zeolite synthesis(29). In addition to these traditional catalytic applications, zeolites have been extensively studied in applications including bio-based conversion(43–46), selective catalytic reduction (SCR) in vehicle emission control(47–49), and methanol-to-hydrocarbon (MTH) reactions(50-67).

1.2 Zeolite Synthesis and Growth Mechanisms

Zeolite preparation usually involve treating certain synthesis mixtures at elevated temperature and autogenous pressure, which is referred as hydrothermal synthesis. The crystallization process begins from an aluminosilicate hydrogel under the combined action of a mineralizing agent (e.g., OH⁻ or F⁻) and structure-directing agent (SDA). One of the prevailing challenges in zeolite science is controlling crystallization to achieve desired physicochemical properties of the final product. Syntheses of nanosized zeolites have been extensively investigated because of their enhanced external surface

area, which is beneficial for catalysis and adsorption applications(22, 36, 51, 68). As summarized in Figure 1.1, conventional hydrothermal syntheses involve several scenarios, such as organic-templated synthesis(69, 70), organic-template-free synthesis(71–73), dry-gel conversion(74–76) and seed-assisted synthesis(76–78). One of the key parameters to generate nanosized zeolite crystallites is low temperature. Typically, a decrease in synthesis temperature favors nucleation over crystal growth without a high degree of Ostwald ripening, leading to sufficiently abundant nuclei during the crystallization process(79). In addition to conventional hydrothermal syntheses, alternative approaches have been recently studied, which include (but are not limited to) microwave and sonication synthesis,(80) ionothermal synthesis(70, 81) and confined synthesis(82–84). Also, many research groups have explored alternative synthesis approaches, such as free-radical assisted synthesis(85, 86), pressure-induced transformation(87, 88), and mechanochemical synthesis(89). Examples of high-pressure synthesis include the work of Wakihara and co-workers(88) who successfully synthesized nanosized **EMT** and **FAU** zeolites under 20 and 400 MPa pressure, respectively, within 1 h synthesis time.

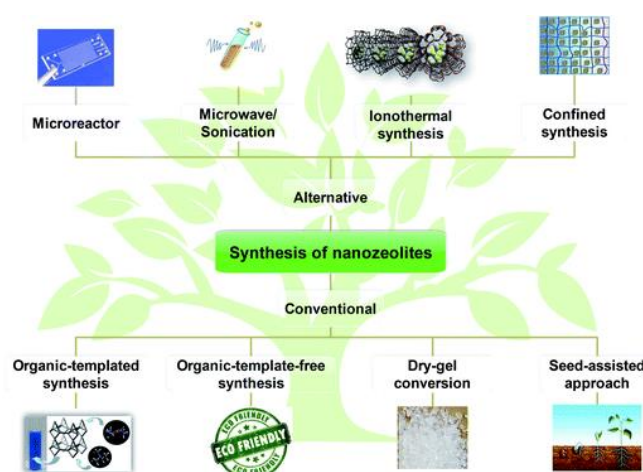


Figure 1.1. Summary of synthesis approaches for nanosized zeolites. The figure is adapted from previous work(68).

Although numerous nanosized zeolite materials have been synthesized, the lack of deep understanding of fundamental crystallization mechanisms often renders unwanted properties of the final product. Rational design of zeolite materials without a *priori* knowledge of nucleation and growth mechanisms is nontrivial owing to their complicated growth involving a combination of classical and nonclassical pathways. As shown in Figure 1.2, numerous pathways of crystal growth can occur. Classical growth involves the addition of solute (monomer) from solution to a crystal surface, which is often depicted as a model Kossel crystal(90). Monomers attach to the kinks, steps or terraces on crystal facets. Nonclassical mechanisms of crystallization differ from the classical routes owing to the physical state of the solute in the solution, which comprises a diverse range of precursors as growth units: oligomers, liquid droplets, amorphous colloidal particles, and nanocrystals(91). Crystallization by particle attachment (CPA) involves structural transformations of amorphous precursors as they attach and integrate into crystal surfaces(92–94). It is common to observe colloidal particles (1 – 100 nm) and/or large aggregates (micron sizes), referred as *worm-like particles* (WLPs)(95), which is a term was first introduced in 1990. In some cases, the combination of both classical and nonclassical growth routes makes zeolite synthesis even more complicated. Previous studies on both **MFI** and **CHA** zeolites(96, 97) by *in situ* atomic force microscopy (AFM) measurements elucidate that classical and nonclassical growths occur simultaneously at near molecular resolution, although the impact of individual contribution of each route on the physicochemical properties of the final crystals remains elusive.

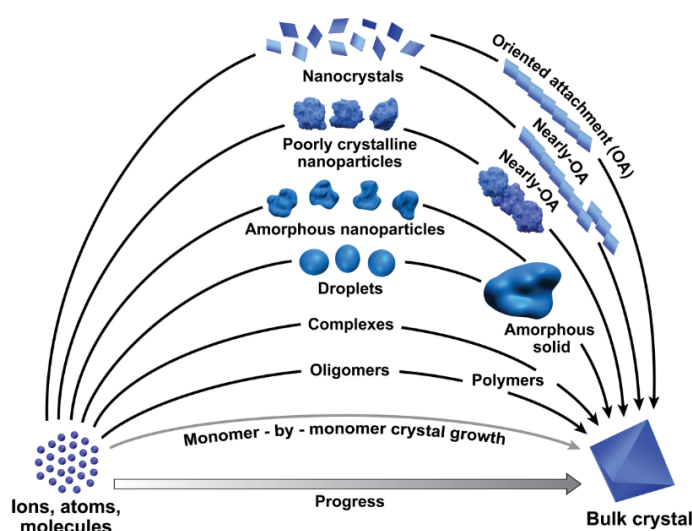


Figure 1.2. Multiple pathways of crystallization. The figure is adapted from previous work(91).

Engineering zeolite crystal habit (e.g., crystal size and morphology), chemical composition, acid site location and strength, and porosity play crucial roles in tailoring catalytic performance. One effective way of tailoring zeolite crystal properties is through the use of zeolite growth modifiers (ZGMs), which are (macro)molecular additives that alter anisotropic rates of crystallization by either inhibiting or promoting crystal growth via preferential binding to crystal facets, altering solubility by forming complexes, or manipulating the structural evolution of precursors. ZGMs have been demonstrated for many zeolites or zeotypes, such as **MFI** (silicalite-1)(98–100), **CHA** (SSZ-13, SAPO-34)(96, 101), **AEI** (SAPO-11)(102), **LTL** (zeolite L)(103–105), **FAU** (zeolite Y)(106), **IWR** (ECNU-20)(107), and **MTW** (ZSM-12)(108). Ions, molecules and macromolecules (e.g., polymers(109, 110), proteins(111), peptides(112, 113) and peptoids(103)) can all function as growth modifiers. The nature of modifier-crystal interactions involves (but is not limited to) van der Waals, electrostatic, hydrogen bonding, and $\pi - \pi$ stacking(114). This dissertation focuses on the effect of several

polyquatarnary amines as efficient accelerants of zeolite SSZ-13 (**CHA**) crystallization, which will be discussed in Chapter 2.

1.3 Zeolite Catalyst Deactivation

Catalyst deactivation is commonly defined as the loss of catalytic activity and/or selectivity over time(115–118). Bartholomew et al. summarized several intrinsic mechanisms of catalyst deactivation(115). Poisoning, vapor formation, vapor-solid and solid-solid reactions are chemical in nature, while fouling and attrition are mechanical types. Another type of catalyst deactivation is associated with thermal degradation over time. Catalyst deactivation is a ubiquitous problem in industrial processes owing to the additional cost of catalyst replacement and net loss of process shutdown(116). Porous materials (e.g., zeolites) are highly prone to catalyst deactivation, which often hinders zeolite-based technology implementation at the industrial scale. Poisoning is one deactivation mechanism for zeolite catalysts due to the strong chemisorption of sulfur impurities and/or metal contaminants (e.g., V, Cu and Ni) in the feedstock. Sintering is common for metal-based zeolite catalysts, leading to the migration and loss of acid strength of the metal phase(118). In addition to poisoning and sintering, coke formation has been extensively studied in the literature as it is one of the most common deactivation mechanisms for zeolite catalysts(119–124). Graphitic carbonaceous compounds can easily accumulate on external surfaces of zeolite particles, resulting in pore blockage and the inaccessibility to reactants. Moreover, due to the high BAS affinity of the coke species, internal micropore and BAS may be also blocked or permanently covered under reaction conditions. Previous studies have shown that coke formation is impacted by zeolite acidity and pore topology(125). The coke formation

rate is over 50 times lower on small and medium pore zeolites than on those with large pores(126).

MTH catalysis is one of the most important reactions in C₁ chemistry since this technology bridges ample and renewable nonfossil sources such as coal, biomass and natural gas to profitable petrochemical products such as ethene, propene, gasoline and aromatics. The MTH process was first initiated by Chang et al. at Mobil in the 1970s during the study of methanol and isobutane alkylation reactions over ZSM-5 (**MFI**) zeolite catalysts(127). In 1985, Union Carbide Corporation (UCC) discovered a new zeolite silicoaluminophosphate, SAPO-34, with small pore chabazite (**CHA**) topology, leading to exceptional light olefin (ethene and propene) selectivity(2). Depending on the product selectivity, MTH can be categorized as methanol-to-olefin (MTO) and methanol-to-gasoline (MTG). The first commercialization of the MTO reaction, DMTO technology, was successfully implemented by the Dalian Institute of Chemical Physics (DICP) in 2006(128, 129). To date, ZSM-5 and SAPO-34 are the two most important commercial zeolite catalysts for MTH processes. Elucidating the structure-performance relationship of zeolites in the MTH reaction has been the subject of numerous studies over the last thirty years(50, 59, 62, 130, 131). For instance, SAPO-34 with isolated Si sites favors higher light olefin selectivity(132). Also, isomorphous substitution of metal heteroatoms in SAPO-34 has been reported by Liu and coworkers wherein CoSAPO-34 showed light olefin selectivity as high as 93%(133). Bhan and coworkers found for ZSM-5 (**MFI**) that light olefin selectivity can be enhanced with increased crystal size due to the long residence time of methylbenzene, thus shifting the olefin cycle to the aromatic cycle(134, 135).

In addition to the rational design of zeolite catalysts in MTH, much effort has been devoted to the mechanistic study of methanol conversion(57, 136–138). The autocatalytic dual-cycle hydrocarbon pool mechanism is generally accepted wherein olefins undergo methylation and cracking in the olefin cycle, and aromatics undergo methylation and dealkylation reactions in the aromatics cycle, interconnected via hydrogen transfer reactions in the propagation phase. Although extensively studied, the initiation phase involving the formation of the first C-C bond remains elusive(139). It has been reported that polycyclic aromatic hydrocarbons induced by a formaldehyde intermediate terminate the chain carrier(55, 140–142). Deactivation in MTH reactions has been a hot topic in both academia and industry. As discussed previously, coke formation is one of the main outcomes for MTH catalyst deactivation. Due to the nature of the MTH chain carrier mechanism, the hydrocarbon pool (HCP) species (e.g., methylbenzene) can act as co-catalysts that facilitate the conversion rate. However, some small polyaromatics that are too large to diffuse out of the zeolite lead to pore blockage of the internal acid sites, although they are sufficiently large to fit within the pores. Also, large polyaromatics, referred as external coke, are associated with pore blockage at the external surface of the zeolite catalyst. Interestingly, a certain hydrocarbon can either be an active species in one zeolite topology or the deactivation species in another zeolite framework. For instance, in the MTH reaction, polymethylbenzenes, which are active cocatalysts in ZSM-5 zeolite, can cause the catalyst deactivation in ZSM-22 zeolite because the transition states of the polymethylbenzenes are highly restricted by the channel intersection in ZSM-22(125).

Deactivation is commonly associated with catalyst stability (or lifetime), which is one of the key parameters of catalyst performance evaluation. Zeolite Catalyst can

deactivate either by the loss of intrinsic activity per acid site or a decrease in the number of active sites, or pore inaccessibility to the acid sites. Also, deactivation is a kinetic phenomenon, which needs to be studied in a kinetically controlled environment. Although there has been extensive experimental effort to decipher the deactivation mechanism of this complicated series of reactions, modeling or directly monitoring the deactivation behavior is challenging. First, operating the catalytic reaction at full conversion is a common pitfall of evaluating deactivation. Haw and coworkers introduced a deactivation model of the so-called “burning cigar” in a fixed bed reactor(143). In this concept, a band of fresh catalyst bed moves from topside to downside once the cigar is lighted (i.e., activated). In this way, running the reaction at full conversion only reflects a portion of catalytic activity and the catalyst can in fact be much more active. Consequently, assessing the deactivation (or stability) at sub-complete conversion becomes more reliable to avoid conflation of activity and stability. Many researchers often use the rate of change of chemical conversion (X) with time-on-stream (TOS) as the deactivation rate ($\frac{dX}{dt}$). However, the deactivation rate is referred as ($\frac{d\tau}{dt}$), where the value of ($\frac{dX}{dt}$) conflates both reaction kinetics and deactivation rate. Janssen applied the following equations in the analysis of conversion with time-on-stream data as (144)

$$\frac{dX}{d\tau} = k(1 - X) \quad (1)$$

$$\text{and } \frac{d\tau}{dt} = -aX, \quad (2)$$

where X is conversion, k is a first-order rate constant of reaction, τ is the contact time, and a is the deactivation coefficient. This analysis is based on the hypothesis that MTH is a first-order reaction and the deactivation rate is proportional to the conversion.

Based on these assumptions, the subsequent analysis deduced a descriptor $t_{0.5} \approx \frac{\tau_0}{a}$, where $t_{0.5}$ is the lifetime to the 50% conversion level and τ_0 is the initial contact time. The descriptor can easily calculate the deactivation rate a since it only contains the initial contact time τ_0 instead of activity in the equation; however, these simple assumptions may not be valid, especially in systems with as much complexity as MTH. Recently, Bhan and coworker(64) developed an analytic formalism, *site-loss* yield $-\frac{d\tau}{dt}$, to evaluate the nonselective deactivation in fixed bed reactors, which is common to many zeolites/zeotypes (e.g., ZSM-5, ZSM-22, ZSM-23, and SAPO-5)(145, 146). Furthermore, when it comes to selective deactivation, cumulative *site-loss* yield can be used to assess catalyst deactivation. The same group used this numerical assessor to evaluate the deactivation pathways mediated by formaldehyde in MTH reactions, showing that polyunsaturated non-aromatic species could be another possible deactivation pathway besides polyaromatic species(147).

1.4 Recent Developments in Mitigating Diffusion Limitation over Zeolite

As previously mentioned, zeolites impose intraparticle transport constraints in many industrial applications due to their inherent micropores (apertures ≤ 1 nm). As shown in Figure 1.3, a high value in the Thiele modulus ϕ exhibits low effectiveness factor η (low utilized catalyst volume) for porous materials. Approaches to shorten the diffusion length and/or enhance effective diffusivity are routinely used to improve the effectiveness factor of zeolite catalysts. Recently, Rimer and coworkers reviewed the recent progress in the rational design of crystalline catalysts with reduced diffusion limitations(148). Synthesis of nanosized zeolites is one of the typical methods to reduce mass transport limitations. Mintova and coworkers discovered nanosized FAU and

EMT zeolites (crystal size less than 20 nm) by a low-temperature aging approach(149, 150). Additional synthesis parameters (e.g. molar composition, synthesis temperature and time) have also been thoroughly studied to tailor the zeolite crystal size. Notable examples of engineering crystal size and morphology have been developed by Rimer and coworkers using ZGMs (see Section 2 above)(96, 98, 103, 104, 145). Moreover, the discovery of new frameworks, such as extra-large pore zeolites, has resulted in much progress in recent years. Corma and coworkers reported a series of extra-large pore zeolites (e.g., ITQ-54, ITQ-43, and ITQ-33), which showed potential for catalysis, gas separations, and ion exchange applications(10, 13). The zeolite ITQ-37 with a pore opening of 30 MR (about 2 nm) considerably enhances the diffusivity while maintaining shape selectivity(10). Recently, there is a growing surge in the synthesis of two-dimensional (2D) zeolites, which are ultrathin nanocrystals with dimensions less than 5 nm(151–155). Ryoo and coworkers successfully synthesized 2D MFI nanosheets by the use of surfactant-like SDAs (e.g., di-quaternary ammonium-type)(154). Apart from conventional hydrothermal syntheses, 2D zeolites can be generated from two-dimensional layered zeolite precursors (LZP). To date, thirteen zeolite framework types are able to be synthesized from a layered precursor (e.g., **FER**, **SOD**, **MFI**, **PCR**)(156–159). Each layer of the 2D LZP is interconnected by weak hydrogen bonding, contrary to covalent bonding in 3D zeolites. A striking example of progress in the synthesis of 2D zeolites is MCM-22 (**MWW**). MWW zeolite can be made in the traditional method as a 3D zeolite, referred to as MCM-49 or LZP MCM-22P. Various post-treatment methods (e.g., swelling, pillaring, delaminated swollen precursor) have produced disparate 2D MWW materials, such as MCM-36, MCM-56, and ITQ-2(152, 160, 161). Recently, Rimer and coworkers reported a new 2D **MWW** zeolite via a one-pot

synthesis, thereby eliminating the need for multiple steps(153). This ultrathin 2D nanosheets with an average thickness of 3.5 nm was synthesized with a commercial surfactant, cetyltrimethylammonium (CTA), as both an in situ exfoliating agent and OSDA. The resulting material exhibited improved properties and catalytic performance compared to ITQ-2 and MCM-22.

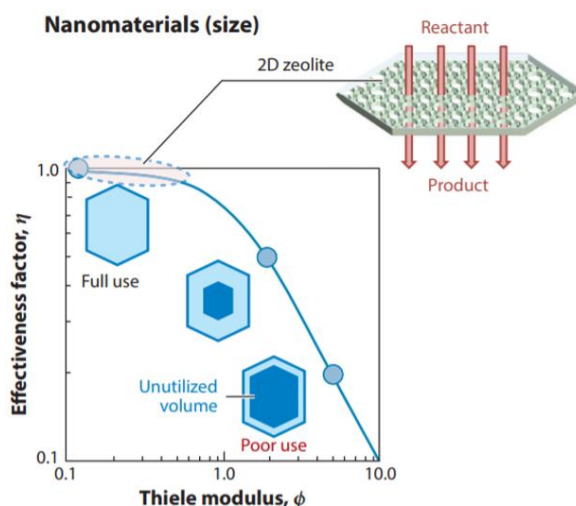


Figure 1.3. Plot of the effectiveness factor η as a function of the Thiele modulus ϕ for porous materials. The effective factor η is the rate of reaction within the catalyst interior divided by the reaction rate at the external surface. The Thiele modulus ϕ is the reaction rate to diffusion rate. The figure is adapted from previous work(148).

Hierarchical zeolites have garnered much attention over the last two decades. These materials are comprised of multimodal pore size distributions wherein the introduction of mesopores (2-50 nm) and/or macropores (>50 nm) relieves the configurational diffusion of micropore to Knudsen or molecular diffusion regimes. Numerous methods have been developed to synthesize hierarchical zeolites and they usually can be categorized into two divisions: “top down” and “bottom up” approaches. Mesoporous zeolites can be generated through post-synthetic approaches (“top down”), such as calcination, steaming, acid/base leaching, or chemical treatments, which collectively lead to dealumination or desilication(20, 162–164). Mesoporous zeolites can be

generated through post-synthetic approach (“top down”) such as calcination, steaming, acid/base leaching, or chemical treatments, thus always leading to dealumination or desilication. Aside from the formation of mesopores, the chemical composition (e.g., Si/Al ratio) is inevitably altered during post-treatment, which can be limiting for many catalytic processing, although dealumination is still widely used in FCC and hydrocracking applications. Also, several research groups have combined dealumination and desilication steps to synthesize multi-pore USY zeolite with remarkable textural properties(165). Notable examples of recent progress in the top-down approach is the discovery of surfactant-templated intracrystalline mesopores by Garcia-Martinez and coworkers, which led to the Molecular Highway technology being commercialized by Rive Technology (later acquired by W.R. Grace Company)(165). In a typical synthesis, commercial USY was mixed with a dilute solution of NH_4OH (or TMAOH) and a surfactant (e.g., CTA) under mild conditions at 150 °C for 10-20 h, leading to uniform mesopores (e.g., 4 nm) without altering the crystal size and morphology. The cationic micelle formed by the surfactant balances the charge of Si-O^- species, which prevents the dissolution of original crystals. The elegant intracrystalline mesostructured zeolite (Meso-HY) was maintained via crystal rearrangement and the calcination process. The Meso-HY catalyst showed better stability and improved product selectivity than HY in model cracking reactions by slowing down the deactivation and over-cracking owing to the desired mesoporosity. The invariant Si/Al, uniformed sufficient mesopore, high recovery yield and excellent hydrothermal stability make this technology easily scalable. A similar surfactant-templated approach was applied to both high Si/Al zeolites (e.g. ZSM-5, MOR) and low Si/Al zeolite (NaY, NaX and NaA) pre-treated with mild acid wash(166, 167).

The “bottom-up” approach is widely utilized for the preparation of hierarchical zeolites. Hard templates (e.g. carbon black, carbon nanotube, nanofiber, ordered mesoporous carbons) have been used in conventional hydrothermal synthesis for a varied range of zeolite framework types such as **MFI**, **MEL**, **BEA**, **AFI** and **CHA**(168–170). One notable example is the synthesis of nanosized **MFI** zeolite with tunable confined growth using 3-dimensional ordered macroporous/mesoporous (3Dom) carbon template, discovered by Tsapatsis and coworkers(171). The similar approach was widely applied to diverse zeolites (e.g. **BEA**, **LTA**, **FAU**, **LTL**) and broader applications including Brønsted, Lewis acid catalysts, and battery cathode(82, 172, 173). Hierarchical zeolites can also be synthesized by a soft-templating method, which involves the use of a cationic surfactant, cationic polymer and aerogel(174–178). One notable example is the rational design of gemini surfactants containing both mesopore-templating and structure-directing functions (e.g., 18-N₃-18), which lead to a series of mesoporous molecular sieves (MMSs) with well-tuned mesoporosity(178). Tsapatsis and coworkers discovered the mesoporous ZSM-5 (**MFI**) with self-pillared “house of cards” structure by the selection of two OSDAs (e.g. phosphonium-based and TBA⁺)(179). The reduced crystal size and mesoporosity of these materials showed excellent performance in the liquid phase reaction (e.g. mesitylene alkylation by benzyl alcohol)(180). Recently, Rimer and coworkers successfully synthesized nanosized self-pillared pentasil zeolite (**MFI** and **MEL** intergrowth) using seed crystals in an organic-free synthesis environment to produce pillared zeolites with reduced diffusion limitations(181).

1.5 Dissertation Outline

Although significant effort has been devoted to the enhancement of zeolite catalytic performance, there remains a gap between their complicated crystallization (nucleation and growth) and the ability to a priori design optimal catalysts. This dissertation aims to bridge the gap between the fundamental understanding of zeolite crystallization mechanisms and developing synthesis methods to improve the performance of zeolite catalysts. Chapter 2 of this dissertation provides evidence that polyamines are effective additives in SSZ-13 synthesis owing to their ability to impact nucleation by regulating the evolution and colloidal stability of amorphous precursors in nonclassical crystallization, which is verified using a combination of electron microscopy and light scattering techniques. Inspired by protrusions or deposits on crystal surfaces as a result of particle attachment that exhibit three-dimensional (3D) growth, we designed an alternative and efficient synthetic approach to enhance mass transport properties by secondary growth using finely tuned compositions that allow for the epitaxial growth of fins on the surface of seed crystals. The improved catalyst lifetime and selectivity have been demonstrated in two model reactions and various zeolite framework types coupled with state-of-art characterization. More significantly, we demonstrate the ability to upgrade commercial catalysts, which has the potential to be implemented as a commercial technology for the next generation of zeolite catalysts. These will be discussed in Chapter 3 and 4 for three- and two-dimensional materials, respectively. Unveiling zeolite catalyst performance under reaction condition is nontrivial given the myriad of tunable properties. In Chapter 5, we provide a discussion of efforts to draw equivalent comparisons among several hierarchical ZSM-5 (**MFI**) materials in MTH reaction. Preliminary results demonstrate that many hierarchical materials are

inherently defective, and that post-synthetic approaches (e.g., annealing) and the judicious selection of reaction condition (e.g., temperature) can remove defects and/or enable direct comparison of catalyst performance.

Chapter 2

Accelerating the Crystallization of Zeolite SSZ-13 with Polyquaternary

Amine Additives

The manuscript discussed in this chapter is submitted. Figure and table numbers have been changed for dissertation consistency. The work was in collaboration with Dr. Eduard L Kunkes, Dr. Vivek Vattipalli and Dr. Ahmad Moini from BASF corporation; Dr. Noemi Linares, and Prof. Javier García-Martinez from University of Alicante.

2.1 Motivation

Nonclassical mechanisms of crystallization can involve a diverse range of species that include (but are not limited to) oligomers, liquid droplets, amorphous colloidal particles, and nanocrystals(91). Nucleation often involves two-step processes(182, 183) where these species form clusters that undergo disorder-to-order transitions. Moreover, crystallization by particle attachment (CPA) comprises similar structural transformations of amorphous precursors as they attach and integrate into crystal surfaces(184). Aluminosilicate zeolites are exemplary materials that crystallize via these complex pathways. Growth media contain a high density of amorphous colloidal particles (or gels) that are rich in silica, and therefore must undergo dissolution-reprecipitation processes to form zeolites where aluminum and silicon are distributed throughout the crystal structure. The specific processes involved in zeolite nucleation are generally not well understood, yet it is recognized that the ability to control amorphous precursor assembly and structural evolution is critical to modulating induction time and crystal properties (e.g., size distribution). In this study, we focus on the synthesis of zeolite SSZ-13 (**CHA** type), which is a commercial material used in catalysis and adsorption applications(63, 185). We have previously studied SZZ-13 growth solutions where ca. 1 μm sized crystals are formed from amorphous precursors

(ca. 100 nm in diameter) via processes that include both monomer addition (classical pathway) and precursor attachment followed by an amorphous-to-crystal transition (nonclassical pathway). We showed that zeolite growth modifiers(95, 96), such as polyethylenimine (PEIM), can operate as colloidal stabilizers, thereby inhibiting precursor aggregation to create a large population of nuclei that leads to a final product of much smaller SSZ-13 crystals (ca. 100 nm). It was also demonstrated that high concentrations of polydiallyldimethylammonium (PDDA) leads to the opposite effect: SSZ-13 crystals with sizes of ca. 10 μm wherein we hypothesized that PDDA promotes the rate of colloidal precursor attachment to crystal interfaces. It has also been demonstrated PDDA at high concentrations can be used as a mesoporegen to produce hierarchical zeolites(186, 187).

2.2 Experimental Methods

2.2.1 Material

The following chemicals were used as reagents: Cab-O-Sil (M-5, Spectrum Chemical), LUDOX AS-40 (40 wt. % in H_2O , Aldrich), sodium hydroxide (98% pellets, MACRON Fine Chemicals), N,N,N-trimethyl-1-1-adamantammonium hydroxide (25 wt. % in H_2O , SACHEM Inc.), polydiallyldimethylammonium chloride (PDDA, MW = 150k, 20 wt. % in H_2O , Sigma-Aldrich), polydiallyldimethylammonium chloride (PDDA, MW = 450k, 20 wt. % in H_2O , Sigma-Aldrich), polyethylenimine (PEIM, MW = 1300, 50 wt. % in H_2O , Sigma-Aldrich), poly(acrylamide-co-diallyldimethylammonium) chloride (PDDAM, 10 wt. % in H_2O , Aldrich), hexadimethrine bromide (PB, $\geq 94\%$ titration, Sigma), 1-butyl-1-methylpyrrolidinium chloride (BMP, $\geq 99.0\%$ titration, Sigma-Aldrich), 1-ethyl-1-

methylpyrrolidinium bromide(EMP, 99%, Aldrich) and aluminum hydroxide (76.5 wt. % Al(OH)₃, reagent grade, Sigma-Aldrich). Sodium metasilicate pentahydrate (\geq 95.0% titration, Aldrich). All reagents were used as received without further purification. Deionized (DI) water used in all experiments was purified with an Aqua Solutions RODI-C-12A purification system (18.2 M Ω).

2.2.2 Synthesis of SSZ-13 Materials

For the synthesis of SSZ-13 crystal, N,N,N-trimethyl-1-1-adamantammonium hydroxide (TMAda) was used as the organic structure directing agent (OSDA). The method was the similar as the reported literature.⁽⁹⁶⁾ In a typical synthesis, 50 wt.% sodium hydroxide solution (0.18g, 0.0023 mol) was first mixed with water (8.13g, 0.4960 mol), followed by the addition of TMAda (0.95g, 0.0011 mol) and stirred for 30 min at room temperature. Aluminum hydroxide (0.06g, 0.0006 mol) was added to the solution and left for another 20 min. Cab-O-Sil (0.68g, 0.0113 mol) used as silica source was added under continuous stirring to produce a final synthesis mixture with a molar composition of 0.052 Al(OH)₃: 1.0 SiO₂: 0.2 NaOH: 44 H₂O: 0.1 TMAda. The growth mixture was aged at room temperature for 4 h with stirring. Crystals synthesized by this procedure are referred to as the *control*. In some syntheses, colloidal silica (LUDOX AS-40) was also used as silica source. For studies of SSZ-13 synthesis in the presence of organic growth modifiers, the additive of choice was added to the growth solution in a specific weight percentage of the entire growth solution after OSDA addition, but prior to the addition of alumina and silica source. The mixture was transferred to a 23 ml Teflon lined stainless steel acid digestion bomb (Parr Instruments). The sealed autoclave was heated in a Thermo Scientific Precision oven under rotation (~ 30 rpm) and autogenous pressure at 170 °C or 180 °C. After a

specified synthesis time, the autoclave was removed from the oven and quenched to room temperature in the water bath. The products of all syntheses were extracted by centrifugation and washed for a total of three cycles (10 min per cycle, 13,000 rpm) using about 50 ml DI water each cycle. The solids were dried in an oven at 50 °C overnight.

2.2.3 Characterization

As-synthesized materials were characterized by powder X-ray diffraction (PXRD) using a Rigaku SmartLab diffractometer with Cu-K α radiation (40 kV, 44 mA) to verify the crystalline structure. Powder XRD patterns acquired from 5° to 50° 2 θ with a step size of 0.02° were compared to simulated patterns of **CHA** framework type provided by the International Zeolite Association Structure Database(6). Scanning electron microscopy (SEM) was performed with a FEI 235 dual-beam (focused ion-beam) system operated at 15 kV and a 5 mm working distance. All SEM samples were coated with a thin carbon layer (ca. 20 nm) prior to imaging to reduce the effects of charging. The molar Si/Al ratio (SAR) of samples was measured by inductively coupled plasma analysis in combination with optical emission spectroscopy (ICP-OES). Before analysis, a Katanax X-300 Fusion Fluxer instrument was used to conduct the fusion of samples (approximately 100 mg) prepared by first dissolving with LiBO₂ (98.5 wt.% lithium metaborate and 1.5 wt.% LiBr). The mixture was heated to 1000 °C for 15 min. Then 2 N HNO₃ was added to the molten mixture and stirred for 10 min, followed by dilution with water to 50 g. The elemental components of the samples were analyzed using an Agilent 725 instrument.

Transmission electron microscopy (TEM) images were taken with a JEOL JEM-1400 Plus instrument. Solids were ground, suspended in ethanol, and sonicated for 15 min. A few drops of this suspension were placed on a Lacey Formvar/Carbon copper grid. Ethanol was evaporated at room temperature. Field emission electron microscopy (FE-SEM) images were performed in a ZEISS model Merlin VP Compact apparatus. Before the analyses, the samples were coated with a 2 nm layer of Iridium using a Quorum Q150T ES Plus sputter coater.

Dynamic Light scattering (DLS) measurements were performed on a Brookhaven Instruments BI-200SM machine equipped with a TurboCorr Digital Correlator, a red HeNe laser diode (35 mW, 637 nm), and a decalin bath that was filtered to remove dust. The liquid sample cell was regulated at 25 °C with a Polyscience digital temperature controller. The model system is SiO₂: NaOH: 1760 H₂O: 0.1 TMAc with increasing additive concentrations in this experiment. LUDOX AS-40 was used as silica source. When we prepared the model solution, we first dissolved sodium hydroxide solution into water in a small vial. Then Ludox AS-40 was added as silica source into the solution. The solution was stirred for about 5 mins at room temperature. Various quantity amounts of PDDA were added and the solution was ready for DLS measurement. DLS experiment was performed at a fixed scattering angle of 90°. At least nine measurements were performed for each point. Autocorrelation functions were collected over a 20 s time frame and data were analyzed by the method of cumulants to obtain the hydrodynamic diameter D_H . Viscosity was calibrated using Ubbelohde viscometers. Oblique illumination microscopy (OIM) measurements were employed by using Nanosight LM10-HS microscope (Nanosight Ltd) equipped with green laser with $\lambda = 532$ nm operating at temperature $T = 25.0 \pm 0.1$ °C to examine the Brownian motion

of individual clusters in the tested solutions. The raw data of this method are movies of point spread functions of clusters undergoing Brownian motion with a powerful objective lens and a faster, sensitive camera (S-PRI, AOS Technologies AG).

2.3 Results and Discussion

2.3.1 SSZ-13 Synthesis with Polyquaternary Amines

In this study, we show that the role of PDDA in zeolite synthesis is more nuanced than previously postulated⁽⁹⁶⁾. Here we performed detailed analyses of SSZ-13 synthesis in the presence of PDDA along with a library of (macro) molecules with predominantly quaternary amine functionality to show how the judicious selection of modifier structure and its concentration can modulate SSZ-13 nucleation.

SSZ-13 crystal growth modifiers were selected from a library of quaternary or polyquaternary (polyquat) amines possessing different molecule sizes and structures (Figure 2.1A). Syntheses of SSZ-13 typically employ N,N,N-trimethyl-1-adamantylammonium (TMA_{da}, I) as an organic structure-directing agent (OSDA). As potential zeolite growth modifiers (ZGMs), we selected four (macro) molecules with similar functionality: poly(acrylamide-co-diallyldimethylammonium) (PDDAM, II), hexadimethrine (polybrene or PB, III), 1-ethyl-1-methylpyrrolidinium (EMP, IV), and polydiallyldimethylammonium (PDDA, V). For control experiments in the absence of any modifier, crystallization is complete within 44 h of heating at 180 °C. One consistent observation among all four ZGMs at low concentrations (≤ 0.2 wt.%) is a two-fold reduction in crystallization time (Figure 2.1B and C) relative to the control. In the case of PDDAM and EMP, these two additives require slightly higher concentrations to exert the same effect as other ZGMs tested. For the small molecule

EMP, there is a two-fold reduction in SSZ-13 crystallization time over the entire range of modifier concentration. Another small molecule 1-butyl-1-methylpyrrolidinium (BMP) was tested for its impact on SSZ-13 crystallization time and exhibits a similar trend as EMP (Figure A1). However, there is a distinct trend observed for the three polymers (PDDAM, PDDA, and PB) wherein higher concentrations (> 0.5 wt.%) lead to increased crystallization times: 48 h for PDDAM, 72 h for PDDA, and 144 h for PB. Interestingly, evaluation of the OSDA (TMAda, I) also revealed a two-fold reduction in crystallization time when increasing the concentration slightly above its nominal value, but returning to a longer crystallization time (equivalent to the control) at higher TMAda concentrations (Figure A2). For comparison, we also assessed the performance of polyethylenimine (PEIM, VI), which lacks the polyquat functionality, but was previously identified as an effective modifier of SSZ-13 crystallization⁽⁹⁶⁾. We find that PEIM has a similar parabolic-like trend as other polymers tested (Figure 1B) with a two-fold reduction in crystallization time at lower concentrations and an increase at higher concentrations (reaching a maximum of 144 h). See XRD analyses for all ZGMs in Figures A3 and A4.

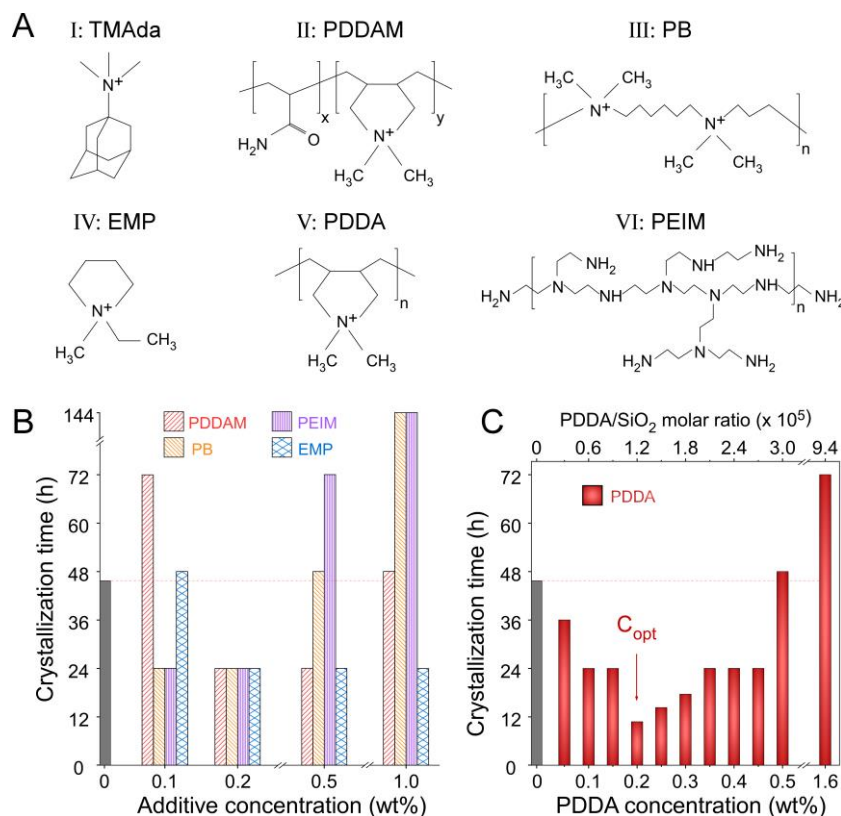


Figure 2.1. (A) Modifiers of SSZ-13 crystallization: (I) TMAda, (II) PDDAM, (III) PB, (IV) EMP, (V) PDDA, and (VI) PEIM. (B and C) Crystallization times estimated from time-resolved powder XRD patterns as a function of modifier concentration for syntheses at 180 °C.

Among the ZGMs tested in bulk assays (Figure 2.1), PDDA was the only modifier to accelerate SSZ-13 crystallization time by a factor of four at intermediate PDDA concentration. As shown in Figure 2.1C, there is a narrow range of concentrations spanning from 0.2 to 0.3 wt.% where the reduction in crystallization time is more pronounced than other ZGMs. The most significant effect is observed at an optimal concentration of 0.2 wt.% (labelled C_{opt}) where the crystallization time is reduced four-fold relative to the control. Collectively, these findings indicate that ZGMs possessing ammonium moieties can significantly alter SSZ-13 nucleation. Herein, we examine mechanistic aspects of growth modification that impact both nucleation and crystal growth. In a previous study⁽⁹⁶⁾ we showed that SSZ-13 synthesis occurs via a

combination of classical and nonclassical pathways involving the addition of monomers and amorphous precursors, respectively. Crystallization by particle attachment is evident when examining the electron micrographs (Figure 2.2A and B) of solids extracted from a control synthesis at an intermediate time (i.e., a partially crystalline product, Figure A5). The spheroidal precursors (arrows in Figure 2.2A and B) are amorphous and predominantly comprised of undissolved colloidal silica from the original synthesis gel (Figure A6), as confirmed by transmission electron microscopy (TEM). The induction period for SSZ-13 nucleation was estimated from time-resolved powder X-ray diffraction (XRD) patterns of extracted solids based on the initial emergence of Bragg peaks, which slightly overestimates the time corresponding to the onset of nucleation. The control sample exhibits an induction period of 30 to 35 h that varies from batch to batch (Figure A7). At the nominal temperature of 180 °C, there is an approximate 10-14 h period of growth prior to achieving a fully crystalline product. Introduction of PDDA at its optimal concentration ($C_{opt} = 0.2$ wt.%) reduces the induction period to ca. 9 h (Figure 2.2C) with an even more dramatic impact on the timeframe of growth (ca. 30 min). The relatively small window of time between the onset of nucleation and a fully crystalline product makes characterization of intermediate stages challenging; therefore, time-resolved studies in the presence of ZGMs was conducted at a lower temperature (170 °C) to extend the period of growth (Figure 2.2D and A8). Indeed, similar studies of PDDA at C_{opt} reveal nucleation around 12 h and growth over a ca. 10 h period (Figure 2.2D). The optimum concentration was also observed when the silica source was replaced from fumed silica to colloidal particles (LUDOX AS-40) with a little shift to 0.3 wt.% (Figure A9). High molecular weight of PDDA (450 kDa) was also tested to see if polymer size affects SSZ-13 crystallization (Figure A10). The high molecular weight or long chain length seemingly

has little effect on the crystallization process, with a crystallization time of 12 h instead of 10 h at 0.2 wt.% concentration with the addition of high molecular weight PDDA. Also, the hydrothermal stability of PDDA was evaluated by ^1H NMR experiments (Figure A11) and the polymer structure showed negligible decomposition after heating at 180 °C for one day.

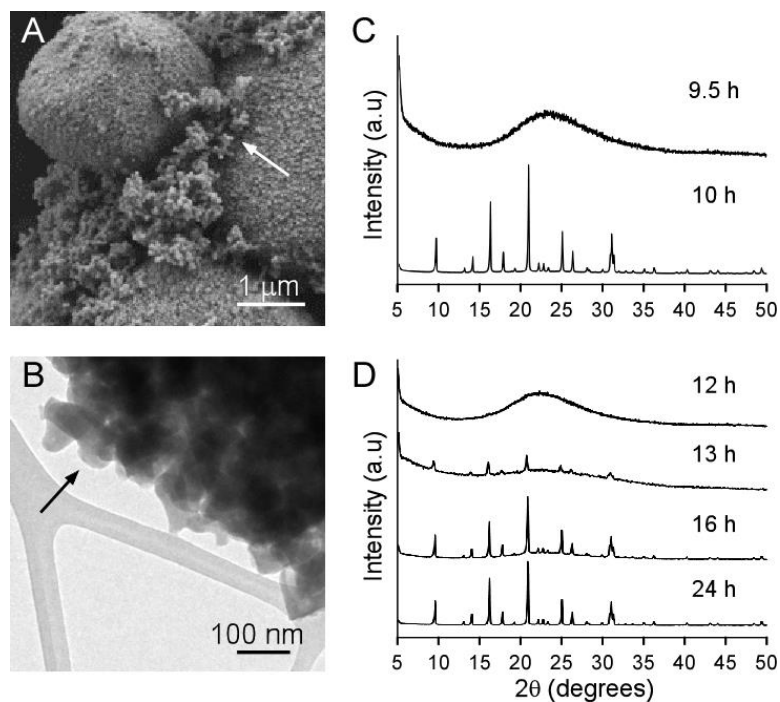


Figure 2.2. (A and B) Samples extracted from a control synthesis after 36 h by (A) FE-SEM and (B) TEM. Arrows denote amorphous precursors. (C) Powder XRD patterns of samples extracted from a growth solution with 0.2 wt.% PDDA heated at 180 °C. (D) Powder XRD patterns of samples extracted from the same growth solution heated at 170 °C.

Experiments at reduced synthesis temperature allowed for the temporal analysis of precursor size (Figure 2.3) during various stages of growth that span the induction period and early stages of crystallization. Prior studies of several zeolites (e.g., **LTL**, **TON**, **MFI** and **MEL**)(95, 188, 189) have revealed that amorphous precursors evolve in size during periods of room temperature aging and hydrothermal treatment. For some zeolites, precursor size decreases with time because of dissolution; and for others

precursor size increases with time via Ostwald ripening and/or aggregation processes. For SSZ-13 syntheses, precursor size is measured as an approximate diameter of the spheroidal morphology. In the absence of modifiers, hydrothermal treatment of growth solutions results in a monotonic increase in precursor size (Figure 2.3A) from an initial diameter of 20 nm to a final value of 52 nm (Figure 2.3B). Once the induction period is finished, the size of the precursors remains fixed during SSZ-13 crystallization. A similar time-resolved analysis was performed with growth media containing EMP, a molecule with close resemblance to the monomer of PDDA (Figure A12). TEM images of solids collected at periodic times during the induction period, which is much shorter than that of the control, reveals negligible change in precursor size. For identical studies with low (0.2 wt.%) and high (0.5 wt.%) concentrations of PDDA, the initial precursor size is ca. 15 nm and there is no appreciable change in precursor size with prolonged hydrothermal treatment (Figure 2.3C). Therefore, it seems there is no direct correlation between SSZ-13 growth kinetics and evolution in precursor size given the spread of crystallization times (24, 44, and 44 h) for 0.2 wt.% PDDA, 0.5 wt.% PDDA, and 0 wt.% PDDA (control) syntheses, respectively. For the control, we observe precursor growth likely involving Ostwald ripening, whereas PDDA leads to a small reduction in precursor size putatively attributed to dissolution. For each of these syntheses, elemental analysis of supernatant solutions (Figure A13) at periodic times during the induction period reveals little change in composition (i.e., Si/Al ratio) irrespective of trends in precursor evolution.

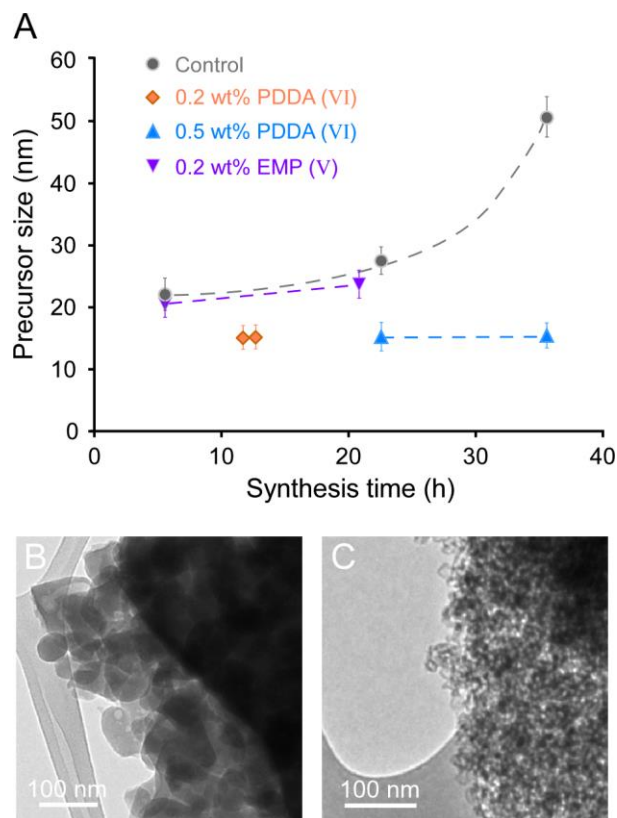


Figure 2.3. (A) Precursor size in solids extracted from growth solutions containing 0.2 wt.% PDDA (orange), 0.5 wt.% PDDA (blue), 0.2 wt.% EMP (purple), and no additive (grey). (B and C) Transmission electron micrographs (TEM) of amorphous precursors extract from a growth solution (B) without modifier and (C) with 0.5 wt.% PDDA after heating at 170 °C for 36 h.

2.3.2 Putative Arrangements of Amorphous Precursor on SSZ-13 Nucleation

To further explore the unique dependence of SSZ-13 crystallization time on PDDA content, we analyzed precursor colloidal stability using dynamic light scattering (DLS). In order to achieve clear solutions for these studies, we prepared solutions with similar compositions used for SSZ-13 synthesis, but without the addition of alumina and with reduced silica content. DLS experiments were performed in the absence (Figure 2.4A, black diamonds) and presence (Figure 2.4A, orange triangles) of OSDA to determine if TMAda interactions with colloidal silica interfere with those of PDDA additive. Measurements of the average hydrodynamic diameter as a function of PDDA

concentration revealed a maximum at a PDDA:SiO₂ ratio in the same order of magnitude as C_{opt} in SSZ-13 bulk crystallization assays (Figure 2.1C), and similar trends for solutions with and without OSDA. These findings indicate that PDDA at concentrations around C_{opt} reduce the colloidal stability of silica particles with an initial size of 25 nm to form clusters with sizes of 400 – 500 nm. This seems to suggest that a similar phenomenon may occur in SSZ-13 growth solutions wherein PDDA promotes the aggregation of precursors at a critical concentration, whereas the degree of aggregation is much less at higher PDDA concentration. For comparison, identical DLS studies were performed in solutions with EMP, PB, PDDAM, and PEIM of varying concentrations; however, in these solutions we did not observe any appreciable change in hydrodynamic diameter (Figure A14), indicating that aggregation only occurred with PDDA and not with other polyquats or EMP, a pseudo monomer of PDDA.

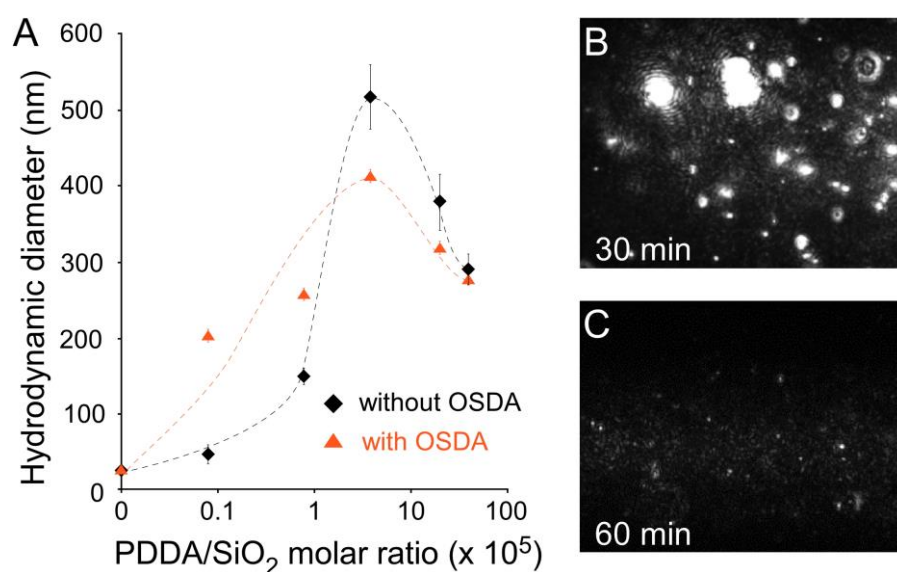


Figure 2.4. (A) DLS measurements of colloidal silica particle hydrodynamic diameter after 5 min. (B and C) OIM studies in clear solutions prepared from soluble silica source (sodium silicate) at a molar composition of 1 Na₂SiO₃: 1760 H₂O: 0.1 TMAda with (B) 0.05 wt.% PDDA (corresponding to C_{opt}) after 30 min, and (C) 0.5 wt.% PDDA after 60 min.

DLS studies examined the effect of polymer additive on precursor colloidal stability; however, we also explored the effect of PDDA on soluble silica species in the solution state using oblique illumination microscopy (OIM). This technique detects the presence of particles (sizes > 10 nm) and allows for time-resolved tracking of diffusion based on Brownian motion (details are provided in the Supporting Information). OIM studies were performed using solutions with an identical molar composition as those employed in DLS studies, but replacing colloidal silica with sodium silicate. The latter, which is comprised of silica monomer and/or small oligomers, is devoid of particulates. This was confirmed by OIM measurements in the absence of PDDA (control), which contained no evidence of particles in solution. Measurements of the same solution containing PDDA at its optimal concentration, C_{opt} , revealed the presence of colloidal particulates within 30 min (Figure 2.4B and Movie A1). This indicates that PDDA has the ability to promote the assembly (or polymerization) of soluble silicates into denser phases of unknown density (i.e., particles or liquid droplets). Analysis of solutions containing PDDA at a higher concentration (Figure 2.4C and Movie A2) showed that there are significantly fewer aggregates after 60 min of imaging, and that the size of these clusters is significantly smaller. Similar measurements were done for solution containing EMP shows little to no aggregation after 1h of imaging (Movie A3).

Here we propose a generalized explanation of zeolite crystal growth modulation in the presence of ZGMs. In the absence of modifiers, precursors grow via ripening or aggregation processes (pathway (i) in Figure 2.5). Low coverage of modifiers (pathway (ii) in Figure 2.5) impedes precursor growth, leading to higher surface area that facilitates exchange of species at the precursor – solution interface with concomitant reduction in crystallization times. At high modifier coverage (pathway (iv) in Figure

2.5), ripening is suppressed, particle size remains small, and colloidal stability is maintained by steric stabilization, which is a general characteristic of polymers(190) but was also observed for small molecules (e.g., EMP). A high density of adsorbed modifier likely impedes the direct interaction and/or exchange of (alumino)silicate species between solid and solution phases, which can cause significant delays in SSZ-13 crystallization time. This is true for all modifiers tested with the exception of monomer, which does not appear to alter solid-solution exchange in ways that increase SSZ-13 crystallization time. The optimal scenario at intermediate concentrations of PDDA (pathway (iii) in Figure 2.5) leads to precursor clustering, akin to bridging flocculation(190), which is characteristic of polymer-colloid interactions at low-to-moderate polymer concentration. This phenomenon has been reported for PDDA interactions with colloidal silica(191, 192). Precursor particles within these clusters can maintain high surface area contact with solution where their close proximity creates confined regions (callout in Figure 2.5, iii) of entrained supernatant solution. We posit these confined regions accelerate SSZ-13 nucleation through pathways that likely include more facile mass transfer and exchange of (alumino)silicate species between solid and solution phases, which has the potential to create a localized high concentration of soluble species where precipitation can be accelerated by the presence of PDDA, consistent with observations in Figure 2.4B.

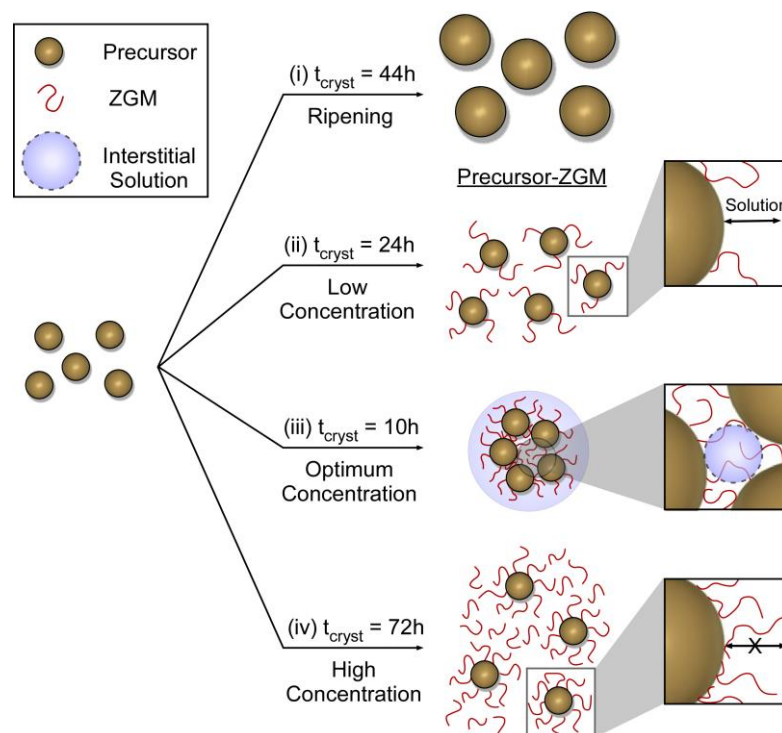


Figure 2.5. Putative arrangements of amorphous precursor suspensions (left) prior to the onset of SSZ-13 nucleation at the following conditions: (i) absence of modifier (control); (ii) low modifier coverage; (iii) intermediate coverage corresponding to an optimal ZGM concentration, C_{opt} , only observed for PDDA (see Figure 2.1C); and (iv) high modifier coverage.

In our previous study(96), the impact of PDDA on SSZ-13 size was rationalized on the basis of nonclassical CPA growth mechanisms wherein we posited that PDDA promotes precursor attachment to growing zeolite crystals. In view of the current findings, an alternative hypothesis can be proposed wherein PDDA alters processes of nucleation wherein SSZ-13 crystals produced in the range of critical PDDA concentration have similar sizes as the control, suggesting a reduction in the induction period without appreciable changes to the number density of nuclei; however, at high PDDA concentrations when crystallization time is markedly longer than the control, the number density of nuclei is much smaller, which ultimately leads to a population of larger crystals; therefore, it is evident that ZGMs impact SSZ-13 nucleation, but less certain how modifiers influence the rate of growth (i.e. precursor attachment) as

previously hypothesized. In models of classical nucleation, the rate of nucleation (and concomitantly the final crystal size) is governed by synthesis parameters such as supersaturation or temperature. In the case of SSZ-13, it is apparent that nucleation rates are regulated on the basis of precursor assembly, evolution, and/or aggregation where the exact origin is more complex and not well understood. One of the challenges associated with performing detailed kinetic studies of SSZ-13 crystallization is the absence of LaMer nucleation^(193–195) involving a burst (or instantaneous formation) of nuclei that grow as a population over time. The first crystals detected in growth solutions have a size similar to those depicted in Figure 2.2A (i.e., equivalent to size of fully-grown SSZ-13 particles), which has thwarted attempts to extract time-resolved changes in zeolite crystal size. As such, the direct impact of ZGMs on SSZ-13 crystal nucleation and growth both remain elusive.

2.4 Summary

In summary, we provided evidence that polyamines are useful additives in SSZ-13 synthesis in that they markedly impact nucleation by regulating the evolution and colloidal stability of amorphous precursors. Interactions between polymers and precursor particles have the potential to alter the exchange of (alumino)silicate species between solid and liquid phases. Our findings revealed that PDDA induces bridging flocculation of precursors within a narrow range of polymer concentration, which greatly accelerates nucleation. Within the same range of critical concentration, we also showed that PDDA promotes the precipitation of soluble silicates. On the basis of these two observations, we hypothesize that confined growth solution within interstitial regions of precursor aggregates at critical PDDA concentration facilitates nucleation, possibly via polymer-mediated reprecipitation of silicates released during precursor

dissolution. The exact mechanism of SSZ-13 nucleation and its modulation (enhancement or inhibition) by polymers remains elusive; however, this work sheds new light on the role of polymer modifiers in SSZ-13 crystallization. In addition to the observed change in crystallization time, our findings also suggest that polymer modification of SSZ-13 crystal size is governed by changes in the rate of nucleation rather than putative alteration of precursor attachment during nonclassical growth. Although further studies are required to elucidate the role of polymer additives in zeolite synthesis, it is evident that by judiciously selecting the polyamine structure and concentration, it is possible to significantly reduce synthesis time and tailor zeolite properties, which are two critical aspects in the industrial production of zeolites.

Chapter 3

Finned Zeolite Catalysts with Three-dimensional Pores

The material discussed in this Chapter has been published. Figure and table numbers have been changed for dissertation consistency. The work was in collaboration with Dr. Taimin Yang and Prof. Xiaodong Zou from Stockholm University; Prof. Paul J. Dauenhauer from University of Minnesota; Dr. Donglong Fu and Prof. Bert M. Weckhuysen from Utrecht University; Prof. Jeremy C. Palmer from University of Houston; Prof. Michael Tsapatsis from Johns Hopkins University.

3.1 Motivation

The confined channels and cages of microporous materials (zeolites) are utilized in numerous applications, which span from catalysis(196, 197) and adsorption(20) to selective separations(21, 22). A common objective in the design of zeolitic materials is to overcome the inherent mass-transport limitations of micropores. This is a ubiquitous challenge for the development of zeolite catalysts in which narrow pore apertures and long diffusion path lengths lead to more rapid deactivation owing to the accumulation of carbonaceous deposits (coke)(198). This is particularly true for zeolites with low-dimensional pore networks. There is an increasing body of literature that shows how the preparation of nanosized crystals can enhance catalyst lifetime and/or alter product selectivity(199, 200). For example, the advent of two-dimensional (2D)(154, 178) or self-pillared(179) zeolites with sizes on the order of a crystal unit cell (~2–4 nm) exhibit a superior catalytic performance to that of conventional zeolites; however, the preparation of these materials has only been demonstrated for a few framework types. Indeed, only a relatively small number of reported zeolites have crystal sizes less than 100 nm(201–203), which highlights the challenges associated with synthesizing nanosized microporous materials. This has motivated the development of alternative methods, such as the preparation of hierarchical zeolites(162, 164), in which the

introduction of mesopores has an analogous beneficial effect on mass transport(203). The practical challenges of nanosized zeolite synthesis include the customary requirement of unconventional organics and the frequent drawback of small product yields. This underscores the need for more facile, efficient methods to produce nanosized zeolites by methodologies that are generalizable to a broad number of framework types.

3.2 Experimental Methods

3.2.1 Material

Zeolite synthesis was performed with the following reagents: tetraethylorthosilicate (TEOS, 98%, Sigma-Aldrich), LUDOX AS-30 (30% suspension in H₂O, Sigma-Aldrich), sodium hydroxide (NaOH, > 98%, Sigma-Aldrich), potassium hydroxide (KOH, 1M, Fisher Chemical), 1,8-diaminooctane (DAO, 98%, Sigma-Aldrich), aluminum sulfate hydrate (Al₂(SO₄)₃, 98%, Sigma-Aldrich), sodium aluminate (technical grade, Alfa Aesar), tetrabutylammonium hydroxide (TBAOH, 40%, Sigma-Aldrich), and tetrapropylammonium hydroxide (TPAOH, 40%, Alfa Aesar). Commercial zeolite ZSM-5 (product number, CBV5524G) was purchased from Zeolyst International. Time-resolved acid titration experiments were performed using 2,4,6-trimethylpyridine (Sigma-Aldrich, >99%). All reagents were used as received without further purification. Deionized (DI) water, used in all experiments, was purified with an Aqua Solutions Type I RODI filtration system (18.2 MΩ). For reaction testing, methanol was purchased from J. T. Baker (99.8%), and the argon, oxygen, and nitrogen gases were purchased from Praxair (UHP grade, 99.999%).

3.2.2 Synthesis of Finned ZSM-11 and ZSM-5 materials

Direct synthesis of conventional and finned ZSM-11 crystals. For the direct synthesis of conventional zeolite ZSM-11, TBAOH was used as the organic structure-directing agent (OSDA). In a typical synthesis, 0.220 g of sodium aluminate was added to a mixture of 0.786 g of NaOH solution (43 mg/g of solution) and 5.36 g of DI H₂O. To this solution was added 5.925 g of TBAOH, followed by the silica source, TEOS (9.707 g). The resulting mixture was stirred at room temperature in a sealed bottle for 2 h to allow for the hydrolysis of TEOS. The resulting solution was placed in a 60 ml Teflon-lined acid digestion bomb (Parr Instruments) that was sealed and heated in a Thermo Fisher Precision oven at 170 °C and autogenous pressures. The autoclave was removed from the oven after 3 days and was quenched in water to room temperature. The molar compositions of synthesis mixtures (Table B1) were varied to synthesize conventional and finned ZSM-11 samples. The crystalline product was removed from the mother liquor by three cycles of centrifugation and washes with DI water, using a Beckman Coulter Avanti J-E centrifuge at 5 °C and 13,000 rpm for 10 min per cycle. Samples for catalysis were calcined in a Thermo Fisher Lindberg Blue furnace under constant flow of dried air (Matheson Tri-Gas) at 550 °C for 5 h with a temperature ramping/cooling rate of 1 °C min⁻¹. These samples were converted to an acid form (Brønsted acids) by ion exchange wherein calcined zeolite was mixed with 1.0 M ammonium nitrate solution to obtain a 2 wt. % suspension. This mixture was heated to 80 °C under continuous stirring for 2 h to allow the exchange of Na⁺ with NH₄⁺. This process was performed three times washing between each ion exchange cycle. The final NH₄-zeolite samples were washed thrice with DI water before they were calcined once again with the same procedure stated above to generate H-form zeolites.

Seed-directed synthesis of finned ZSM-11 and ZSM-5 crystals. The ZSM-11 sample used as seeds was prepared with a molar composition of 10 DAO (1,8-diaminooctane):10 K₂O: 100 SiO₂: 1 Al₂O₃: 4000 H₂O. In a typical synthesis, 0.185 g of Al₂(SO₄)₃ was added to a mixture of 0.61 g of KOH solution (50 wt. %) and 15.35 g of deionized water. To this solution was added 0.40 g of DAO, followed by 5.45 g of colloidal silica (LUDOX AS-30) and 0.22 g of calcined ZSM-11 crystals (2 wt. %) according to the procedures outlined in a previous paper(204). The resulting mixture was stirred at room temperature for 24 h. The sol gel was then placed in a 60 ml Teflon-lined acid digestion bomb and heated in an oven at 160 °C and autogenous pressure for 3 days. The crystalline product was removed from the mother liquor by three cycles of centrifugation and washes with deionized water, using a Beckman Coulter Avanti J-E centrifuge at 5 °C and 13,000 rpm for 10 min per cycle. The resulting seeds were immediately stored in deionized water without allowing time for the solids to dry. A seeded growth solution was made with a molar composition of 27.3 DAO: 11.9 K₂O: 90 SiO₂: 1 Al₂O₃: 3588 H₂O. The solution was prepared by adding an appropriate amount of Al₂(SO₄)₃ to a solution that contained KOH and deionized water, followed by the addition of DAO and LUDOX AS-30. The mixture was stirred at room temperature for 24 h prior to adding 0.65 g of as-synthesized ZSM-11 seeds (10 wt. % relative to the total amount of growth solution). The seeds were not calcined and contained occluded DAO. The suspension was heated for 2 days at 120 °C. The solids were extracted from the mother liquor using the centrifuge/washing procedure described above.

The ZSM-5 sample used as seeds was prepared with a molar composition of 15 TPAOH: 4 Na₂O: 100 SiO₂: 1.67 Al₂O₃: 2500 H₂O: 400 EtOH. In a typical synthesis,

0.094 g of sodium aluminate was added to a mixture of 1.022 g of NaOH solution (46 mg/g of solution) and 12.17 g of DI H₂O. To this solution was added 6.41 g TEOS, followed by the OSDA, TPAOH (2.30 g). The resulting mixture was stirred at room temperature for 2 h prior to heating the sol gel in an oven at T = 170 °C and autogenous pressure for 2 days. The isolated seeds were immediately placed in DI water for storage. A solution for seeded growth was prepared using a molar composition of 10 TPAOH: 0.5 Na₂O: 31.5 SiO₂: 0.5 Al₂O₃: 1660 H₂O. The solution was prepared using similar steps reported in Methods, but with the addition of 0.65g as-synthesized ZSM-5 seeds (5 wt. % relative to the total amount of growth solution) after aging the secondary growth solution. The seeds were not calcined and contained occluded TPA (the only exception is commercial ZSM-5, which is provided by Zeolyst International as a calcined sample without OSDA). The mixture was heated for 24 h at 100 °C with rotation and the solids were extracted as a white powder. For processes employing a thermal annealing step, the gel after centrifugation was directly transferred to a solution with composition 10 TEOS: 14 TPAOH: 9500 H₂O, which was heated at 170 °C for 7 days. The solution was then removed from the oven and the solid was dried in air after multiple centrifugation and washing cycles. The finned Zeolyst sample was prepared by the same seeding and annealing procedures.

The SPP zeolite sample (Si/Al = 75) for acid titration measurements was synthesized following the reported procedure in Zhang et al(179).

3.2.3 Characterization

The H-forms of the zeolite materials were characterized by powder XRD using a Rigaku SmartLab Diffractometer with Cu K α radiation to verify the crystalline

structure. Powder XRD patterns were compared to simulated patterns of each framework type provided by the International Zeolite Association Structure Database(6). Textural analysis of the H-form samples prepared for catalytic testing was performed by N₂ adsorption/desorption using a Micromeritics ASAP 2020. The data were analysed by instrument software to obtain the Brunauer–Emmett–Teller surface area and the microporous volume was determined from the t-plot method. Scanning electron microscopy (SEM) was performed with a FEI 235 dual-beam (focused ion-beam) system operated at 15 kV and a 5 mm working distance. All SEM samples were coated with a thin platinum layer (ca. 5 nm) prior to imaging to reduce the effects of charging. The molar Si/Al ratio of zeolite samples was measured by inductively coupled plasma analysis in combination with optical emission spectroscopy (ICP-OES). Before analysis, a Katanax X-300 Fusion Fluxer instrument was used to conduct the fusion of zeolite samples (approximately 50 mg) prepared by first dissolving with LiBO₂ (98.5 wt. % lithium metaborate and 1.5 wt. % LiBr). The mixture was heated to 1,000 °C for 15 min. Then 50 ml 2 N HNO₃ was added to the molten mixture and stirred for 10 min. The elemental components of the samples were analyzed using an Agilent 725 instrument. NH₃-TPD was performed on a Micromeritics Autochem II 2920 equipped with a TCD detector. Prior to TPD, 60-100 mg of catalyst was first outgassed in helium for 1 h at 600 °C with a heating ramp of 10 °C min⁻¹. NH₃ was adsorbed at 100 °C until saturated, followed by flushing with helium for 120 min at 100 °C. The ammonia desorption was monitored using the TCD detector until 600 °C with a ramp of 10 °C min⁻¹, using a flow of 25 ml min⁻¹. Solid-state ²⁷Al MAS NMR experiments were conducted at 11.7 T on a JEOL ECA-500 spectrometer, equipped with a 3.2 mm magic angle spinning probe. Spectra of all catalysts were obtained at a spinning frequency of 12.5 kHz with a $\pi/12$ pulse width of 1.25 μ s, a recycle delay of 0.8 s and 4096 number

of scans. The ^{27}Al chemical shift was referenced using 1 M $\text{Al}(\text{NO}_3)_3$ aqueous solution. Surface elemental analysis of zeolites was performed with X-ray photoelectron spectroscopy (XPS) using a PHI 5800 ESCA (Physical Electronics) system, which is equipped with a standard achromatic $\text{Al K}\alpha$ X-ray source (1486.6 eV) operating at 300 W (15 kV and 20 mA) and a concentric hemispherical analyzer. Since zeolites are insulating materials, the equipment neutralizer component was utilized to prevent charging effects. All data was collected at a 45° takeoff angle, and collected spectra were analyzed using the MultiPak program.

TEM images and SAED patterns were taken with a JEOL JEM-2100 FEG TEM operated at an accelerating voltage of 200 kV. A Gatan Ultrascan CCD (charge-coupled device) camera was used to collect image data and a Gatan Orius 200D CCD detector was used to collect diffraction data. Sample particles were dispersed and ultrasonicated in ethanol and then dipped on a lacey carbon copper grid. Electron tomography was also performed using the JEOL JEM-2100 FEG. A Gatan 912 ultrahigh tilt tomography sample holder was used to achieve a large tilt range. A tilt series of bright-field TEM images of a zeolite crystal particle was acquired over an angular range from -65 to $+65^\circ$. The interval between neighbouring images was kept at 1.0° . Before the sample was placed on the copper grid, a droplet of a 5 nm gold nanoparticle dispersion was also delivered onto the copper grid as a fiducial marker for tomogram alignment. The software ETomo was used for tilt series data processing, which included alignment and reconstruction.

The reaction intermediates and coke species formed during the MTH reactions were monitored by operando UV–vis diffuse reflectance spectroscopy using an AvaSpec 2048L spectrometer(205, 206). The UV–vis spectra were collected in the wavelength

range 200–1000 nm (11,000–50,000 cm^{-1} in wavenumber) in reflection mode using a high-temperature UV–vis optical fibre probe (Avantes). The probe was placed in a stainless-steel protection sleeve and comprised one excitation and one collection optical fibre with a diameter of 400 μm and a length of 1.5 m. Typically, catalysts with the same pellet size to the performance testing were loaded in a fixed-bed quartz reactor (inner diameter, 6 mm \times 3 mm) and activated at 550 $^{\circ}\text{C}$ for 3 h under 100% oxygen and then cooled to 350 $^{\circ}\text{C}$ (for the reaction) under a flow of helium. A WHSV of 20 h^{-1} was obtained for methanol by flowing helium gas through a methanol saturator at ~ 25 $^{\circ}\text{C}$. UV–vis spectra were collected and saved every 30 s with 100 accumulations.

Time-resolved spectra were measured using a Bruker Vertex 70 FTIR with a HeNe laser and RT-DLaTGS detector (20 kHz scanner velocity, 6 mm aperture and KBr beam splitter). For the sample preparation, ~ 15 mg of a powder catalyst sample was homogenized using an agate mortar and pestle, pressed at 2–3 ton (CrushIR Digital Hydraulic Press; Pike Technologies) for 5 min into 13 mm-diameter pellets (KBR Die, CAS no. 7758-02-3; International Crystal Laboratories) and inserted into the cell body (high temperature cell, Part no. HTC-M-05, CaF_2 windows; Harrick Scientific). Before inserting the sample pellet, a background spectrum was collected (64 scans at 4 cm^{-1} resolution) with the empty cell. A K-type thermocouple (Part no. 008-144; Harrick Scientific) was in constant intimate contact with the sample pellet holder. The manufacturer-provided cartridge heater (100 W, 24 V) was controlled via a temperature controller in cascade mode (Omega CN7800). To ensure that the CaF_2 windows of the sample cell do not overheat, cooling water was continuously pumped (variable flow chemical pump; Control Company) and flowed through water-cooling ports connected to the cell body. The sample was calcined at 500 $^{\circ}\text{C}$ for 4 h in air (Air Ultra Zero; Linde)

at a ramp rate of 5 °C min⁻¹. After calcination, the sample was cooled down to and remained at 150 °C for the duration of the experiment to ensure the absence of water. For the amine purification, H-ZSM-5 (CBV28014; Zeolyst International) was calcined under flowing air at 550 °C for 10 h at a ramp rate of 1 °C min⁻¹. Freshly calcined H-ZSM-5 was added to 20 ml of TMPyr and stirred vigorously (1,200 rpm) for > 1 h. H-ZSM-5 was isolated from TMPyr via centrifugation at 10,000 rpm for > 5min. TMPyr was used immediately post-purification for dosing in FTIR. For the amine dosing process, He gas was flowed over the sample pellet to purge any remaining air. To ensure that the He was moisture-free, He gas was flowed through a liquid nitrogen trap and desiccator before reaching the cell body. The initial spectrum of the calcined catalyst was measured at this time, with the background spectrum subtracted. Purified TMPyr was flowed at 0.06 ml h⁻¹ to the sample cell. FTIR spectra (64 scans, 4 cm⁻¹ resolution and scan range from 4,000 to 1,000 cm⁻¹) were saved continuously at different time intervals during the duration of the experiment: every 30 s for the first 10 min, then every 30 min for the rest of the experiment.

We hypothesized that the bulk zeolite crystal can be modeled as a sphere. We can start with a species balance for molecule A, where A = 2,4,6-trimethylpyridine (TMPyr), and incorporate Fick's Law to model diffusion flux (negligible in all directions except the radial direction, r) to obtain the governing equation as

$$\frac{\partial C_A}{\partial t} = \mathfrak{D} \left[\frac{1}{r^2} \frac{\partial}{\partial r} \left(r^2 \frac{\partial C_A}{\partial r} \right) \right]. \quad (3.1)$$

Then, imposing the initial condition that the starting concentration of TMPyr, $C_{A,0}$, in the cell is based on the preset co-feed rate of 0.06 ml h⁻¹, we have

$$C_A(r, t = 0) = C_{A,0}. \quad (3.2)$$

For the second-order differential, we need two boundary conditions (BCs). The first homogenous Neumann BC naturally arises due to the symmetry condition imposed by the spherical model as

$$\left. \frac{\partial C_A}{\partial t} \right|_{r=0,t}^{\infty} = 0. \quad (3.3)$$

The second Dirchlet BC is assumed after some pseudo-steady state is reached where the concentration of the 2,4,6-trimethylpyridine has reached an equilibrium shown as

$$C_A(r = R, t > t_{ss}) = C_{A,R}. \quad (3.4)$$

Using separation of variables (space- and time-domain) method, we eventually end with the spherical Bessel's solution, shown in Eq. 3.5 after some reordering, where θ_A is the surface coverage of 2,4,6-trimethylpyridine, i.e., percentage of Brønsted acid sites (BAS) titrated by TMPyr.

$$\theta_A(r, t) = \frac{C_A}{C_{A,0}} = \left[\frac{\sin(\lambda_n r)}{r \sin(\lambda_n)} \right] \left[e^{-\lambda_n^2 * \mathcal{D} * t} \right] \quad n = 1, 2, \dots \quad (3.5)$$

Assuming that the TMPyr equally accesses all facets of the approximated “spherical zeolite”, we can focus on the temporal diffusion of TMPyr. Based on the analysis of Eq. 3.5, the diffusion can be modeled as an exponential which is rearranged for the percentage of acid sites titrated where τ is the relevant time scale for diffusion as

$$\% \text{ BAS titrated} = A * (1 - e^{-\lambda_n^2 * \mathcal{D} * t}). \quad (3.6)$$

Thus, we have fit an exponential diffusion model to empirical values obtained from FTIR, where the percentage of Brønsted acid sites titrated by TMPyr in conventional samples is shown in the following equation

$$\% \text{ BAS titrated} = A * \left(1 - e^{-\frac{t}{\tau_{seed}}}\right). \quad (3.7)$$

The model for finned samples is simply a summation of two exponential diffusion models, one with a slow time scale τ_{seed} of TMPyr through the bulk crystal and a faster time scale τ_{fin} through the fins

$$\% \text{ BAS titrated} = A * \left(1 - e^{-\frac{t}{\tau_{seed}}}\right) + A_{fin} * \left(1 - e^{-\frac{t}{\tau_{fin}}}\right). \quad (3.8)$$

3.2.4 Catalytic Measurements

The MTH reaction was carried out according to a previously reported procedure(204) using a fixed-bed stainless-steel reactor (inner diameter, 1/4 inch (6.35mm)), H-form zeolite catalysts and a reaction temperature of 350 °C (Thermo Scientific Lindberg Blue M furnace). The catalysts were pressed and sieved (40–60 mesh) and then homogeneously mixed with a diluent (silica gel, 35–60 mesh; Sigma-Aldrich). Two plugs of quartz wool were used to support the catalyst bed and the reaction temperature was monitored by a K-type thermocouple (Omega Engineering) inserted into the stainless-steel tube. Prior to the reaction, the catalyst bed was activated in situ at 550 °C for 3 h under a flow of dried air and then cooled to 350 °C. Methanol (99.9% purity) was continuously fed into the reactor at a WHSV of 9 h⁻¹ by a syringe pump (Harvard Apparatus) at 7 $\mu\text{l min}^{-1}$ with a preheated inert gas stream of argon (30 cm³ min⁻¹). The effluent was analysed by an online gas chromatograph (Agilent GC7890A) equipped with a flame ionization detector. To compare the deactivation rate of the catalysts, reactions were carried out at a subcomplete methanol conversion, X, with the initial conversion regulated by adjusting the catalyst mass. Methanol conversion is defined as

$$X = [1 - C_{eff}/C_{feed}] \times 100\%. \quad (3.9)$$

where C_{eff} is the carbon-based molar concentration of both methanol and dimethyl ether measured in the effluent and C_{feed} is the concentration of methanol measured in the feed.

The selectivity, S_i , of hydrocarbon product i is defined as

$$S_i = [C_i/C_{t,eff}] \times 100\%. \quad (3.10)$$

where C_i is the carbon-based molar concentration of hydrocarbon i measured in the effluent and $C_{t,eff}$ is the total carbon-based molar concentration of hydrocarbons measured in the effluent.

3.2.5 Kinetic Monte Carlo Simulation

Kinetic Monte Carlo (KMC) simulations were performed to study the transport of benzene through seed and finned silicalite-1 crystals at 300 K. Benzene transport in silicalite-1 was characterized by infrequent jumps between three types of favourable adsorption sites located in S, Z and I of the pores. This hopping process was modelled using first-order kinetic equations solved stochastically using the rejection-free KMC algorithm described by Laloué et al.(207). The rate constants for the elementary transitions between adsorption sites were derived in a previous atomistic simulation study using rare-event sampling methods, in which they were shown to lead to good predictions of benzene's experimentally measured diffusivity(208, 209).

The seed and finned zeolite crystals were created by replication of the orthorhombic (Pnma) unit cell of **MFI**, which has unit-cell dimensions of $a = 2.01$ nm, $b = 1.99$ nm and $c = 1.34$ nm along its three principal crystallographic axes. The seed crystal was generated by replicating the unit cell to create a nearly cubic $247 \times 250 \times 372$ (496.47

$\times 497.50 \times 498.48 \text{ nm}^3$) supercell with linear dimensions of about $\beta = 500 \text{ nm}$ in each direction. The finned crystal was generated by decorating the surface of the smooth structure with smaller, nearly cubic $24 \times 25 \times 37$ ($48.24 \times 49.750 \times 49.58 \text{ nm}^3$) supercells with linear dimensions of $\alpha = 50 \text{ nm}$ in each direction; the fin location on the surface was chosen to ensure continuity of the pore network. As prescribed by the KMC model, the pore networks of both crystals were represented as lattices with S, Z, and I adsorption sites. On the order of 10^8 and 10^9 lattice sites were needed to represent the seed and finned structures, respectively, examined in this study.

Mass transport through the seed and finned zeolite crystals was characterized by computing the diffusion path length for benzene as

$$r = \sum_{i=1}^{n-1} |\Delta r_i|. \quad (3.11)$$

where $|\Delta r_i| = |r_i - r_{i-1}|$ is the scalar distance travelled in the i^{th} kMC step and r is the position vector of the molecule. The initial position r_0 at time $t_0 = 0$ was chosen by placing benzene at a randomly selected lattice site on the outside of crystal's bounding surface. The kMC moves were attempted and rejected until the molecule first crossed the bounding surface of the crystal, entering at position r_1 and time t_1 . The trajectory of the molecule was then propagated for n kMC steps, with the n^{th} step corresponding to the event in which the molecule first exited the zeolite crystal by re-crossing the bounding surface. The residence time within the crystal was calculated as $\tau = t_{n-1} - t_1$. For each structure, the mean diffusion path length $\langle r \rangle$ and residence time $\langle \tau \rangle$ were estimated by averaging over 10^5 independent trajectories. In each case, only a single benzene molecule was simulated inside the crystal such that interactions between diffusing species could be neglected.

Simulations were performed for several models with different surface-to-surface fin spacing γ ranging from 4 to 50 nm to vary the surface density of fins from 3.3×10^{-4} to $1.0 \times 10^{-4} \text{ nm}^{-2}$. The mean diffusion path length $\langle r \rangle$ and residence time $\langle \tau \rangle$ decrease monotonically as the surface density of fins increases. For the models examined, these metrics are reduced by a factor ranging from 1.5 to 2.5, thereby demonstrating that the mass transport characteristics of the finned crystals are enhanced relative to the seed zeolites for a broad range of fin densities.

3.2.6 Steered Molecular Dynamics Simulations

Molecular simulation was used to investigate the mobility of 2,4,6-trimethylpyridine (TMPyr) in all-silica **MEL** (silicalite-2) and **MFI** (silicalite-1) zeolite frameworks. Although experiments show that TMPyr can adsorb and diffuse within silicalite-2 and silicalite-1, these processes occur over long-time scales due to the similarity in size of the molecule and the characteristic dimensions of pores in these frameworks. As a result, TMPyr was not observed to transition between zeolite cages in **MEL** and **MFI** on time scales accessible with standard molecular dynamics (MD) simulations (in qualitative agreement with the long times required for experimental titrations). Thus, we employed a steered molecular dynamics (SMD) protocol in which a time-dependent bias was applied to promote cage hopping in silicalite-2 and silicalite-1. The SMD simulations were conducted with GROMACS 5.1.5(210). The zeolite frameworks were described using the clay force field (ClayFF)(211), whereas TMPyr was modelled using OPLS force field parameters generated by the LigParGen web server(212). Lennard-Jones (LJ) parameters for interactions between the zeolite framework and TMPyr were determined using Lorentz-Berthelot (LB) combining rules. The LJ size and well depth parameters (σ and ϵ) for interactions between C, H, and N atoms on TMPyr and O atoms

in the zeolite were scaled by factors of 0.9126 and 1.4202, respectively. In previous computational studies(208, 213), application of these scaling factors to the parameters obtained using the LB combining rules was shown to improve the predicted transport properties of aromatic compounds in zeolites. Lennard-Jones and real-space electrostatic interactions were truncated at 1.2 nm. The particle mesh Ewald (PME) method was used to treat long-range electrostatics, with parameters chosen to ensure a relative error of less than 10^{-5} in the computed energy.

The **MEL** framework was modelled as a $2 \times 2 \times 3$ supercell ($4.05 \times 4.05 \times 4.03$ nm³), generated using crystallographic data from the International Zeolite Association database(6). A single TMPyr molecule was inserted at an intersection of the major straight channels of the framework. The system was energy minimized using the steepest descent algorithm to remove pair-wise forces larger than 10 kJ mol⁻¹ nm⁻¹ and then subsequently equilibrated by performing an 8 ns MD simulation in the NVT ensemble. The equations of motion were integrated using the leap-frog algorithm with a 2 fs time step, and a Bussi-Parrinello velocity-rescaling thermostat(214) with 2 ps time constant was applied to maintain the temperature at 300 K. Following equilibration, a 22 ns SMD simulation was performed in the NVT ensemble using PLUMED 2.4.3.(215) plugin for GROMACS. In the SMD simulation, a moving harmonic restraint with spring constant of $50,000$ kJ mol⁻¹ nm⁻² was applied to the center of mass of the TMPyr molecule to pull it 2 nm along the major axis of the straight channel of silicalite-2 at an average velocity of 0.1 nm ns⁻¹. The SMD simulation for silicalite-1 was performed using the same protocol in a system where TMPyr was inserted at an intersection of the straight and sinusoidal channels in a $3 \times 3 \times 3$ supercell ($5.89 \times 5.86 \times 3.93$ nm³).

Trajectories from the SMD simulations reveal that TMPyr's cage hopping mechanism in **MEL** proceeds via several intermediate steps. The intermediate steps involve concerted translations and rotations that result in one of the molecule's methyl groups protruding into apertures formed by small ring structures in the framework, thereby allowing the bulky aromatic ring of TMPyr to transverse narrow regions of the pore. Cage hopping in **MFI** is observed to proceed via a similar process.

3.3 Results and Discussion

3.3.1 One-pot Synthesis of Finned Zeolites

Here we investigate an alternative method of reducing (to reduce) internal diffusion limitations via the synthesis of zeolites with rough protrusions (size α) on their exterior surfaces (Figure 3.1a), which exhibit an identical crystallographic registry with the interior crystal (size β). These features resemble “fins”, which are well known to enhance the rate of heat transfer in conductive materials owing to the increased external surface area. Analogous to studies by Ryoo and coworkers(178) who showed that hierarchical zeolites possessing high external surface area markedly reduce external coking, we demonstrate a similar effect for finned catalysts, focusing on two common 3-dimensional medium-pore zeolites: ZSM-11 (**MEL**) and ZSM-5 (**MFI**). The synthesis of ZSM-11 using (by) a previously reported protocol(204) yields crystals with relatively smooth exterior surfaces (Figure B1). We identified an alternative one-pot synthesis of ZSM-11 that produces crystals with finned surfaces (Figure 3.1b and c). Transmission electron microscopy (TEM) reveals that these are single crystals (Figure 3.1d) with an identical registry between the center of the particle and the exterior fins. These exterior features are aligned in parallel with an average dimension of 35 nm

(Figure 3.1e). Elemental analysis reveals no evidence of aluminum zoning (Table B1)(216), which has been reported for ZSM-5(217). Moreover, textural analysis (Figure B2) shows no evidence of mesoporosity in ZSM-11 samples, although TEM tomography reveals the presence of isolated pores within the interior of these particles (Figure B3 and Movie B1), which is likely (probably) attributed to the non-classical mechanism of zeolite growth involving (that involves) particle attachment(91, 97).

Prior studies have reported rough crystals of ZSM-11(218) and ZSM-5(219). The majority of these examples are structures with distinctly different features than those reported here. Notably, rough crystals in literature are commonly aggregates with small crystallites arranged in random orientations on the exterior surfaces of larger particles (Figure B4). These misoriented domains can give rise to pore blockage at the interfacial boundaries between adjacent particles; however, prior studies have demonstrated that these aggregated structures enhance the overall catalytic performance relative to that of conventional analogues, which is attributed to the introduction of interstitial mesopores(220). Here, we show that the one-pot synthesis of finned ZSM-11 improves catalyst properties owing to a different mechanism: enhanced mass transport through fins of a much smaller dimension (i.e. $\alpha \ll \beta$). Shen et al.(204) previously reported trends in catalyst lifetime and selectivity as a function of H-ZSM-11 crystal size (150, 300, and 750 nm) using methanol-to-hydrocarbons (MTH) as a model reaction. In Figure 3.1f, Time-on-stream (TOS) conversions over these three catalysts are compared to (with that of) the finned H-ZSM-11 sample (Figure 3.1f), which has an overall size of ca. 460 nm, fin included. Interestingly, the finned catalyst deviates from the trend of increasing lifetime with decreasing crystal size when comparisons are made on the basis of overall particle dimension; however, the trend is qualitatively consistent if the finned

catalyst behaves as a crystal of much smaller size, commensurate with that of the average fin dimension ($\alpha \approx 35$ nm).

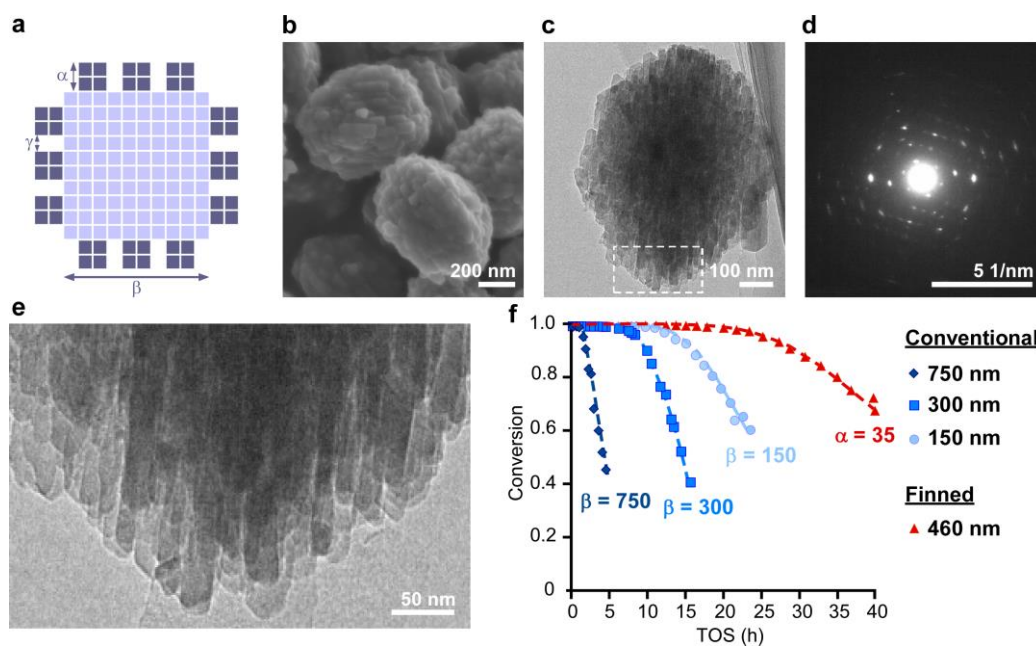


Figure 3.1. (a) Idealized schematic of a finned zeolite with fin and interior dimensions of α and β , respectively, and fin pitch γ . (b) SEM of zeolite ZSM-11 crystals with finned surfaces prepared from a one-pot synthesis (Table B2). (c) TEM of a representative finned ZSM-11 crystal. (d) Corresponding SAED pattern of the crystal in panel C showing a single-crystal pattern behaviour. (e) High-magnification TEM image from panel c (dashed box) showing the parallel alignment of fins. (f) TOS MTH conversion for H-ZSM-11 catalysts at 350 °C with WHSV = 9 h⁻¹.

3.3.2 Preparation of finned zeolites by secondary growth

The preparation of finned zeolite crystals via a one-pot synthesis is arbitrary and difficult to predict owing to the largely unknown impact of synthesis parameters on zeolite crystallization. To this end, secondary (or seeded) growth offers a more controlled method to create fins on the exterior surfaces of seed crystals. Here we demonstrate the secondary growth method for both ZSM-11 (Figure 3.2a–d) and ZSM-5 (Figure 3.2e–h). Scanning electron microscopy images of ZSM-11 (Figure 3.2a) and ZSM-5 (Figure 3.2e) seeds reveal exterior crystal surfaces devoid of rough features.

Scanning electron microscopy images after secondary growth of ZSM-11 (Figure 3.2b) and ZSM-5 (Figure 3.2f) confirm the presence of fins (protrusions). TEM images show average feature sizes of 30 ± 3 nm for ZSM-11 (Figure 3.2c) and 53 ± 6 nm for ZSM-5 (Figure 3.2g). Selected area electron diffraction (SAED) patterns (Figure 3.2d and h) also confirm that the samples are single zeolite crystals, which thus indicates that the fins grow epitaxially on the surfaces of the seeds. Powder X-ray diffraction (XRD) patterns indicate that the samples are fully crystalline before and after seeded growth (Figs. B5 and B6), whereas textural analysis (Table B3 and Figure B7) shows a slight increase in the total surface area ($\sim 8\%$) with secondary growth without an appreciable change in micropore volume (as shown in Table B3, the micropore volumes for finned and seed particles are indistinguishable). Elemental analysis (Table B3) also confirms that the Si/Al ratio of the samples before and after seeded growth are nearly identical.

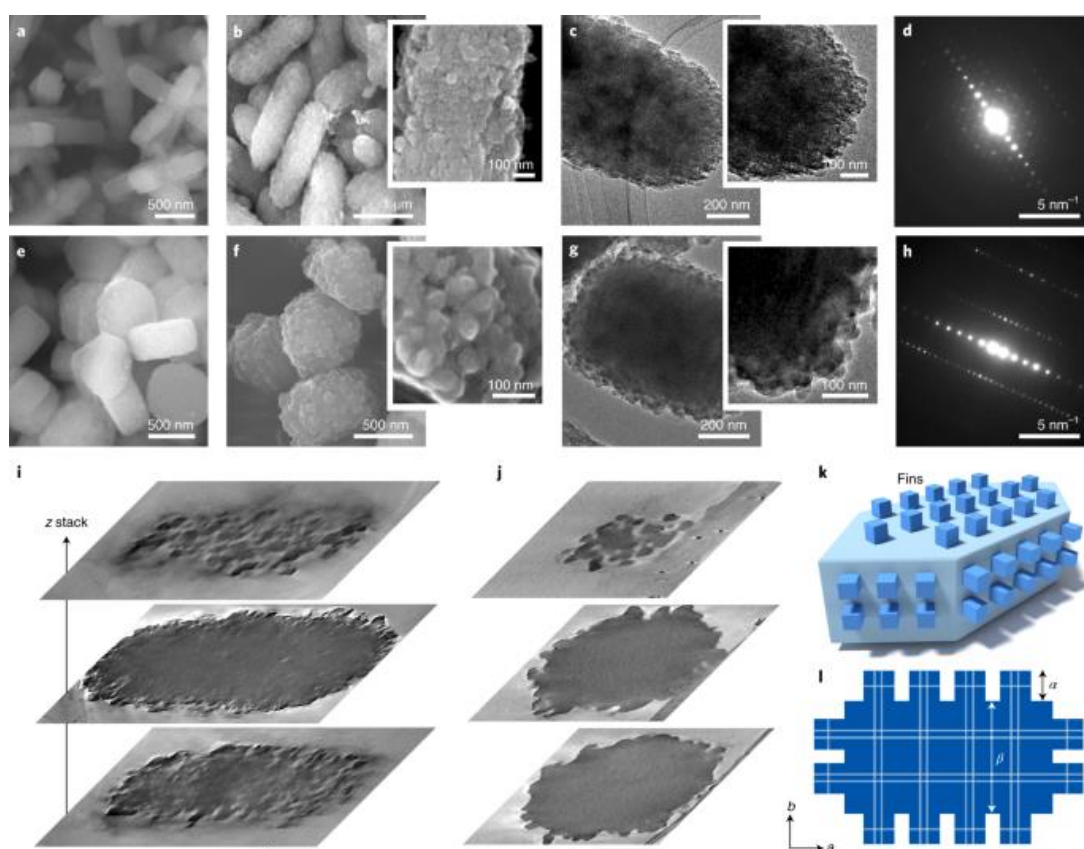


Figure 3.2. Electron micrographs of zeolite ZSM-11 (a – c) and ZSM-5 (e – g) crystals. SAED patterns (d and h) reveal that the finned zeolites are single crystals. (i and j) TEM tomography images of finned (i) ZSM-11 and (j) ZSM-5 crystals showing cross-sectional images from Movies B2 and B3, respectively. Scale bars equal 200 nm. (k) Idealized schematic of a finned zeolite in which the fins have the same crystallographic registry as the seed. (l) Illustration of a finned zeolite that comprised of continuous channels throughout the seed (size β) and fins (size α).

The protocol to generate finned zeolites was strategically selected by adjusting the supersaturation to a level that was sufficiently high to avoid layer-by-layer growth of core–shells (that is, complete overgrowth of seed crystals), which was previously demonstrated by Ghorbanpour et al.(221). However, there is an upper limit of supersaturation that, when exceeded, leads to the homogeneous nucleation of new crystals in the growth solution, and thereby generates aggregates of both small and large crystallites. TEM tomography of finned ZSM-11 (Figure 3.2i and Movie B2) and ZSM-5 (Figure 3.2j and Movie B3) after secondary growth confirmed the absence of intraparticle mesoporosity. TEM tomograms of each sample perpendicular to the z direction (z stacks), depicted in Figure 3.2i and j at the bottom, middle and top of the particles, clearly show the size and distribution of fins on the exterior surfaces. The finned zeolites prepared by secondary growth (Figure 3.2k) comprise regions with two characteristic dimensions: β is the size of the original seed along the principal zone axis of diffusion (that is b directions for **MFI** and **MEL**) and α is the average size of the fins. An idealized schematic of finned zeolites (Figure 3.2l) shows medium-pore channels that extend from the interior to exterior with an identical registry where the net increase in external surface area is highly dependent on the relative sizes of β and α (Figure B8).

Synthesis conditions for seed-directed synthesis of finned ZSM-5 and ZSM-11 were the result of parametric studies to determine optimal conditions for fin growth. For

instance, the use of lower temperature and/or reduced concentration of silica/alumina was found to inhibit secondary growth (within the timescales of synthesis). On the contrary, higher temperature and/or increased concentration of silica/alumina was found to promote homogeneous nucleation in growth solutions, resulting in a bimodal size distribution of particles rather than the generation of fins. The versatility of this synthesis approach was also tested for a range of seed and fin compositions (i.e., Si/Al = 30 – 60). The average mass yield of samples for this study is 800 mg, which is governed by the quantity of seeds used for secondary growth. To this end, the synthesis of finned zeolites can be easily scaled up via the adjustment of seed mass.

The total external surface area of finned zeolites can be defined by three geometrical descriptors: β (the average dimension of the seed crystal), α (the average size of fins), and γ (the average pitch between fins). Here we estimate scaling relations by making the following simplifying approximations: (1) The geometry of seed crystals and fins are cubes; (2) the mass density ρ of fins equal that of the seed; (3) pores are interconnected in all directions; and (4) the fins are equally spaced on the seed crystal (i.e. fixed values of γ). First, we consider a periodic array of fins with $\gamma = \alpha$ and calculate the approximate change in specific surface area of finned zeolites with fixed α and varying β . A cubic seed crystal has a surface area of $6\beta^2$, a mass of $\rho\beta^3$, and a specific surface area of $6/\rho\beta$. The projected area of a single fin (including the interstitial distance γ between fins) on a seed crystal is $4\alpha^2$ (i.e., $2\alpha \times 2\alpha$). Therefore, the total number of fins per seed crystal n is $1.5(\beta/\alpha)^2$ and the corresponding mass of fins per seed is $n\rho\alpha^3$. Each cubic fin adds an additional surface area of $4\alpha^2$, resulting in a net surface area $S_A = 6\beta^2 + 4n\alpha^2$ (per crystal) and a specific area of $S_A/(\rho\beta^3 + n\rho\alpha^3)$. In Figure B8, we plot the percent increase in specific surface area of a finned zeolite

compared to its corresponding seed crystal as a function of β . These calculations were performed using four different scenarios: small fins with $\alpha = 25$ nm spaced with small and large interstitial distances ($\gamma = 25$ and 50 nm, respectively); and larger fins with $\alpha = 50$ nm spaced with equivalent small and large interstitial distances. The general trend of specific surface area with increasing seed size is pseudo-logarithmic with values increasing and then reaching a plateau in the range $\beta = 250$ nm to 1.5 μm .

These calculations reveal distinct trends based on the ratio α/γ . We estimate that the net increase in specific surface area is more pronounced for larger fins with smaller separations ($\alpha = 50$ nm; $\gamma = 25$ nm), which leads to maximum 178% increase in surface area with the number of fins per area of seed crystal, $N = 0.25 \alpha^{-2}$, equal to 0.0002 nm^{-2} . In the two scenarios with $\alpha/\gamma = 1$, we estimate similar trends with a maximum 100% increase in specific surface area and N ranging from 0.0001 to 0.0004 nm^{-2} . The scenario leading to the least net increase in surface area is small fins and large pitch ($\alpha = 25$ nm; $\gamma = 50$ nm), which indicates the interstitial spacing between fins has a significant impact on surface area. Although increases in surface area by the growth of fins cannot solely account for the observed changes in mass transport and improved catalyst performance, these calculations do offer some insight into the rational design of finned zeolite geometry (α, β, γ). Moreover, these calculations offer some explanation for the $< 10\%$ increase in BET surface area for finned Zeolyst samples (Table B5) compared to ca. 40 and 70% increases (Table B3) for **MFI** and **MEL**, respectively. The larger increase in surface area for **MEL** is predicted based on its larger fin size relative to **MFI**.

3.3.3 Impact of Fins on Catalytic Performance

To substantiate the enhanced mass-transport properties of zeolites after secondary growth, we assessed the performance of the acid-exchanged (H-form) seed and finned samples in the MTH reaction at subcomplete methanol conversion (60–90%). The acid-site density and the framework Al of each catalyst was quantified (Table B3 and Figure B9) to ensure a consistent weight hourly space velocity (WHSV). TOS analysis of both seed and finned H-ZSM-11 (Figure 3.3a) and H-ZSM-5 (Figure 3.3b) samples reveals similar catalyst activity (that is, a nearly identical starting conversion). This suggests that the reactions in finned samples are not solely restricted to the exterior protrusions, but also occur within the interior of the catalyst. This is qualitatively consistent with the TEM and textural analyses showing the epitaxial growth of fins without a noticeable obstruction of the pores at the fin–seed boundary. For both crystal topologies, we observed an approximate threefold reduction in the rate of deactivation, which thus confirms that the presence of fins markedly extends the catalyst lifetime. Moreover, comparison of the product selectivities (Figure 3.3c and d) reveals a subtle shift whereby finned zeolites, which seemingly behave as pseudo nanocrystallites of dimension α , promote the olefin-based cycle of the MTH hydrocarbon pool (HCP) mechanism⁽⁵⁷⁾. Prior studies showed a progressive shift in the preferred cycle (from aromatic to olefin) with decreasing crystal size⁽¹³⁵⁾. This is clearly evident when the conventional descriptor ethylene/2MBu is compared, which is a ratio of the signature products from the aromatic-based cycle (ethylene) and olefin-based cycle (2MBu, 2-methylbutane and 2-methyl-2-butene). Over the entire range of the methanol conversion, we observed a noticeable reduction in the ethylene/2MBu ratio of finned catalysts (Figure 3.3e), which agrees with the expected trend for smaller particles.

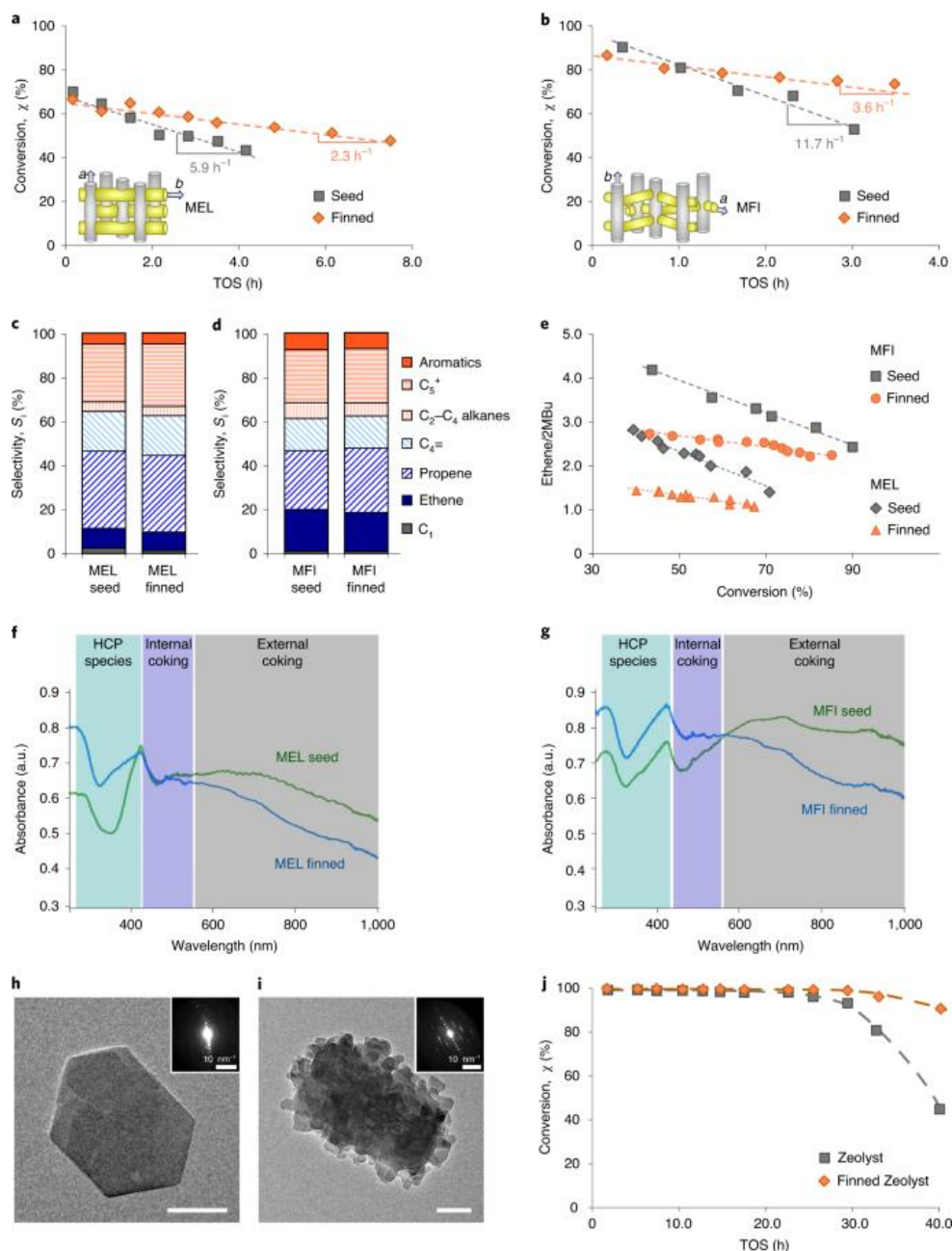


Figure 3.3. Plots of sub-complete methanol conversion over zeolite (a) H-ZSM-11 and (b) H-ZSM-5 catalysts during MTH catalysis as a function of time-on-stream (TOS). (c and d) Selectivities of hydrocarbon products for seed and finned (c) H-ZSM-11 and (d) H-ZSM-5 samples. (e) Ratio of ethylene to 2MBu (2-methylbutane and 2-methyl-2-butene) for the four set of samples. (f and g) Operando UV-Vis diffuse reflectance spectroscopy after 4 h TOS for (f) H-ZSM-11 and (g) H-ZSM-5 catalysts. (h and i) TEM images and SAED patterns of (h) Zeolyst CBV5524G and (i) the corresponding finned material prepared by secondary growth (see Figure B12 for additional images). Scale bars equal 100 nm (insets: scale bars equal 5 nm^{-1}). (J) TOS methanol conversion over as-received and finned commercial H-ZSM-5.

MTH reactions were repeated using operando ultraviolet–visible light (UV-vis) diffuse reflectance spectroscopy (DRS) coupled with online gas chromatography to track the spatiotemporal progression of the formation of hydrocarbon species in the zeolite crystals. It was previously shown⁽²²²⁾ that a UV-Vis spectrum obtained during MTH catalysis can be grouped into three distinct regions of wavelengths corresponding to HCP species as well as small and large polyaromatics. HCP species are reaction products small enough to diffuse through zeolite pores; small polyaromatics are associated with internal coke given that their size is sufficiently large to fit within zeolite pores, but too large to diffuse out of the zeolite; and large polyaromatics are attributed to external coke. The UV-vis spectra for H-ZSM-11 (Figure 3.3f) reveal equivalent internal coke between seed and finned samples; however, there is a noticeable reduction in the quantity of external coke for the finned sample, suggesting the presence of external protrusions leads to less accumulation of polyaromatics at (the) pore mouths. A similar trend was observed for H-ZSM-5 samples (Figure 3.3g), but with a shorter lifetime owing to the tortuous sinusoidal channels of **MFI** compared to the straight channels of **MEL** (insets of Figure 3.3a and b). Collectively, these studies indicate that finned catalysts enhance mass transport properties of the zeolite by suppressing the formation of external coke. This seemingly implies that olefins and small aromatics more readily diffuse through the fins, leading to reduced residence time of HCP species near the pore mouths.

One advantage of the finned synthesis approach is that it is theoretically applicable to a wide range of framework types. Moreover, this approach can be used to upgrade commercial catalysts via the addition of a secondary growth step. As proof of principle, we performed a seeded growth experiment using a commercial ZSM-5 sample from

Zeolyst (CBV5524G, Si/Al = 25). Electron micrographs of the as-received H-ZSM-5 reveal a heterogeneous particle size distribution with dimensions that span 100–250 nm (Figure 3.3h and Figure B12). Secondary growth of these particles successfully generated finned H-ZSM-5 with $\alpha = 35 \pm 5$ nm (Figure 3.3i and Figure B12). Elemental analysis (Table B5) also confirms that the Si/Al ratio of the samples before and after the seeded growth were nearly identical. MTH reactions at complete methanol conversion over as-received and finned catalysts reveal that the latter exhibits longer lifetime (Figure 3.3j) with expected trends in product selectivity (Figure B13), analogous to the synthetic seed and finned samples. Note that the preparation of ZSM-5 with a high Al content (Si/Al = 15–25) and sizes ranging from 2 nm (2D materials) to 100 nm (commercial samples) is largely inaccessible by conventional synthesis routes; however, the synthesis of finned zeolites offers a unique route to achieve pseudo-crystallites within this largely inaccessible size range.

3.3.4 Mass-transport Properties of Finned Zeolites

To confirm whether finned zeolites exhibit distinct mass-transport properties relative to conventional (seed) zeolites, we performed kinetic Monte Carlo (KMC) simulations to compare the diffusive behaviour of benzene (a relatively bulky, representative hydrocarbon molecule) in silicalite-1, the siliceous isostructure of ZSM-5, with preset α and β dimensions. The schematic in Figure 3.4a, which is not drawn to full scale, is a cross-section of the 3D model used in the KMC simulations in which each square represents a unit cell of silicalite-1 (unit cells that belong to the seed and fins are coloured light and dark blue, respectively). The simulated model contains $\sim 10^7$ unit cells. Benzene diffuses through the pore network of silicalite-1 via a series of infrequent hops between favourable adsorption sites in the framework's straight pores

(S), sinusoidal channels (Z) and at their intersections (I) (Figure 3.4a–c), which can be described by first-order kinetics. The KMC simulations of benzene hopping dynamics in silicalite-1 using rate constants from molecular modelling yield diffusivity estimates (Table B6) that are in good agreement with experiment(208, 223). We used this modelling approach to estimate the diffusion path length r , defined as the total trajectory length of a benzene molecule between first entrance and exit of the zeolite crystal, for seed and finned superstructures created by replication of the periodic **MFI** unit cell. For a seed crystal ($\beta = 500$ nm), the mean diffusion path length for benzene was $r = 138$ nm, which corresponds to a characteristic residence time of $\tau = 1.9 \times 10^{-5}$ s (Figure 3.4d and Table B7). When the surface was decorated with fins ($\alpha = 50$ nm) with a fixed pitch γ of 10 nm, we obtained $r = 58$ nm and $\tau = 7.9 \times 10^{-6}$ s (Figure 3.4d and Table B7). This 2.4-fold reduction arises from the comparatively shorter distance, relative to the seed crystal, required for diffusing molecules to enter and exit through the fins. Although the magnitude of the improvement depends on the fin surface density (Table B7), KMC simulations show that the finned structures exhibit superior mass-transport characteristics, consistent with experimental observations.

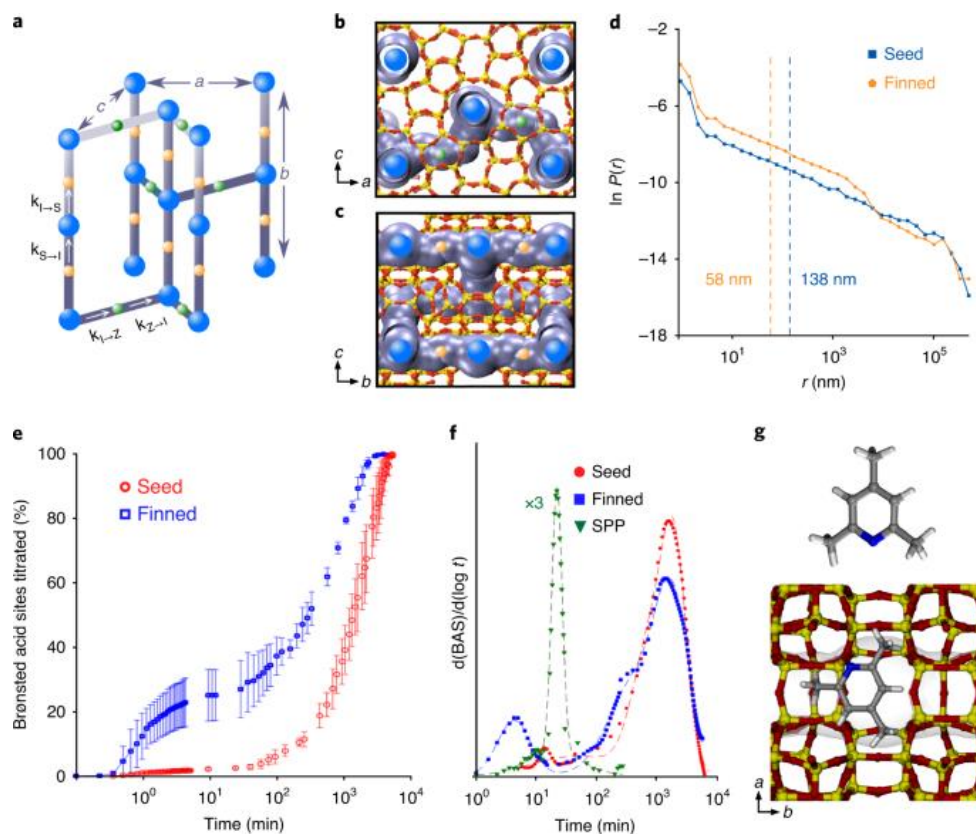


Figure 3.4. (a) KMC lattice representation of the pore network for the **MFI** unit cell. (b and c) Renderings along the *b* direction (b) and *a* direction (c) showing the KMC pore network superimposed on an atomistic unit cell. (d) Log probability density distribution of the benzene diffusion path length *r* for a finned zeolite and a seed crystal with a cubic geometry. (e) Time-resolved titration of Brønsted acid sites for H-ZSM-11 seed and finned samples. (f) Differential plot of titrated Brønsted acid sites in Zeolyst ZSM-5 (**MFI** type) seed and finned samples and SPP zeolite. (g) TMPyr structure and a snapshot from a molecular dynamics simulation (Movie B4) showing TMPyr within a **MEL** channel. Cage hopping in **MFI** is observed to proceed via a similar process (Movie B5).

The enhanced mass-transport properties of finned zeolites were further verified using an experimental protocol to assess internal diffusion based on time-resolved Fourier-transform infrared (FTIR) spectroscopy. In these studies, the purified bulky organic base 2,4,6-trimethylpyridine (TMPyr) was used to titrate Brønsted acid sites within zeolite micropores (Figure B14). Diffusion and adsorption of TMPyr slowly permeated the micropores of H-ZSM-11 and H-ZSM-5 over 3 days due to steric hindrance from the methyl groups(224). The temporal permeation of TMPyr was

quantified by the disappearance of FTIR intensity at $3,605\text{ cm}^{-1}$ which corresponds to the vacant Brønsted acid sites and also by the appearance of peaks at $1,565\text{ cm}^{-1}$ associated with the trimethylpyridinium ion (Figure B15). The loss of Brønsted acid sites is linearly correlated to the increase in trimethylpyridinium ions (Figure B16). The distinct TMPyr uptake kinetics for H-ZSM-11 (Figure 3.4e) and H-ZSM-5 (Figure B17), both with and without fins, are described by an exponential diffusion model. When the differential of the titrated Brønsted acid sites over time was plotted for the Zeolyst samples (Figure 3.4f) and other zeolites (Figure B18), we observed the two distinct diffusion regimes, which indicates the initial fast uptake of TMPyr in the fins relative to the bulk particle. To further assert the correspondence of the two timescales to the finned and bulk portions of the crystals, we also applied the method to examine a self-pillared pentasil (SPP) zeolite, which consists of intergrown few-nanometre-thick **MFI** nanosheets (that is, it has a uniform micro- and mesopore hierarchical structure throughout each particle), and as such it should exhibit only one (fast) timescale. Indeed, we obtained one diffusion regime, albeit somewhat slower than the fast one obtained in the finned samples, which indicates possible contributions of mesopore resistances in the SPP zeolite (Figure 3.4f). Molecular dynamics simulations also confirmed that TMPyr is of sufficient size to fit within the channels of both **MEL** (Figure 3.4g) and **MFI** (Figure B19) frameworks.

Table 3.1. Elemental analysis of zeolite catalyst samples.

Sample	τ_{fast} (s)	τ (s)
MEL-Seed	n.a.	6.6×10^5
MEL-Finned	2.4×10^2	6.7×10^4
MFI-Seed	n.a.	2.6×10^5
MFI-Finned	4.4×10^2	1.2×10^5
Zeolyst	n.a.	4.5×10^4
Finned Zeolyst	3.1×10^2	4.2×10^4
SPP	1.7×10^3	n.a.

Experimental points in TMPyr titration curves (Figure B20) were fitted using an exponential model to obtain time constants for fast (τ_{fast}) and slow (τ) diffusion within the finned and interior micropore regions, respectively (Table 3.1). The finned zeolites exhibit an initial rapid uptake kinetics three orders of magnitude faster than the seed. These trends are qualitatively consistent with kMC models and catalytic studies, which show distinct transport properties of finned zeolites in which the introduction of protrusions with size $\alpha \ll \beta$ markedly reduced the internal diffusion limitations. Time-resolved titration measurements also reveal that this disparity in time constants is maintained for nanocrystals in which the differences between α and β are less substantial (for example, Zeolyst H-ZSM-5 in Figure 3.3h and i).

3.4 Summary

There is growing evidence for the advantages of synthesizing nanosized zeolites with markedly reduced internal diffusion limitations for enhanced performances in catalysis and adsorption. Producing zeolite crystals with sizes less than 100 nm, however, is non-trivial, often requires the use of complex organics and typically results in a small product yield. There are few synthesis methods capable of producing ZSM-5 and ZSM-11 crystal sizes in the range 10–80 nm. Conversely, methods to produce 2D crystals with sizes <10 nm often result in insufficient acid-site density (for example, Si/Al > 40) for industrial hydrocarbon catalysis. Moreover, ultrasmall crystallite sizes pose practical challenges for solids extraction in commercial synthesis processes. The generation of finned zeolites overcome these restrictions and challenges by altering the performance of large crystals to behave as pseudo-nanocrystals. Using a synergistic combination of state-of-the-art experimental techniques, we show that finned ZSM-5 and ZSM-11 zeolites possess unusually outstanding mass-transport properties.

Markedly enhanced rates of molecular uptake in fins, coupled with reduced internal diffusion path lengths, leads to less coke formation on external surfaces, longer catalyst lifetimes and a shift in the product selectivities that are characteristic of zeolites with an overall crystal size equal to that of the average fin dimension. The ability to introduce fins through a facile secondary growth process is an alternative method to reduce diffusion limitations in zeolites. Here we demonstrate that this approach can be used to enhance the performance of commercial catalysts, with the promise of becoming a generalized platform for the rational design of zeolites across a broad range of framework types.

Chapter 4

Enhanced Selectivity and Stability of Finned Catalysts with Two-dimensional Pores

The manuscript of this research work is submitted. The work is in collaboration with Prof. Paul J. Dauenhauer from University of Minnesota; Prof. Xiujie Li from Dalian Institute of Chemical Physics; Dr. Taimin Yang and Prof. Xiaodong Zou from Stockholm University.

4.1 Motivation

The confined channels and cages of zeolites and zeotypes have been widely used as shape-selective catalysts and absorbents in numerous commercial processes due to their unique properties, such as (hydro)thermal stability, tunable acidity, and versatile pore topologies(20, 22). A common objective in the design of zeolite catalysts is overcoming the inherent mass transport limitations of micropores. Advancements in the synthesis of two-dimensional (2D)(153–155), self-pillared(179, 181), hierarchical (e.g., mesoporous)(162, 163), and nanosized(201, 225) zeolites have revealed their superior catalytic performance relative to conventional analogues owing to reduced internal diffusion pathlength and increased external surface area (i.e. more accessible acid sites). The majority of these advancements have focused on the optimization of zeolites with three-dimensional pores; however, the frameworks with the most restrictive mass transport are zeolites with one- and two-dimensional pore networks. Methods to optimize one-dimensional materials include post-synthesis modification to introduce mesopores(226, 227) or relatively few cases where the judicious selection of synthesis parameters leads to nanosized crystals(228). Two-dimensional zeolites are either layered materials(160, 229) or structures that are amenable to the generation of nanosheets(230–232) with thicknesses less than a few unit cells of the crystal structure;

however, diffusion is orthogonal to these directions where the enhanced external surface area of promotes reactions involving bulky (sterically-hindered) molecules, but does little to mitigate internal mass transport limitations.

In this chapter, we examine the synthesis and catalytic performance of ferrierite (**FER**), which is a two-dimensional zeolite with interconnected small (8-ring, 3.5×4.8 Å) and medium (10-ring, 4.2×5.4 Å) pore apertures. Ferrierite is a commercial catalyst that is used in isomerization(233–236) and other reactions(237, 238) owing to its unique pore topology that includes intersections of two disparate pore sizes and cavities within the smaller channels that can promote shape-selective reactions. Restricted diffusion through two-dimensional pores makes ferrierite more susceptible to rapid deactivation from coke formation (i.e. pore blockage)(239). To our knowledge, ferrierite crystals have not been synthesized with dimensions less than 100 nm in both the b- and c- directions (parallel to 8- and 10-ring pores, respectively). There have been examples where particles (or aggregates of particles) are comprised of smaller domains or protrusions with dimensions less than 100 nm through the judicious selection of organic structure-directing agents (OSDAs). Corma and coworkers(202) produced ferrierite catalysts with a length of 10–30 nm using two cooperative OSDAs and reported their enhanced lifetime in 1-pentene oligomerization. Hong and coworkers(233) synthesized needle-like ferrierite crystals with sizes of ca. 10 nm using choline as the OSDA; and Xiao and coworkers(235) reported an alternative OSDA capable of inhibiting growth in the a-direction to generate ultrathin nanosheets (6–8 nm in the direction orthogonal to diffusion). Other studies have successfully synthesized ferrierite crystals with sizes on the order of 100 nm(236). Alternative techniques include post-synthesis treatment (e.g., delamination) of layered FER precursor (PREFER)(229, 240) or the generation

of hierarchical structures by dealumination or desilication(241, 242). However, these methods reduce micropore volume and often result in the loss of crystallinity.

We recently discovered a new class of hierarchical ZSM-5 (MFI) and ZSM-11 (MEL) catalysts referred to as “finned” zeolites(243). It was demonstrated for these three-dimensional zeolites that the epitaxial growth of fin-like protrusions on seed crystals dramatically enhanced mass-transport properties and catalyst lifetime in the methanol-to-hydrocarbon (MTH) reaction. Here, we extend this general concept to the synthesis of ferrierite and test the hypothesis that ultrasmall fins (<50 nm) on this two-dimensional zeolite markedly enhance catalyst turnovers and product selectivity. In this chapter, our findings revealed that ferrierite crystals can be prepared with tunable fin size to transform seeds into pseudo nanoparticles with improved mass transport properties. This phenomenon was validated for both synthetic and commercial ferrierite seeds where we observed that the introduction of fins leads to sizable increases in catalyst turnovers and isobutene selectivity compared to non-finned counterparts.

4.2 Experimental Methods

4.2.1 Material

Zeolite synthesis was performed with the following reagents: LUDOX AS-30 (30% suspension in H₂O, Sigma-Aldrich), sodium hydroxide (NaOH, > 98%, Sigma-Aldrich), potassium hydroxide (KOH, 1M, Fisher Chemical), Catapal B alumina (72% Al₂O₃, Sasol), aluminum sulfate (Al₂(SO₄)₃·18H₂O, 98%, Sigma-Aldrich), cyclohexylamine (CHA, ≥99%, Aldrich), and pyrrolidine (Pyr, 99%, Aldrich). Time-resolved acid titration experiments were performed using 2, 3-dimethylpyridine (Sigma-Aldrich, 99%). All reagents were used as received without further purification.

Deionized (DI) water, used in all experiments, was purified with an Aqua Solutions Type I RODI filtration system (18.2 M Ω). For reaction testing, 1-butene (99.9%) and nitrogen (99.99%) were purchased from Dalian Special Gases Co., Ltd.

4.2.2 Zeolite Catalyst Preparation

The ferrierite seed was hydrothermally synthesized with a molar composition of 4.8 NaOH: 1.0 Al₂O₃: 20 SiO₂: 5.0 CHA: 1.2 KOH: 750 H₂O. In a typical synthesis, the sodium aluminate solution was premade at 165 °C for 6 h by mixing with Catapal B alumina, NaOH and water. Then 7.22 g (0.036 mol) of LUDOX AS-30 was added to a mixture of a sodium aluminate solution (15.1 wt. % Na₂O, 16.8 wt. % Al₂O₃, 0.0018 mol) and 15.49 g (1.35 mol) of DI H₂O. To this solution was added 0.05 g NaOH solution (10 wt. %, 0.0086 mol) and 0.24g KOH solution (50 wt. %, 0.0022 mol), followed by the organic structure-directing agent (OSDA) cyclohexylamine (CHA, 0.90 g, 0.0090 mol). The resulting mixture was stirred at room temperature to get homogenous solution. The gel solution was placed in a 60 ml Teflon liner within a metal autoclave (Parr Instruments) that was sealed and heated in a Thermo Fisher Precision oven at temperature T = 165 °C and autogenous pressures. The autoclave was removed from the oven after 2 days synthesis and was quenched in water to room temperature. The sample was washed for three times without drying. A growth solution was made to grow on ferrierite seed with a molar composition of 6.2 Na₂O: 0.71 Al₂O₃: 20 SiO₂: 14 Pyr: 800 H₂O. The solution was prepared by mixing approximate amount of Al₂(SO₄)₃·18H₂O and DI water, followed by LUDOX AS-30 and NaOH additions. At last, the OSDA pyrrolidine (Pyr) was added to the gel solution. The solution was stirred at room temperature for 3 h. Then, 20 wt. % of ferrierite wet seed was added to the solution for the secondary growth. The suspension was placed in Teflon liner within

an autoclave and heated for 24 h at different temperatures (120 °C to 140 °C) and then quenched to room temperature. The solution was then removed from the oven and the solid was dried in air after centrifuge washing for further analysis. The finned commercial sample was synthesized at 130 °C, following the similar procedure except the use of the Zeolyst CP914C as the seed.

4.2.3 Characterization

As-synthesized materials were characterized by powder X-ray diffraction (PXRD) using a Rigaku SmartLab diffractometer with Cu-K α radiation (40 kV, 44 mA) to verify the crystalline structure. Powder XRD patterns acquired from 5° to 50° 2 θ with a step size of 0.02° were compared to simulated patterns of **FER** framework type provided by the International Zeolite Association Structure Database(6). Scanning electron microscopy (SEM) was performed with a FEI 235 dual-beam (focused ion-beam) system operated at 15 kV and a 5 mm working distance. All SEM samples were coated with a thin platinum layer (ca. 5 nm) prior to imaging to reduce the effects of charging. Textural analysis of H-form samples prepared for catalytic testing was performed by N₂ adsorption/desorption using a Micromeritics ASAP 2020. The data was analyzed by instrument software to obtain the BET surface area and the microporous volume was determined from the t-plot method. The molar Si/Al ratio of all ferrierite samples was measured by inductively coupled plasma analysis in combination with optical emission spectroscopy (ICP-OES). Before analysis, approximate 50 mg of the sample was fused with LiBO₂ (98.5 wt% lithium metaborate and 1.5 wt% LiBr) by Katanax X-300 Fusion Fluxer instrument. The mixture was heated to 1000 °C for 15 min. Then 50 mL 2 N HNO₃ was added to the molten mixture and stirred for 10 min. Agilent 725 instrument was used to analyze the elemental components of the samples. Aluminum speciation

was determined from ^{27}Al MAS NMR spectra collected at a spinning frequency of 12.5 kHz, pulse of $\pi/12$, relaxation delay of 0.8 s, and 4 K scans at 11.7 T on a JEOL ECA-500 spectrometer. Before the ^1H MAS NMR measurements, all the samples were dehydrated at 400 °C and at a pressure below 10^{-2} Pa for 20 h. Spectra were collected at 600.13 MHz using single-pulse sequence with p/4 pulse, 4 s recycle delay. For the determination of quantitative results, all samples were weighed, and the spectra were calibrated by measuring a known amount of adamantane performed under the same conditions.

The samples for transmission electron microscope (TEM) investigations were dispersed in ethanol. After ultrasonication of the suspension, a droplet was taken and transferred to a lacey carbon copper grid. Then the droplet was dried in air at room temperature. TEM images and selected area electron diffraction (SAED) patterns were collected on a JEOL JEM-2100F microscope operated at 200kV (Cs 1.0 mm, point resolution 0.23 nm) using a Gatan Orius 200D CCD camera (resolution 2048 x 2048 pixels, pixel size 7.4 μm). 3D electron diffraction (3DED) and electron tomography datasets were collected on a Thermo Fisher Themis-Z TEM operated at 300 kV with a Gatan OneView camera. A Fischione model 2020 advanced tomography holder was used to engage the copper grid. The 3DED datasets were collected by *Instamatic* software(244) and then the 3D reciprocal lattices were reconstructed and visualized by *REDp* software(245). The collection of electron tomography dataset was done in TEM mode using *TEM Tomography* software, which allows automatic focusing and tracking of the target. 5 nm gold nanoparticles were used as fiducial marker for tomogram alignment. The tomography datasets were processed by *ETomo* software(246), in which tilt series alignment and 3D reconstruction were performed.

Time-resolved spectra were measured using a Fourier-transform infrared spectroscopy (FTIR) with a HeNe laser and RT-DLaTGS detector (Bruker Vertex 70, 20 kHz scanner velocity, 6 mm aperture, KBr beam splitter). For sample preparation, about 15 mg of powder catalyst sample was homogenized using an agate mortar and pestle, pressed (Pike Technologies, CrushIR Digital Hydraulic Press) at ~3 ton for 5 min into 13 mm-diameter pellets (International Crystal Laboratories, KBR Die, CAS no.7758-02-3) and inserted into the cell body (Harrick Scientific, High Temperature Cell, Part no. HTC-M-05, CaF₂ windows). Before inserting each sample pellet, a background spectrum was collected (64 scans, 4 cm⁻¹ resolution) with the empty cell. A K-type thermocouple (Harrick Scientific, Part No. 008-144) was in constant intimate contact with the sample pellet holder to measure the temperature. The manufacturer-provided cartridge heater (100 W, 24 V) was controlled via a temperature controller in cascade mode (Omega CN7800). To ensure that the CaF₂ windows of the sample cell does not overheat, cooling water was continuously pumped (Control Company, Variable Flow Chemical Pump) and flowed through water cooling ports connected to the cell body. The sample was calcined at 500°C for 4 h in air (Linde, Air Ultra Zero) at a ramp rate of 1°C min⁻¹. After calcination, the sample was cooled down to and remained at 240 °C for the duration of the experiment to ensure the absence of water. Cold 2,3-dimethylpyridine (Sigma-Aldrich, CAS no. 583-61-9) was used for dosing in FTIR. For the amine dosing process, He gas (Minneapolis Oxygen Company, Grade 5.0 He, UN1046) was flowed over the sample pellet to purge any remaining air. To ensure that the He is moisture-free, He gas was flowed through a liquid nitrogen trap and desiccator before reaching the cell body. The initial spectrum of the calcined catalyst was measured at this time, with the background spectrum subtracted. 2,3-dimethylpyridine was flowed at 0.06 ml h⁻¹ to the sample cell. FTIR spectra (64 scans,

4 cm⁻¹ resolution, scan range from 4000 to 1000 cm⁻¹) were saved continuously at different time intervals during the duration of the experiment: every 30 s for the first 30 min, then every 10 min for the rest of the experiment.

4.2.4 Catalytic Measurements

The skeletal isomerization of 1-butene to isobutene was carried out in a fixed bed micro-reactor with an inner diameter of 7 mm under atmosphere pressure. In a typical run, 0.15 g of catalyst was diluted with quartz sand to 0.5 g and put into the center of the reactor. The catalyst was activated at 500 °C in continuous nitrogen flow for 2 h. Then the temperature was cooled down to 400 °C. The mixture flow of 1-butene with nitrogen was fed into the fixed bed. The molar ratio of 1-butene to nitrogen was 1:1 and weight hourly space velocity (WHSV) of 1-butene was 12 h⁻¹. The reaction products were analyzed online by an Agilent 7890B gas chromatograph equipped with a flame ionization detector (FID) and an Al₂O₃ capillary column. To compare the catalyst performance in 1-butene isomerization reaction, the turnover number (TON) is calculated for a selected range of time on stream (TOS) using a modified form of the equation as(247)

$$TON(t) = \frac{1}{[H^+]} \int_{t_1}^{t_2} F(\tau) d\tau. \quad (4.1)$$

where [H⁺] is the concentration of Brønsted acid sites and F(τ) is the experimental trend of molar flow rate of all hydrocarbon products as a function of time on stream evaluated between two times (t₁ and t₂).

4.3 Results and Discussion

4.3.1 Preparation of Finned Ferrierite Zeolites

Ferrierite (**FER** type) zeolite is comprised of two-dimensional pores, as illustrated in Figure 4.1a. Medium-sized pores with a 10-membered ring (MR) aperture are oriented axially along the b-direction and intersect small-sized pores with 8-MR aperture oriented along the c-direction. Using an approach similar to a previous study of zeolites **MFI** and **MEL**(243), we prepared a series of finned FER zeolites. In this chapter, we synthesized seeds with relatively monodisperse size distribution (Figure 4.2a) using a reported protocol(236) with slight modifications. Crystallization of ferrierite resulted in a platelet morphology, as is typical of 2D zeolites, where pores are accessible on low surface area facets (i.e., edges with thickness < 100 nm) and a nonporous basal surface in the [100] plane. For illustrative purposes, the schemes in Figure 4.1a and b highlight porous and nonporous facets as purple and grey shaded regions, respectively. Secondary growth of ferrierite seeds in mixtures at various synthesis conditions (Table C1) result in three-dimensional growth of protrusions (referred to as fins) from all surfaces of the platelet. Fins that populate the basal surface (Figure 4.1b) have a pore network that is disconnected from that of the seed, rendering each of these fins an isolated nanoparticle. In contrast, fins populating the edges of the platelet (Figure 4.1c), which are in crystallographic registry with the seed (*vide infra*), have their 2-D network of pores oriented such that they are interconnected with pores in the seed. Herein, we refer to β as the width of seed platelets (b \times c dimension), where β of 820 ± 46 nm; we refer to α as the average size of fins, which are approximately isotropic in shape with α of 25 to 50 nm. The average spacing between fins, labelled as γ in Figure 4.1c, is 10 – 30 nm.

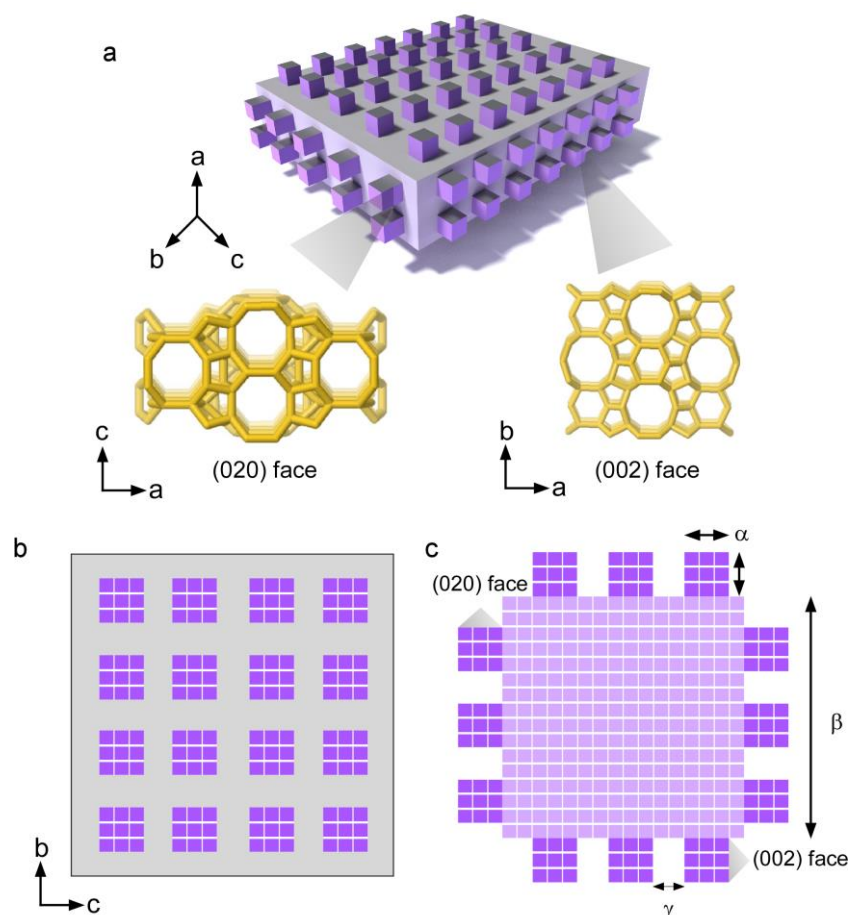


Figure 4.1. (a) Idealized schematic of a finned ferrierite (**FER**) zeolite. (b) Fins located on basal (200) facets are isolated nanoparticles with pore networks disconnected from the seed crystal. (c) Illustration of a finned zeolite along a cross-sectional (200) plane with fins located on the (020) and (002) facets.

Parametric analysis of secondary growth conditions revealed that the fin size α can be tuned by changing synthesis temperature. All syntheses used identical seeds, which are referred to as sample FS (Figure 4.2a). We prepared three finned ferrierite samples of increasing fin size using synthesis temperatures of 120 °C (Figure 4.2b), 130 °C (Figure 4.2c), and 140 °C (Figure 4.2d); these samples are referred to as FSF1, FSF2, and FSF3, respectively. Scanning electron micrographs show that the lowest temperature for seeded growth results in a lower coverage of fins (Figures 4.2b and Figure 4.3a) compared to the two samples prepared at higher temperature. Moreover,

an increase in temperature leads to a monotonic increase in the average fin size α , as shown in Figure 4.2e. Powder X-ray diffraction patterns of all samples (Figure C1) indicate complete crystallinity without evidence of impurities. Textural analysis revealed that both seed (FS) and finned (FSF1, FSF2, and FSF3) samples have similar micropore volume (Table C1) with type IV isotherms (Figure C2) confirming the absence of mesopores after secondary growth. The increased size and coverage of fins with increased synthesis temperature results in a maximum external surface area corresponding to sample FSF2 (Table C1). Elemental analysis indicates that the compositions of both seed and finned samples are nearly identical (Si/Al ratio = 9.2 ± 0.4 , Table C1). We also checked for potential zoning,^(248, 249) which is a known phenomenon where mesoscopic gradients in Si/Al ratio can lead to either Si- or Al-rich exterior rims of zeolite crystals. Comparison of the bulk composition measured by inductively coupled plasma optical emission spectrometry (ICP-OES) to that of the surface measured by X-ray photon spectroscopy (XPS) shows mild Si-zoning for samples FS and FSF1 (Table C1) and no appreciable differences for finned samples FSF2 and FSF3.

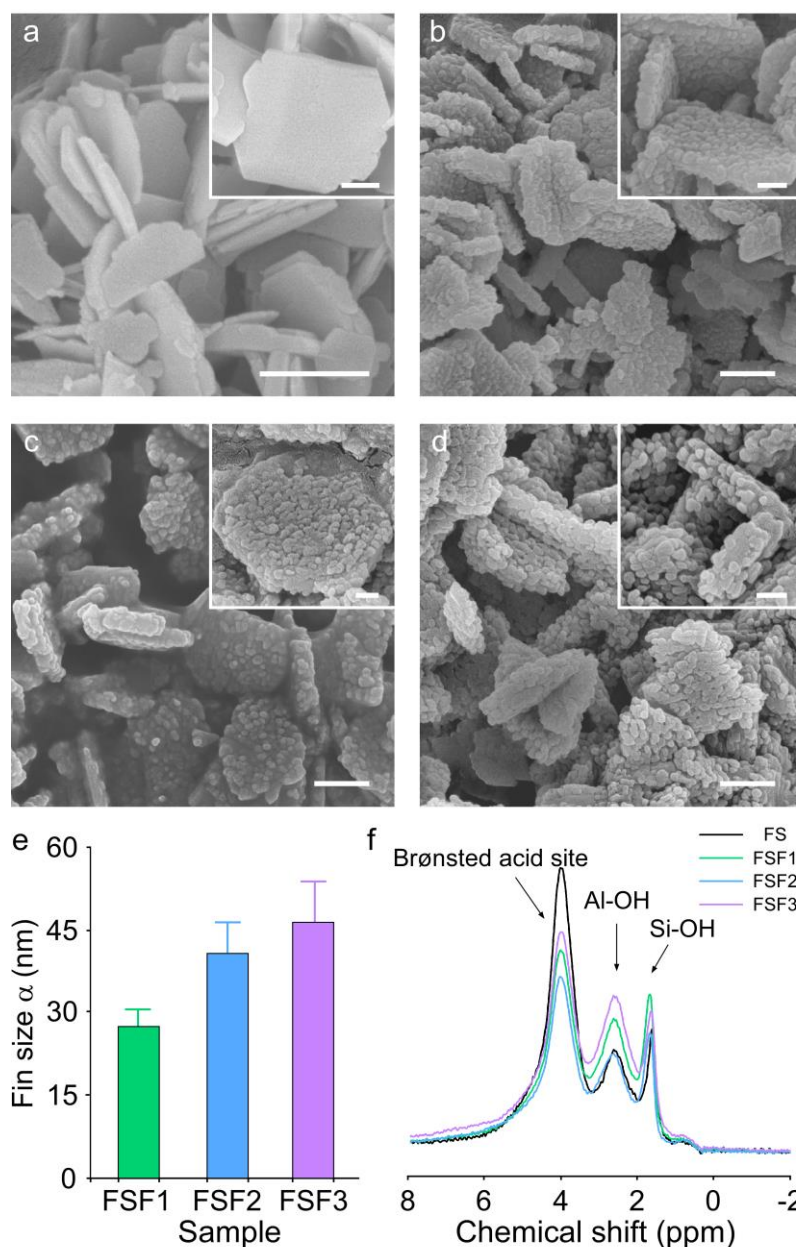


Figure 4.2. (a) Tunable fin size on **FER** crystals. (a – d) Scanning electron micrographs of (a) seed and (b – d) finned crystals prepared at three different synthesis temperatures: (b) 120 °C (FSF1), (c) 130 °C (FSF2), and 140 °C (FSF3). Scale bars equal 500 nm. Insets: high magnification images of representative crystals. Scale bars equal 200 nm. (e) Comparison of fin size α for the three finned **FER** samples. (f) Solid state ^1H MAS NMR analysis of H-form zeolites prepared for catalyst testing.

Transmission electron microscopy (TEM) confirmed the epitaxial growth of fins on seed crystal surfaces. TEM analysis of sample FSF1 captured images of platelets oriented normal to the basal surface (Figure 4.3a) and crystal edge (Figure 4.3c). Both

of these facets are laden with fins, confirming secondary growth occurs on all facets of FS seed crystals (Figure C3). Select area electron diffraction (SAED) of each crystal orientation (Figure 4.3b and d, respectively) confirms that fins are in crystallographic registry with the underlying seed crystal; thus, the conditions reported in this study lead to epitaxial growth of fins. The systematic absences of electron diffraction patterns also confirmed the *Immm* space group of the **FER** framework (Figure C4 and Movie C1), consistent with the expected structure(250). This was also confirmed in SAED patterns for samples FSF2 (Figure C5) and FSF3 (Figure C6). The distribution of fins on external facets was assessed by TEM tomography wherein two-dimensional planes of target crystals were computationally reconstructed along the z direction (z stacks), which is parallel to the (200) crystal plane of the finned samples. Representative z-stack images of sample FSF2 are shown for planes imaged near the bottom, middle, and top of the platelet (Figure 4.3e and Movie C2). Similar tomography tilt series were collected for samples FSF3 (Figure 4.3f and Movie C3) and FSF1 (Movie C4). In all three finned samples, TEM analysis reveals a relatively uniform coverage of fins on all crystal facets with average sizes that are consistent with those measured by SEM analysis (Figure 4.2e). Moreover, the increased coverage of fins with increasing synthesis temperature was also evident in TEM images and reconstructed tomography z stacks.

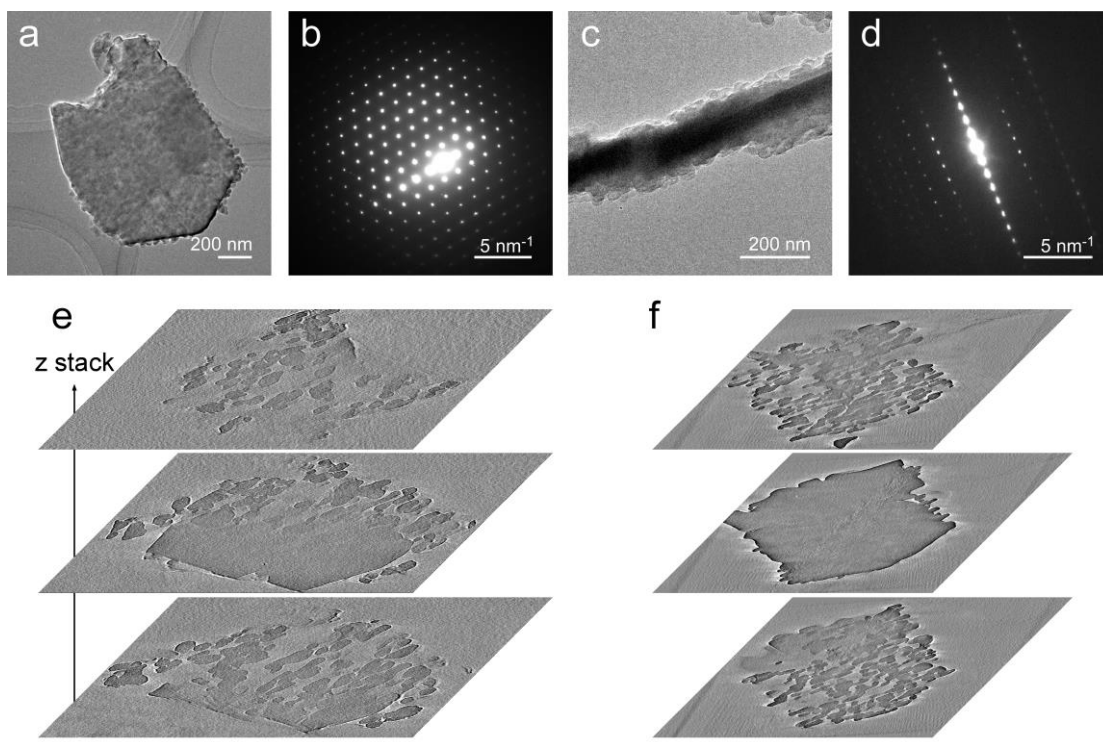


Figure 4.3. (a) Transmission electron micrographs of sample FSF1 along the (a) facing the sheet and (c) from the edge, respectively. SAED patterns (b and d, respectively) reveal a single crystal. (e, f) TEM tomography images of representative crystals from samples (e) FSF2 and (f) FSF3 showing cross-sectional images along the z direction (see Movies C2 and C3, respectively). Scale bars equal 500 nm.

As evidence for generating finned ferrierite zeolites to benchmark catalysts in performance testing (described in the next section), we selected a commercial ferrierite from Zeolyst (CP914C) as a seed and generated a finned analogue using similar secondary growth mixtures at 130 °C. We refer to seed and finned samples as FC and FCF, respectively. The physicochemical properties of these materials (Table C1 and Figure C1) are similar to the samples synthesized in house with respect to composition (Si/Al ratio), surface area, and crystallinity. SEM images of the as-received FC sample reveal a heterogeneous size distribution of ferrierite crystals (Figure C7) with β spanning from 400 to 800 nm. Electron microscopy imaging of the finned sample FCF (Figure C7) reveals a fin size (36 ± 12 nm) and coverage similar to sample FSF2. The

SAED patterns for FCF (Figure C8) also confirm its single crystal structure, indicating epitaxial growth of fins on seed surfaces.

4.3.2 Catalytic Testing of Finned Ferrierite Catalysts

All synthetic and commercial seed and finned ferrierite samples were ion exchanged with NH_4^+ and calcined according to an established protocol(243) to generate H-form catalysts. The acidity and aluminum speciation of the catalysts were characterized by multiple techniques. The quantity of Brønsted acid sites (BAS) could not be determined by a combination of ammonia temperature programmed desorption (NH_3 -TPD) and pyridine Fourier transform infrared (FTIR) analyses owing to the inability of bulky pyridine molecules to access acid sites within small 8-MR pores; therefore, we used solid state ^1H MAS NMR (Figures 4.2f) along with a common standard (adamantane)(251) to quantify BAS concentration (Table C1) based on chemical shift in NMR spectra (ca. 4 ppm) related to framework Al. The percentage of extra-framework Al (EFAI) was obtained by solid-state ^{27}Al MAS NMR (Figure C9), where we observe a relatively narrow range of values spanning 7 to 12% (Table C1) with no discernable trends observed among seed and finned samples. Moreover, the general trend in BAS concentration is difficult to ascertain given that all in-house finned samples (FSF1, FSF2, and FSF3) have notably smaller values compared to the parent seed (FS), whereas the finned commercial sample (FCF) has a slightly higher BAS concentration compared to its parent seed (FC). To account for the subtle differences in acidity we report the turnover number (TON), which accounts for the BAS concentration of each catalyst.

Table 4.1. Physicochemical properties of seed and finned H-form zeolite **FER** samples.

Sample ^a	BET S_A (m^2/g) _b	S_{ext} (m^2/g) _b	V_{micro} (cm^3/g) _b	Si/Al (bulk) ^c	Si/Al (surface) ^c	BAS ($\mu mol/g$) ^d	EFAI ^e (%)	τ_{fp} ^f (min)
FS	354	73	0.11	8.7	11.5	750	9.5	14.0
FSF1	387	106	0.11	9.5	11.8	590	8.5	21.5
FSF2	391	134	0.11	9.4	9.3	510	7.1	17.0
FSF3	389	99	0.12	9.1	9.7	670	12.1	28.0
FC	369	37	0.13	10	10.6	540	6.9	n.a.
FCF	362	41	0.13	10.2	11.0	580	7.8	37.5

^a FS = synthesized **FER** sample, FC = commercial **FER** sample (Zeolyst CP914C); ^b N_2 adsorption/desorption measurements of BET total surface area (S_A), external surface area (S_{ext}), and micropore volume (V_{micro}) after calcination and prior to ion exchange; ^c Elemental analysis of bulk and surface Si/Al measured by ICP-OES and XPS, respectively; ^d BAS = Brønsted acid sites measured by 1H MAS NMR; ^e EFAI = extra-framework aluminum measured by ^{27}Al MAS NMR; ^f Fast time scale (first peak maximum) from time-resolved titration of Brønsted acid sites by 2,3-dimethylpyridine.

For catalytic testing we selected 1-butene isomerization as a benchmark reaction to assess the effects of fins. The desired product from this isomerization reaction is isobutene (Figure 4.4a) with a variety of undesirable side products that include propene and pentene, among others. Catalyst testing was performed at sub-complete conversion of 1-butene (initial conversion of ca. 60%) in a fixed bed reactor at 400 °C using a weight hourly space velocity of 12 h^{-1} . The TON was evaluated from the conversion versus time on stream curve of each catalyst (Figure C10) within a fixed range of 45 to 55% conversion. The parent seed FS has a TON of 5600 (Figure 4.4b) while the three finned samples (FSF1, FSF2, and FSF3) exhibited a nearly two-fold increase in turnover number (spanning 9600 to 11500). The most effective catalyst was FSF2, which had the lowest BAS concentration among finned samples but also had the highest external surface area and lowest percentage of EFAI (Table C1). The presence of EFAI species can have a deleterious effect on catalyst performance(252), whereas the external

surface area can enhance molecule entry and exit from zeolite pores, thereby reducing the rate of catalyst deactivation by coking. This indicates that the synthesis temperature during secondary growth of fins is critical for catalyst preparation, with the intermediate temperature of 130 °C used to prepare FSF2 being the most optimal condition.

In literature it has been proposed that 1-butene isomerization involves three possible mechanisms: monomolecular, bimolecular, pseudo-monomolecular(253). It has been hypothesized that catalyst deactivation is attributed to the pseudo-monomolecular mechanism. We observe that the seed and finned catalysts all have similar initial conversion at fixed space velocity (Figure C10), despite differences in BAS concentration ranging from 510 to 750 mol/g; however, there are clear differences in catalyst deactivation where a temporal decrease in conversion (Figure C10) results in nearly linear rates of deactivation with finned catalysts coking less rapidly than the parent seed (i.e., deactivation rates of 0.5 and 1.5 h⁻¹, respectively). The ability of fins to improve catalyst lifetime is consistent with trends observed in methanol to hydrocarbon reaction for ZSM-5 and ZSM-11 catalysts(243), where we have shown that fins reduce the internal diffusion path length and increase the rate of molecule sorption into pores. These collective effects reduce mass transport limitations in finned catalysts with concomitant reduction in the rate of external coke accumulation.

We also observe that finned ferrierite zeolites increase isobutene selectivity from 75% for FS to 81% for FSF2 (Figure 4.4c). This is qualitatively consistent with previous studies showing that decreased size of ferrierite catalysts results in improved selectivity(233, 236). While it has been reported that the bimolecular mechanism is unselective for isobutene(253), the exact reason for increased selectivity in finned and nano-sized ferrierite zeolites is unresolved. We posit that one contributing factor may

be the reduced probability of secondary reactions (e.g., cracking or polymerization) as a result of the shortened diffusion path length in finned regions of the catalyst.

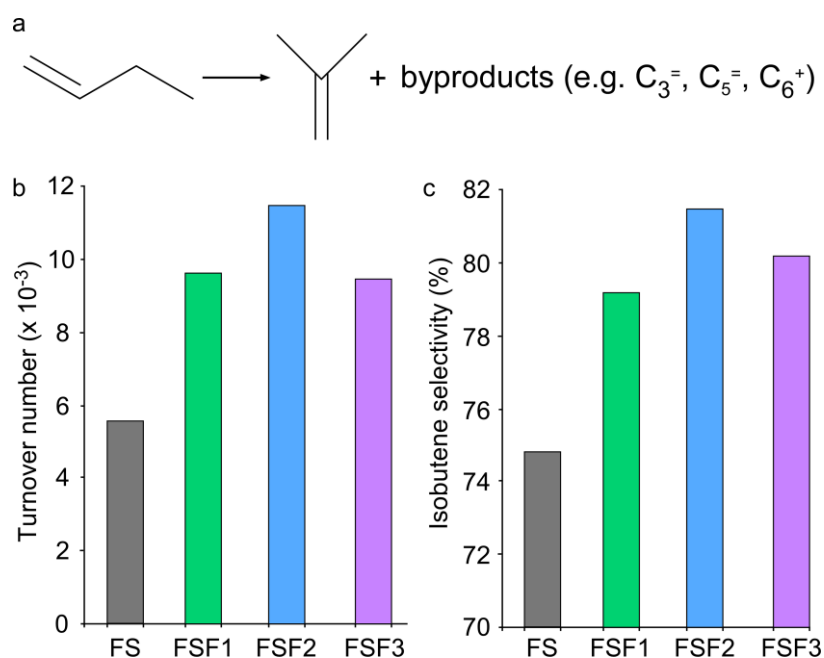


Figure 4.4. (a) Reaction of 1-butene to isobutene and byproducts (propene, pentene, etc.). (b) Comparison of turnover number (units of mol_C/mol_{H^+}) for the seed (FS, gray) and finned (FSF1, FSF2, and FSF3) catalysts in the isomerization reaction at subcomplete conversion of 1-butene ($\leq 60\%$). Reactions were performed at $400\text{ }^\circ\text{C}$ with $WHSV = 12\text{ h}^{-1}$ (evaluated between 45 – 55% conversion, Figure C10). (c) Corresponding isobutene selectivity for each catalyst (evaluated at 50% 1-butene conversion). The complete product selectivity distribution is provided in Figure C11.

As an example of introducing fins to an existing zeolite to improve catalyst performance, we conducted a similar experiment using commercial ferrierite (Zeolyst CP914C) as a parent seed to generate a finned analogue. We refer to these samples as FC and FCF, respectively. The physicochemical properties of these H-form catalysts (Table C1) the same as those of the seed and finned samples prepared in house. In Figure 4.5a, we report the decrease in conversion with time on stream for both samples wherein the x-axis is converted to cumulative turnovers as a fairer way of comparing catalyst deactivation. Interestingly, we observe a more pronounced increase in catalyst stability for the commercial sample relative to in house ferrierite catalysts, with FC and

FCF exhibiting deactivation rates of 1.4 and 0.3 h⁻¹, respectively. Analysis of TON (Figure 4.5b) reveals a significant three-fold increase for the finned sample (FCF) relative to its parent seed (FC). In addition, there was a more pronounced impact of fins on isobutene selectivity (Figure 4.5c) where the differences between FC and FCF increased with time on stream (i.e., with decreasing 1-butene conversion). Notably, isobutene selectivity increased from 67% (FC) to 81% (FCF) at 50% conversion. When compared to the difference between FS and FSF2 at similar conversion (Figure 4.4c), the net increase of 14% was more pronounced for the commercial sample. This may be attributed to the presence of rough features (i.e., small fin-like protrusions) on the surfaces of FS seeds that go undetected by electron microscopy but are seemingly evident in titration experiments (*vide infra*). This is also consistent with FS having a nearly two-fold higher external surface area than FC, despite both samples having on average similar crystal size. It is also possible that the commercial sample contains defects that are removed during secondary growth of fins, which contributes to the net improvement in catalyst lifetime and selectivity. Overall, comparison of both in house and commercial samples highlight the degree to which the performance of ferrierite catalysts can be enhanced by the introduction of fins.

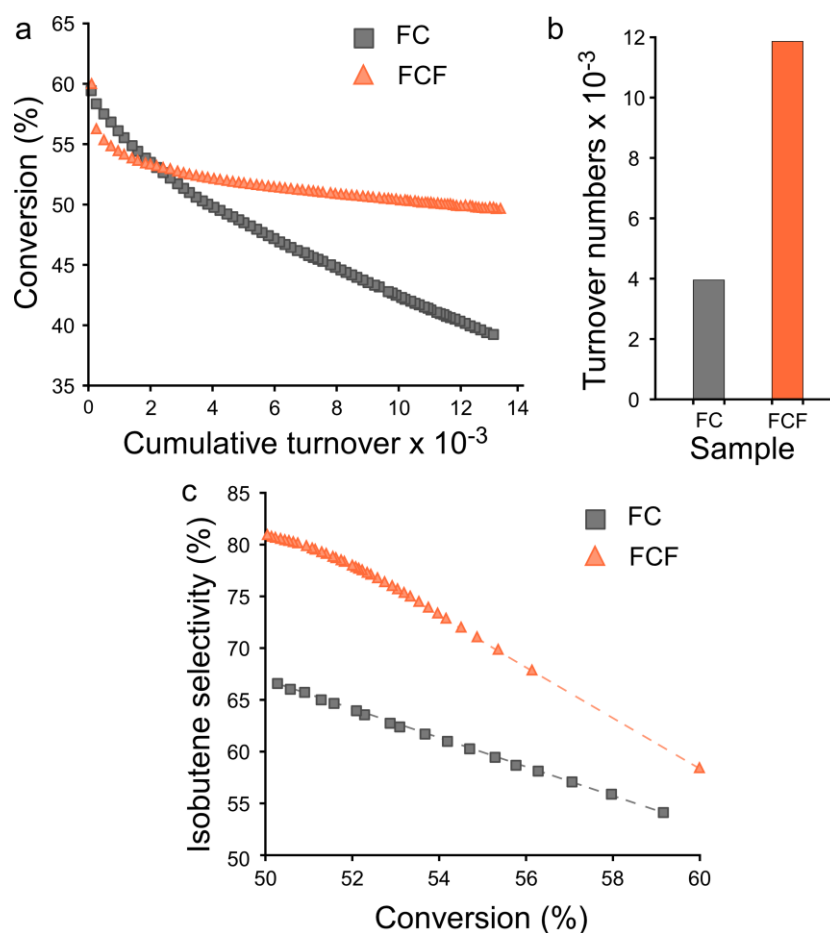


Figure 4.5. (a) Subcomplete conversion of 1-butene as a function of cumulative turnovers for commercial ferrierite FC (Zeolyst CP914C) and its finned analogue (FCF). (b) Comparison of turnover numbers (mol_C/mol_{H^+}) for seed (FC, gray) and finned (FCF, orange) catalysts evaluated at 45 – 55% conversion. (c) Isobutene selectivity as a function of 1-butene conversion.

To characterize the diffusion properties of finned ferrierite, titration experiments were conducted using time-resolved FTIR spectroscopy to quantify the disappearance of Brønsted acid sites (3605 cm^{-1}) and the concomitant uptake of amines (1555 cm^{-1}). Our previous study showed that 2,4,6-trimethylpyridine slowly accessed the internal pores and titrated Brønsted acid sites of three-dimensional **MFI** and **MEL** due to steric hindrance from methyl groups(243). As mentioned, Ferrierite is a two-dimensional catalyst comprised of two disparate smaller pores (8-MR and 10-MR). For this study, we used the titrant 2,3-dimethylpyridine (DMPyr), an organic base with smaller kinetic diameter, as the probe molecule due to the comparatively smaller pores of 10-

membered ring (MR) aperture in **FER** relative to **MFI**. DMPyr slow diffuses in **FER** 10-MR channels allowing for time-resolved comparison of the titration of acid sites within the fins and bulk catalyst. However, DMPyr is prohibitively large to access 8-MR channels, and titration of all BAS by DMPyr only occurs via diffusion along the 10-MR channels and adsorption at the intersection of the smaller 8-MR channels.

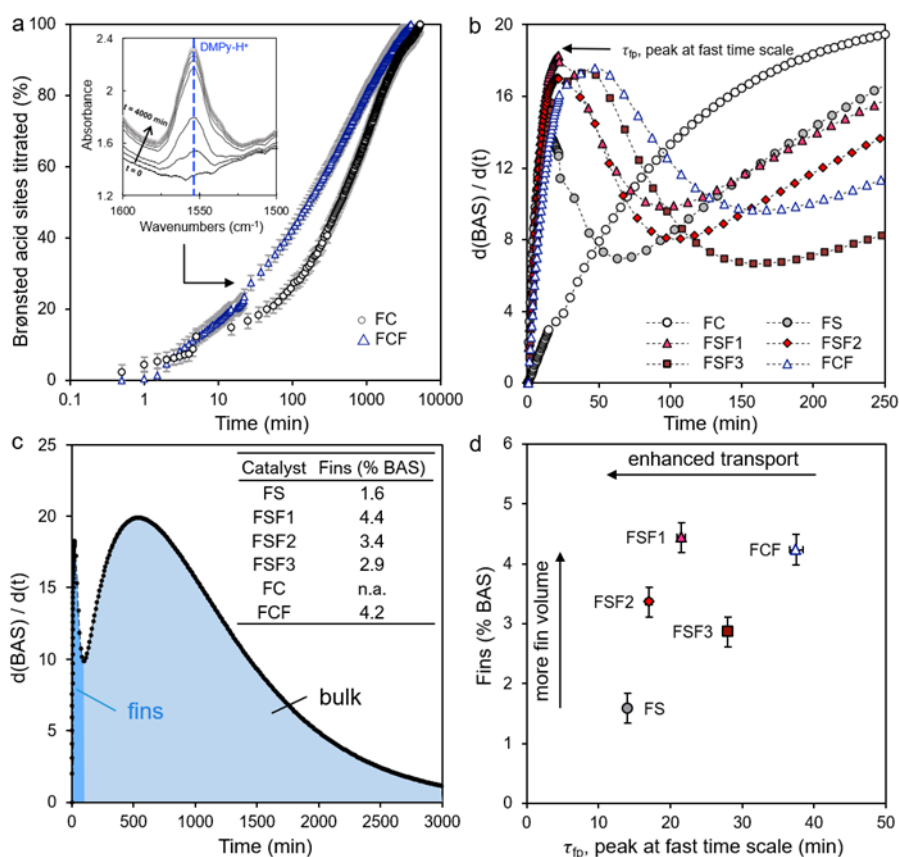


Figure 4.6. (a) Titration of BAS by 2,3-dimethylpyridine in commercial and finned **FER** (FC and FCF respectively) over time. (b) Derivative of BAS titration for all catalysts. (c) Derivative of BAS titration by 2,3-dimethylpyridine in FSF1 over time. Inset: Percentage of BAS titrated in fins over the bulk. (d) Percentage of fins BAS plotted as function of peak at fast time-scale, τ_{fp} .

The adsorption kinetics of DMPyr on Brønsted acid sites (BAS) of all **FER** catalysts were assessed via FTIR peak area at 1555 cm⁻¹ over 4,000 minutes (Figures 4.6a, C12, C15, and C16). As the DMPyr-H⁺ peak area increases with time, BAS in the catalyst were titrated over about 65 hours. To precisely determine the changing rates of amine

uptake, the derivative of BAS titration over time was plotted for both commercial **FER** and finned **FER** materials (Figures 4.6b, C11, C12, and C13). The area under the derivative peaks in Figure 6c represents the cumulative amount of BAS titrated at different times, with the first peak's maximum indicated by τ_{fp} , also referred to as the "peak at fast time-scale" (Figure C13). We observe that commercial ferrierite (FC) does not exhibit this initial peak τ_{fp} associated with fins, while the catalysts synthesized in-house (FS, FSF1, FSF2, FSF3, and FCF) all had τ_{fp} , indicating the presence of a significant portion of BAS that can be accessed more quickly than bulk acid sites. The initial fast BAS titration was attributed to the BAS in fins and external surface areas of the catalyst, while slower uptake was attributed to the BAS within the bulk catalyst (Figure 4.6c). The percentage of BAS in fins is plotted as a function of the peak at fast time-scale, τ_{fp} , for all catalysts (Figure 4.6d). Finned ferrierite materials, specifically FSF1 and FSF2, have higher percentages of BAS in fins and relatively lower τ_{fp} compared to seed and commercial ferrierite (FS, FC, FCF). This result is in agreement with the catalytic performances of **FER**, indicating that the better performing catalysts have enhanced transport properties and higher BAS volume in the fins.

4.4 Summary

In summary, we have developed a facile and highly versatile method for improving mass transport properties of zeolites with 2D pore networks. Most zeolites with 2D pores crystallize as platelets where internal diffusion is markedly more restricted than 3D counterparts. This places greater emphasis on the ability to synthesize nanosized zeolites and/or control anisotropic crystal growth to achieve morphologies that increase access to pore openings and reduce the internal diffusion pathlength. These outcomes are difficult to achieve by the manipulation of common synthesis parameters. The few

cases where nanosized ferrierite crystals are reported in literature rely on the use of unconventional organic structure-directing agents. Here, we demonstrate that secondary growth using traditional synthesis conditions can produce fins of tunable size, thereby endowing conventional ferrierite materials with enhanced properties that align with those of much smaller crystal size. This was confirmed by time-resolved titrations showing an initial uptake of the titrant is more rapid in fins; therefore, the introduction of fins transforms seeds into pseudo nanocrystals with enhanced mass transport and improved catalytic performance.

In this study, we selected 1-butene isomerization to assess the impact of fins on both catalyst lifetime and selectivity. Our findings reveal that fins dramatically extend the lifetime of ferrierite catalysts and also improve their efficiency (i.e., increase total turnovers) relative to their conventional counterparts. This is most evident for commercial ferrierite where finned analogues exhibit a four-fold decrease in the deactivation rate and a three-fold increase in TON. Moreover, finned commercial ferrierite has much higher isobutene selectivity, thus illustrating a key advantage of this approach: the ability to take a zeolite off the shelf and perform a facile post-synthesis modification to improve its properties. While this study focuses on a single reaction, we envision that finned zeolites can be used more generally to improve zeolite performance for a range of commercially-relevant reactions where mass transport limitations impose restrictions on current catalysts.

Chapter 5

Summary and Future Outlook

5.1 Current Research Summary

In this dissertation, we have studied how the presence of polymer additives with predominantly quaternary amine functionality impacted the nucleation of zeolite crystals. We selected a commercial-relevant zeolite, SSZ-13 (**CHA**), and showed that polyamines can be used as effective accelerants to regulate the evolution and colloidal stability of intermediate precursors via a nonclassical crystallization pathway. Among the additives tested, polydiallyldimethylammonium (PDDA) exhibited the most pronounced impact on the SSZ-13 crystallization, resulting in a 4-fold reduction in the synthesis time at intermediate polymer concentration. Our findings demonstrated that PDDA induced bridging flocculation of precursors and promoted the precipitation of soluble silicates, evidenced by a combination of electron microscopy and light scattering techniques. Based on these experiment observations, we proposed a generalized explanation based on the putative arrangement of amorphous precursors into clusters prior to the SSZ-13 nucleation in the presence of PDDA. Proximity between the precursor particles within these clusters leads to high surface area and solution within confined interstitial regions, which can facilitate mass transfer and exchange of (alumino)silicate species. This work sheds light on the role of polymer additives in SSZ-13 crystallization and offers a facile solution to improve the overall efficiency of zeolite synthesis.

Inspired by previous studies revealing 3-dimensional island growth in silicalite-1 (**MFI**), we invented a novel class of hierarchical catalysts referred to as “finned”

zeolites. In Chapter 3, we demonstrated that three-dimensional finned ZSM-5 (**MFI**) and ZSM-11 (**MEL**) zeolites can be epitaxially grown on the surface of seed crystals via the judicious selection of synthesis gel composition and conditions. Using high-resolution electron tomography in collaboration with Dr. Yang and Prof. Zou from Stockholm University, we confirmed the absence of intraparticle mesoporosity and visualized the size and shape of the small protrusions after secondary growth. Finned zeolite catalysts with enhanced external surface area exhibited outstanding mass transfer properties and catalyst lifetime (i.e., 3-fold reduction in the rate of deactivation) in the methanol-to-hydrocarbon (MTH) reaction. Using *operando* UV-Vis diffuse reflectance spectroscopy in collaboration with Dr. Fu and Prof. Weckhuysen from Utrecht University, we were able to attribute the slower deactivation rate of finned catalysts to the suppressed formation of external coke. Quantitative evaluation of diffusion properties was accomplished by a combination of kinetic Monte Carlo simulations (in collaboration with Prof. Palmer at the University of Houston) and time resolved FTIR spectroscopy (in collaboration with Prof. Dauenhauer at the University of Minnesota and Prof. Tsapatsis at Johns Hopkins University). Finned **MFI** material displayed more than a 2-fold reduction in the simulated mean diffusion path length of benzene diffusion, while an initial fast uptake of titrant, 2,4,6-trimethylpyridine (TMPyr), confirmed the superior mass transport properties of finned protrusions. To prove of concept, a similar synthetic approach was applied to a commercial ZSM-5 catalyst wherein we showed that finned analogue enhanced the catalyst lifetime, consistent with samples prepared in house.

The approach of epitaxially growing fins on zeolite catalysts has been proven to dramatically reduce diffusion limitations in zeolites. This facile method has the promise

of becoming a generalized platform for the rational design of zeolites, especially for frameworks with low-dimensional pores that exhibit more severe mass transport limitations. In Chapter 4, we extended the concept of finned zeolites to the synthesis of ferrierite (**FER**), which is a widely-used commercial zeolite with two-dimensional pores. We posited that ultrasmall fins (<50 nm) on ferrierite zeolite could markedly boost catalyst turnovers and product selectivity. We showed that fin sizes of ferrierite crystals could be tuned when varying the synthesis conditions (i.e., temperature). Transmission electron tomography was used to confirm the identical crystallographic registry of fins and seeds (in collaboration with Dr. Yang and Prof. Zou at Stockholm University). Similar to the titration experiments used for three-dimensional zeolites in Chapter 3, a smaller titrant, 2,3-dimethylpyridine (DMPyr), was used to identify the peak at fast time-scale (τ_{fp}) in collaboration with Prof. Dauenhauer (University of Minnesota) and Prof. Tsapatsis (Johns Hopkins University). These *in situ* titration experiments verified the substantial improvement in mass transfer properties for both synthetic and commercial finned ferrierite. Indeed, fins enhanced catalyst lifetime and isobutene selectivity in the 1-butene isomerization reaction compared to conventional analogues (in collaboration with Prof. Li at the Dalian Institute of Chemistry Physics).

5.2 Future Outlook

5.2.1 Hierarchical ZSM-5 Catalyst Comparison

To minimize mass transport limitations of nanoporous materials, a common objective in zeolite synthesis is the design of materials with smaller crystal dimensions and larger external surface area. To date, five different types of nanosized or hierarchical zeolite materials have been extensively studied in the literature, which can

be grouped as nanoparticles, self-pillared, finned, two-dimensional, and mesoporous materials. Although many researchers have demonstrated the benefits of these advanced materials (i.e., superior performance in diffusion-limited reactions), in many cases, it is still an obstacle to directly evaluate the catalytic performance among these materials due to the ignored physicochemical properties and inconsistent test conditions. As mentioned previously, Ryoo and coworkers invented the synthesis of two-dimensional MFI nanosheets (2 nm thickness) and reported that multilamellar ZSM-5 catalysts exhibit excellent lifetime due to the suppression of coke formation in the MTH reaction(154). Self-pillared pentasil (SPP) catalysts with house-of-cards arrangements, discovered by Tsapatsis and coworkers, demonstrated higher apparent reaction rates in mesitylene alkylation by benzyl alcohol(179). In addition, nanosized ZSM-5 materials (<50 nm) have been prepared by Tsapatsis and coworkers using mesoporous carbon as a template. These promising catalysts are referred to as three-dimensional ordered mesoporous (3Dom). The objective of an ongoing project in the Rimer group is to conduct an impartial evaluation of these nanosized or hierarchical ZSM-5 catalysts in both gas and liquid phase reactions. The synthesis conditions of all these nanosized or hierarchical materials are summarized in Table 5.1.

Table 5.1. Physicochemical properties of nanosized and hierarchical ZSM-5 zeolites.

Sample ^a	Molar Composition of Growth Mixture						T (°C)	Time (day)
	Al ₂ O ₃	SiO ₂	Na ₂ O	H ₂ O	H ₂ SO ₄	OSDA ^b		
NS	1	100	30	4000	18	10	150	7
SPP	1	100	1.25	1000	4.5	30	120	10
Seed	1.25	100	4	2500	n.a.	15	170	2
Finned	1.25	100	1.25	3800	n.a.	32	110	1

^a NS = ZSM-5 nanosheet reproduced from literature,(178) SPP = self-pillared pentasil material provided from the Tsapatsis group; ^b C₂₂₋₆₋₆Br₂, tetrabutylphosphonium hydroxide (TBPOH), tetrapropylammonium hydroxide (TPAOH), and TPAOH were used as OSDAs for the syntheses of NS, SPP, seed and finned samples, respectively.

We followed the protocol in literature to reproduce ZSM-5 nanosheet (NS) synthesis. As shown in Figure 5.1a, a multilamellar NS material with similar morphology was successfully synthesized. Using a conventional pillaring method(178), we synthesized pillared multilamellar ZSM-5 nanosheet (NS-P) catalysts with higher external surface area (Table 5.1 and Figure 5.1a), consistent with reported properties of NS-P compared to NS(178). However, we observed appreciable reduction of micropore volume after ammonium ion exchange and calcination to produce H-form catalysts (Table 5.2).

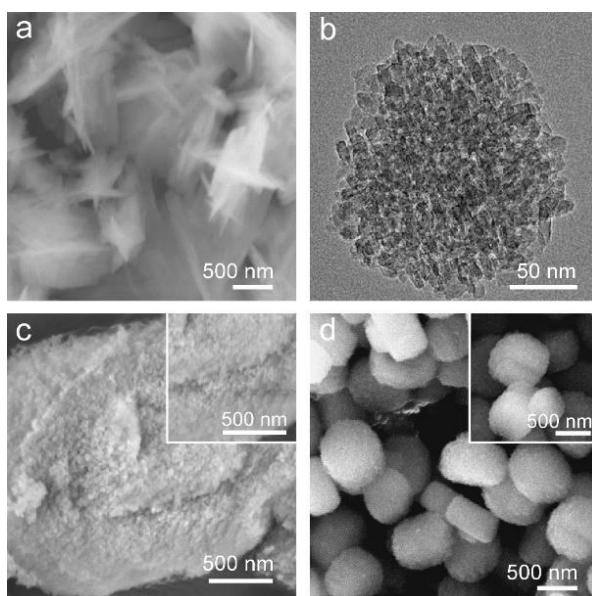


Figure 5.1. Electron micrographs of (a) NS, (b) SPP, (c) 3Dom, and (d) Finned ZSM-5 samples.

To overcome this, we applied an annealing approach, which has been shown to improve the crystallinity and/or deplete of extra-framework Al species in finned and few-unit-cell crystalline domain pentasil (FDP) materials (Figure D1 in Appendix D)(254). As shown in Table 5.2, the micropore volume of the H-form catalyst was restored to its expected value after annealing, although there was slightly dealumination during the annealing process. The SPP and 3Dom materials were directly obtained from

the Tsapatsis and Fan groups, respectively. Scanning electron microscopy (SEM) in Figure 5.1b and c displayed the similar morphology as reported(171, 178). The finned ZSM-5 material was also obtained by the judicious selection of synthesis gel composition, as shown in Figure 5.1d. In order to study the effect of annealing on zeolite properties and catalytic performance, the SPP and finned ZSM-5 materials were subjected to an annealing step at 170 °C for three days. Here we also included one commercial ZSM-5 catalyst (Zeolyst, CBV8014) as a reference to compare against nanosized and hierarchical ZSM-5 samples.

Table 5.2. Physicochemical properties of nanosized and hierarchical ZSM-5 zeolite samples.

Sample	BET S_A (m^2/g) ^a	S_{ext} (m^2/g) ^a	V_{micro} (cm^3/g) ^a	Si/Al (bulk) ^b
NS	455	201	0.11	43
NS-P	501	357	0.06	n.a.
NS-P-A	456	183	0.11	75
SPP	737	362	0.13	40.3
SPP-A	494	205	0.12	40.2
Seed	385	97	0.11	55
Finned	445	180	0.11	63

^a N_2 adsorption/desorption measurements of BET total surface area (S_A), external surface area (S_{ext}), and micropore volume (V_{micro}); ^b Elemental analysis of bulk Si/Al measured by ICP-OES.

The MTH (gas phase) and Friedel-Crafts alkylation reaction of mesitylene with benzyl alcohol (liquid phase) were selected as benchmark reactions to elucidate the mass transfer properties of as-made catalysts. As shown in Figure 5.2a, preliminary catalytic results showed the non-annealed SPP catalyst displayed lower activity compared with the Zeolyst sample with similar Si/Al ratio at the same reaction condition (i.e., $T = 350$ °C with a weight-hourly space velocity of $WHSV = 15$ h^{-1}).

These results suggest the non-annealed SPP sample may contain a fraction of defective acid sites. Interestingly, the SPP material (SPP-A) showed even higher activity and better stability compared with an annealed Zeolyst sample. Quantitative assessment of the acid site density and acid strength may be used to interpret the improvement in catalytic performance. The annealed ZSM-5 nanosheet (NS-P-A), as shown in Figure 5.2b, exhibited enhanced activity and stability under similar reaction conditions reported in the literature (i.e., $T = 400\text{ }^{\circ}\text{C}$ with $\text{WHSV} = 11\text{ h}^{-1}$). However, when the reaction temperature was lowered to $350\text{ }^{\circ}\text{C}$, which is more commonly used in MTH reactions, we observed low initial activity (ca. 30% methanol conversion) for the NS-P-A material (Figure 5.2a), possibly due to the dealumination during annealing and/or the presence of extra-framework Al species in the sample. Careful characterization is needed in the future to elucidate the structure-performance relationships of these hierarchical catalysts. Furthermore, systematic analysis of the annealing conditions (i.e., time and temperature) deserves further investigation. Preliminary results demonstrated that prolonged annealing time may be detrimental for low-Al containing ZSM-5 (i.e., leading to the ripening and removal of finned features). It is evident that careful post-synthetic procedures, such as annealing, can be an effective and versatile approach to improve the activity and stability of hierarchical zeolite catalysts. In the future, researchers should pay closer attention to post-synthesis modification methods to improve next-generation zeolite catalysts.

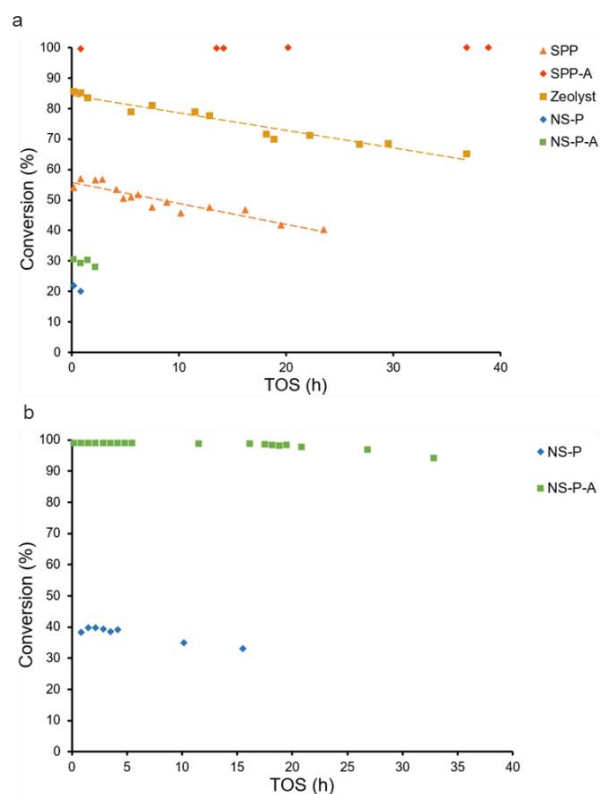


Figure 5.2. (a) Plots of methanol conversion over SPP, SPP-A, Zeolyst, NS-P and NS-P-A catalysts during the MTH reaction as a function of time on stream (TOS). Reaction conditions are 350 °C and $\text{WHSV} = 15 \text{ h}^{-1}$. (b) Plots of methanol conversion over NS-P and NS-P-A catalysts during MTH as a function of TOS. Reaction conditions are 400 °C and $\text{WHSV} = 11 \text{ h}^{-1}$.

5.2.2 Finned Zeolite with One-dimensional Pores

As discussed in Chapters 3 and 4, we successfully synthesized three- and two-dimensional finned zeolites: ZSM-5 (**MFI**), ZSM-11 (**MEL**) and ferrierite (**FER**). All these materials exhibited dramatically improved mass transport properties compared to their non-finned counterparts. Observation of enhanced catalytic performance (i.e., lifetime and selectivity) validated that secondary epitaxial growth of protrusions can transform seeds into pseudo nanoparticles with improved diffusion properties; thus, this approach serves as a generalized platform for the rational design of zeolites across a broad range of framework types for diverse applications in the (petro)chemical industry. One fascinating study would be to generate finned zeolites for zeolites with

one-dimensional pores. Methods to optimize one-dimensional materials include post-synthesis modification to introduce mesopores whereas relatively few cases have been reported where the judicious selection of synthesis parameters leads to nanosized crystals. However, one-dimensional zeolites are highly susceptible to severe accumulation of coke during reactions, leading to fast deactivation. One-dimensional zeolite structures such as ZSM-23 (**MTT**) and ZSM-22 (**TON**) could be decorated with finned features. Beato and coworkers reported a novel method to generate nanosized ZSM-23 crystals with sizes around 100 nm(255). With careful selection of secondary growth conditions (i.e., gel composition, seeding amount and synthesis temperature), it is likely that similar approaches in this dissertation can be used to generate finned **MTT** catalysts. More interestingly, a systemically catalytic study could be performed using the MTH reaction to assess finned zeolites with one-, two-, and three-dimensional pores (e.g., selecting only medium-pore catalysts for equivalent comparisons). For example, the one-dimensional **TON** zeolite does contain channel intersections large enough to render the aromatic cycle active. A finned **TON** catalyst may facilitate the diffusion of intermediate reactive species, which may reduce external coke and improve the olefin selectivity compared with other finned materials.

Secondary growth can also be generally applied in syntheses of broader zeolitic materials. For example, aluminophosphate (AIPO) or silicoaluminophosphates (SAPO) could be used as seeds for growth of fins. It has been shown that nanosized SAPO-34 material prolongs the catalyst lifetime in MTO catalysis(256); however, few syntheses of nanosized (<100 nm) SAPO-34 crystals have been reported. Generating even smaller SAPO-34 dimensions (<50 nm) could be rationally designed via secondary growth on a conventional seed. The kinetics of nucleation and growth for zeotype materials may

be different from those of zeolites based on differences in properties, such as acidity and pH. Judicious selection of synthesis parameters would ultimately lead to the next-generation of SAPO-34 materials with the promise of commercialization in MTO catalysis.

References

1. G. A. Ozin, A. Kuperman, A. Stein, Advanced Zeolite, Materials Science. *Angew. Chemie Int. Ed. English*. **28**, 359–376 (1989).
2. B. M. Lok, C. A. Messina, R. L. Patton, R. T. Gajek, T. R. Cannan, E. M. Flanigen, Silicoaluminophosphate molecular sieves: another new class of microporous crystalline inorganic solids. *J. Am. Chem. Soc.* **106**, 6092–6093 (1984).
3. R. M. Barrer, Zeolites and their synthesis. *Zeolites*. **1**, 130–140 (1981).
4. E. M. Flanigen, R. L. Patton, S. T. Wilson, in *Innovation in Zeolite Materials Science*, P. J. Grobet, W. J. Mortier, E. F. Vansant, G. B. T.-S. in S. S. and C. Schulz-Ekloff, Eds. (Elsevier, 1988; <https://www.sciencedirect.com/science/article/pii/S0167299109605784>), vol. 37, pp. 13–27.
5. J. Kugbe, N. Matsue, T. Henmi, Synthesis of Linde type A zeolite–goethite nanocomposite as an adsorbent for cationic and anionic pollutants. *J. Hazard. Mater.* **164**, 929–935 (2009).
6. International Zeolite Association (IZA) Structure Database. IZA <http://www.iza-structure.org/databases/> (2017).
7. E. M. Flanigen, in *Introduction to Zeolite Science and Practice*, H. van Bekkum, E. M. Flanigen, J. C. B. T.-S. in S. S. and C. Jansen, Eds. (Elsevier, 1991; <https://www.sciencedirect.com/science/article/pii/S0167299108635995>), vol. 58, pp. 13–34.
8. T. F. Degnan, The implications of the fundamentals of shape selectivity for the development of catalysts for the petroleum and petrochemical industries. *J. Catal.* **216**, 32–46 (2003).
9. A. Corma, M. J. Díaz-Cabañas, J. L. Jordá, C. Martínez, M. Moliner, High-throughput synthesis and catalytic properties of a molecular sieve with 18- and 10-member rings. *Nature*. **443**, 842–845 (2006).
10. J. Sun, C. Bonneau, Á. Cantín, A. Corma, M. J. Díaz-Cabãas, M. Moliner, D. Zhang, M. Li, X. Zou, The ITQ-37 mesoporous chiral zeolite. *Nature*. **458**, 1154–1157 (2009).
11. J. Jiang, J. Yu, A. Corma, Extra-Large-Pore Zeolites: Bridging the Gap between Micro and Mesoporous Structures. *Angew. Chemie Int. Ed.* **49**, 3120–3145 (2010).
12. J. Jiang, J. L. Jorda, J. Yu, L. A. Baumes, E. Mugnaioli, M. J. Diaz-Cabanas, U. Kolb, A. Corma, *Science* in press, doi:10.1126/science.1208652.
13. J. Li, A. Corma, J. Yu, Synthesis of new zeolite structures. *Chem. Soc. Rev.* **44**, 7112–7127 (2015).

14. A. Burton, Recent trends in the synthesis of high-silica zeolites. *Catal. Rev.* **60**, 132–175 (2018).
15. P. B. Weisz, V. J. Frilette, Intracrystalline and molecular-shape-selective catalysis by zeolite salts. *J. Phys. Chem.* **64**, 382 (1960).
16. P. B. Weisz, Molecular shape selective catalysis. *Pure Appl. Chem.* **52**, 2091–2103 (1980).
17. C. S. Cundy, P. A. Cox, The Hydrothermal Synthesis of Zeolites: History and Development from the Earliest Days to the Present Time (2003), doi:10.1021/cr020060i.
18. C. Martínez, A. Corma, Inorganic molecular sieves: Preparation, modification and industrial application in catalytic processes. *Coord. Chem. Rev.* **255**, 1558–1580 (2011).
19. T. P. Lee, B. Saad, E. P. Ng, B. Salleh, Zeolite Linde Type L as micro-solid phase extraction sorbent for the high performance liquid chromatography determination of ochratoxin A in coffee and cereal. *J. Chromatogr. A.* **1237**, 46–54 (2012).
20. K. A. Cychosz, R. Guillet-Nicolas, J. García-Martínez, M. Thommes, Recent advances in the textural characterization of hierarchically structured nanoporous materials. *Chem. Soc. Rev.* **46**, 389–414 (2017).
21. N. Rangnekar, N. Mittal, B. Elyassi, J. Caro, M. Tsapatsis, Zeolite membranes – a review and comparison with MOFs. *Chem. Soc. Rev.* **44**, 7128–7154 (2015).
22. K. Varoon, X. Zhang, B. Elyassi, D. D. Brewer, M. Gettel, S. Kumar, J. A. Lee, S. Maheshwari, A. Mittal, C.-Y. Sung, M. Cococcioni, L. F. Francis, A. V McCormick, K. A. Mkhoyan, M. Tsapatsis, *Science* in press, doi:10.1126/science.1208891.
23. G. Calzaferri, S. Huber, H. Maas, C. Minkowski, Host–guest antenna materials. *Angew. Chemie Int. Ed.* **42**, 3732–3758 (2003).
24. G. Calzaferri, R. Méallet-Renault, D. Brühwiler, R. Pansu, I. Dolamic, T. Dienel, P. Adler, H. Li, A. Kunzmann, Designing dye–nanochannel antenna hybrid materials for light harvesting, transport and trapping. *ChemPhysChem.* **12**, 580–594 (2011).
25. R. Köppe, O. Bossart, G. Calzaferri, N. S. Sariciftci, Advanced photon-harvesting concepts for low-energy gap organic solar cells. *Sol. energy Mater. Sol. cells.* **91**, 986–995 (2007).
26. Z. Li, J. Hüve, C. Krampe, G. Luppi, M. Tsotsalas, J. Klingauf, L. De Cola, K. Riehemann, Internalization Pathways of Anisotropic Disc-Shaped Zeolite L Nanocrystals with Different Surface Properties in HeLa Cancer Cells. *Small.* **9**, 1809–1820 (2013).
27. M. D. Oleksiak, J. D. Rimer, Synthesis of zeolites in the absence of organic structure-directing

- agents: factors governing crystal selection and polymorphism. *Rev. Chem. Eng.* **30**, 1–49 (2014).
28. R. I. Masel, *Chemical kinetics and catalysis* (Wiley-Interscience New York, 2001), vol. 10.
29. W. Vermeiren, J.-P. Gilson, Impact of zeolites on the petroleum and petrochemical industry. *Top. Catal.* **52**, 1131–1161 (2009).
30. E. T. C. Vogt, B. M. Weckhuysen, Fluid catalytic cracking: recent developments on the grand old lady of zeolite catalysis. *Chem. Soc. Rev.* **44**, 7342–7370 (2015).
31. P. B. Venuto, E. T. Habib Jr, Fluid catalytic cracking with zeolite catalysts (1979).
32. A. Corma, in *Studies in surface science and catalysis* (Elsevier, 1989), vol. 49, pp. 49–67.
33. H. Weyda, E. Köhler, Modern refining concepts—an update on naphtha-isomerization to modern gasoline manufacture. *Catal. Today.* **81**, 51–55 (2003).
34. G. Valavarasu, B. Sairam, Light naphtha isomerization process: a review. *Pet. Sci. Technol.* **31**, 580–595 (2013).
35. I. E. Maxwell, Zeolite catalysis in hydroprocessing technology. *Catal. Today.* **1**, 385–413 (1987).
36. T. F. Degnan, Applications of zeolites in petroleum refining. *Top. Catal.* **13**, 349–356 (2000).
37. W. Yang, Z. Wang, H. Sun, B. Zhang, Advances in development and industrial applications of ethylbenzene processes. *Chinese J. Catal.* **37**, 16–26 (2016).
38. H. G. Karge, J. Ladebeck, Z. Sarbak, K. Hatada, Conversion of alkylbenzenes over zeolite catalysts. I. Dealkylation and disproportionation of ethylbenzene over mordenites. *Zeolites.* **2**, 94–102 (1982).
39. H.-K. Min, S. H. Cha, S. B. Hong, Mechanistic insights into the zeolite-catalyzed isomerization and disproportionation of m-xylene. *ACS Catal.* **2**, 971–981 (2012).
40. D. P. Upare, S. Park, M. S. Kim, Y.-P. Jeon, J. Kim, D. Lee, J. Lee, H. Chang, S. Choi, W. Choi, Selective hydrocracking of pyrolysis fuel oil into benzene, toluene and xylene over CoMo/beta zeolite catalyst. *J. Ind. Eng. Chem.* **46**, 356–363 (2017).
41. R. J. Kalbasi, O. Mazaheri, Synthesis and characterization of hierarchical ZSM-5 zeolite containing Ni nanoparticles for one-pot reductive amination of aldehydes with nitroarenes. *Catal. Commun.* **69**, 86–91 (2015).
42. H. A. Smail, M. Rehan, K. M. Shareef, Z. Ramli, A.-S. Nizami, J. Gardy, Synthesis of uniform mesoporous zeolite ZSM-5 catalyst for friedel-crafts acylation. *ChemEngineering.* **3**, 35 (2019).

43. G. W. Huber, A. Corma, Synergies between bio-and oil refineries for the production of fuels from biomass. *Angew. Chemie Int. Ed.* **46**, 7184–7201 (2007).
44. T. Ennaert, J. Van Aelst, J. Dijkmans, R. De Clercq, W. Schutyser, M. Dusselier, D. Verboekend, B. F. Sels, Potential and challenges of zeolite chemistry in the catalytic conversion of biomass. *Chem. Soc. Rev.* **45**, 584–611 (2016).
45. D. P. Serrano, J. A. Melero, G. Morales, J. Iglesias, P. Pizarro, Progress in the design of zeolite catalysts for biomass conversion into biofuels and bio-based chemicals. *Catal. Rev.* **60**, 1–70 (2018).
46. M. Moliner, Y. Román-Leshkov, M. E. Davis, Tin-containing zeolites are highly active catalysts for the isomerization of glucose in water. *Proc. Natl. Acad. Sci.* **107**, 6164–6168 (2010).
47. S. Mohan, P. Dinesha, S. Kumar, NO_x reduction behaviour in copper zeolite catalysts for ammonia SCR systems: A review. *Chem. Eng. J.* **384**, 123253 (2020).
48. H. Wang, R. Xu, Y. Jin, R. Zhang, Zeolite structure effects on Cu active center, SCR performance and stability of Cu-zeolite catalysts. *Catal. Today.* **327**, 295–307 (2019).
49. J. Zhu, Z. Liu, L. Xu, T. Ohnishi, Y. Yanaba, M. Ogura, T. Wakihara, T. Okubo, Understanding the high hydrothermal stability and NH₃-SCR activity of the fast-synthesized ERI zeolite. *J. Catal.* **391**, 346–356 (2020).
50. A. D. Chowdhury, A. Lucini Paioni, G. T. Whiting, D. Fu, M. Baldus, B. M. Weckhuysen, Unraveling the Homologation Reaction Sequence of the Zeolite-Catalyzed Ethanol-to-Hydrocarbons Process. *Angew. Chemie.* **131**, 3948–3952 (2019).
51. B. M. Weckhuysen, J. Yu, Recent advances in zeolite chemistry and catalysis. *Chem. Soc. Rev.* **44**, 7022–7024 (2015).
52. S. Teketel, M. W. Erichsen, F. L. Bleken, S. Svelle, K. P. Lillerud, U. Olsbye, Shape selectivity in zeolite catalysis. The Methanol to Hydrocarbons (MTH) reaction. *Catalysis.* **26**, 179–217 (2014).
53. S. Teketel, W. Skistad, S. Benard, U. Olsbye, K. P. Lillerud, P. Beato, S. Svelle, Shape selectivity in the conversion of methanol to hydrocarbons: the catalytic performance of one-dimensional 10-ring zeolites: ZSM-22, ZSM-23, ZSM-48, and EU-1. *Acs Catal.* **2**, 26–37 (2012).
54. A. Hwang, T. T. Le, Z. Shi, H. Dai, J. D. Rimer, A. Bhan, Effects of diffusional constraints on lifetime and selectivity in methanol-to-olefins catalysis on HSAPO-34. *J. Catal.* **369**, 122–132 (2019).
55. A. Hwang, A. Bhan, Deactivation of zeolites and zeotypes in methanol-to-hydrocarbons catalysis: mechanisms and circumvention. *Acc. Chem. Res.* **52**, 2647–2656 (2019).

56. B. L. Foley, B. A. Johnson, A. Bhan, A Method for Assessing Catalyst Deactivation: A Case Study on Methanol-to-Hydrocarbons Conversion (2019).
57. S. Ilias, A. Bhan, Mechanism of the catalytic conversion of methanol to hydrocarbons. *ACS Catal.* **3**, 18–31 (2013).
58. S. S. Arora, Z. Shi, A. Bhan, Mechanistic Basis for Effects of High-Pressure H₂ Cofeeds on Methanol-to-Hydrocarbons Catalysis over Zeolites. *ACS Catal.* **9**, 6407–6414 (2019).
59. B. Liu, D. Slocombe, M. AlKinany, H. AlMegren, J. Wang, J. Arden, A. Vai, S. Gonzalez-Cortes, T. Xiao, V. Kuznetsov, Advances in the study of coke formation over zeolite catalysts in the methanol-to-hydrocarbon process. *Appl. Petrochemical Res.* **6**, 209–215 (2016).
60. D. Fu, A. Lucini Paioni, C. Lian, O. van der Heijden, M. Baldus, B. M. Weckhuysen, Elucidating Zeolite Channel Geometry–Reaction Intermediate Relationships for the Methanol-to-Hydrocarbon Process. *Angew. Chemie.* **132**, 20199–20205 (2020).
61. D. Rojo-Gama, S. Etemadi, E. Kirby, K. P. Lillerud, P. Beato, S. Svelle, U. Olsbye, Time- and space-resolved study of the methanol to hydrocarbons (MTH) reaction-influence of zeolite topology on axial deactivation patterns. *Faraday Discuss.* **197**, 421–446 (2017).
62. B. M. Weckhuysen, J. Yu, Recent advances in zeolite chemistry and catalysis. *Chem. Soc. Rev.* **44**, 7022–7024 (2015).
63. U. Olsbye, S. Svelle, M. Bjrgen, P. Beato, T. V. W. Janssens, F. Joensen, S. Bordiga, K. P. Lillerud, Conversion of methanol to hydrocarbons: How zeolite cavity and pore size controls product selectivity. *Angew. Chemie - Int. Ed.* (2012), , doi:10.1002/anie.201103657.
64. B. L. Foley, B. A. Johnson, A. Bhan, A Method for Assessing Catalyst Deactivation: A Case Study on Methanol-to-Hydrocarbons Conversion. *ACS Catal.* **9**, 7065–7072 (2019).
65. S. Teketel, W. Skistad, S. Benard, U. Olsbye, K. P. Lillerud, P. Beato, S. Svelle, Shape Selectivity in the Conversion of Methanol to Hydrocarbons: The Catalytic Performance of One-Dimensional 10-Ring Zeolites: ZSM-22, ZSM-23, ZSM-48, and EU-1. **2**, 26–37 (2012).
66. A. Hwang, A. Bhan, Deactivation of Zeolites and Zeotypes in Methanol-to-Hydrocarbons Catalysis: Mechanisms and Circumvention. *Acc. Chem. Res.* (2019), doi:10.1021/acs.accounts.9b00204.
67. A. Hwang, T. T. Le, Z. Shi, H. Dai, J. D. Rimer, A. Bhan, Effects of diffusional constraints on lifetime and selectivity in methanol-to-olefins catalysis on HSAPO-34. *J. Catal.* **369**, 122–132 (2019).
68. S. Mintova, J. P. Gilson, V. Valtchev, Advances in nanosized zeolites. *Nanoscale.* **5**, 6693–

6703 (2013).

69. C. S. Cundy, P. A. Cox, The hydrothermal synthesis of zeolites: Precursors, intermediates and reaction mechanism. *Microporous mesoporous Mater.* **82**, 1–78 (2005).
70. R. E. Morris, Ionothermal synthesis of zeolites and other porous materials. *Zeolites Catal. Synth. React. Appl.*, 87–105 (2010).
71. J. Zhu, Z. Liu, A. Endo, Y. Yanaba, T. Yoshikawa, T. Wakihara, T. Okubo, Ultrafast, OSDA-free synthesis of mordenite zeolite. *CrystEngComm.* **19**, 632–640 (2017).
72. L. Van Tendeloo, E. Gobechiya, E. Breynaert, J. A. Martens, C. E. A. Kirschhock, Alkaline cations directing the transformation of FAU zeolites into five different framework types. *Chem. Commun.* **49**, 11737–11739 (2013).
73. K. Iyoki, K. Itabashi, T. Okubo, Progress in seed-assisted synthesis of zeolites without using organic structure-directing agents. *Microporous mesoporous Mater.* **189**, 22–30 (2014).
74. D. I. Petkowicz, M. L. Mignoni, J. H. Z. dos Santos, Dry-gel process for zeolite synthesis: Some fundamental aspects. *Microporous Mesoporous Mater.* **279**, 92–98 (2019).
75. K. G. Strohmaier, Synthesis approaches. *Zeolites Catal. Synth. React. Appl.*, 57–86 (2010).
76. Y. Jin, X. Chen, Q. Sun, N. Sheng, Y. Liu, C. Bian, F. Chen, X. Meng, F.-S. Xiao, Solvent-Free Syntheses of Hierarchically Porous Aluminophosphate-Based Zeolites with AEL and AFI Structures. *Chem. – A Eur. J.* **20**, 17616–17623 (2014).
77. K. Iyoki, K. Itabashi, T. Okubo, Seed-Assisted, One-Pot Synthesis of Hollow Zeolite Beta without Using Organic Structure-Directing Agents. *Chem. Asian J.* **8**, 1419–1427 (2013).
78. M. H. Nada, S. C. Larsen, Insight into seed-assisted template free synthesis of ZSM-5 zeolites. *Microporous Mesoporous Mater.* **239**, 444–452 (2017).
79. V. Valtchev, L. Tosheva, Porous Nanosized Particles: Preparation, Properties, and Applications. *Chem. Rev.* **113**, 6734–6760 (2013).
80. Y. Li, W. Yang, Microwave synthesis of zeolite membranes: A review. *J. Memb. Sci.* **316**, 3–17 (2008).
81. Q. Wu, X. Hong, L. Zhu, X. Meng, S. Han, J. Zhang, X. Liu, C. Jin, F.-S. Xiao, Generalized ionothermal synthesis of silica-based zeolites. *Microporous Mesoporous Mater.* **286**, 163–168 (2019).
82. H. Chen, J. Wydra, X. Zhang, P.-S. Lee, Z. Wang, W. Fan, M. Tsapatsis, Hydrothermal synthesis of zeolites with three-dimensionally ordered mesoporous-imprinted structure. *J. Am. Chem.*

- Soc.* **133**, 12390–12393 (2011).
83. Y. Chai, W. Shang, W. Li, G. Wu, W. Dai, N. Guan, L. Li, Noble metal particles confined in zeolites: synthesis, characterization, and applications. *Adv. Sci.* **6**, 1900299 (2019).
84. W. Fan, M. A. Snyder, S. Kumar, P.-S. Lee, W. C. Yoo, A. V McCormick, R. L. Penn, A. Stein, M. Tsapatsis, Hierarchical nanofabrication of microporous crystals with ordered mesoporosity. *Nat. Mater.* **7**, 984–991 (2008).
85. D. Shi, L. Xu, P. Chen, T. Ma, C. Lin, X. Wang, D. Xu, J. Sun, Hydroxyl free radical route to the stable siliceous Ti-UTL with extra-large pores for oxidative desulfurization. *Chem. Commun.* **55**, 1390–1393 (2019).
86. G. Feng, P. Cheng, W. Yan, M. Boronat, X. Li, J.-H. Su, J. Wang, Y. Li, A. Corma, R. Xu, Accelerated crystallization of zeolites via hydroxyl free radicals. *Science* **351**, 1188–1191 (2016).
87. J. L. Jordá, F. Rey, G. Sastre, S. Valencia, M. Palomino, A. Corma, A. Segura, D. Errandonea, R. Lacomba, F. J. Manjón, Synthesis of a novel zeolite through a pressure-induced reconstructive phase transition process. *Angew. Chemie.* **125**, 10652–10656 (2013).
88. C. Tan, Z. Liu, Y. Yonezawa, S. Sukenaga, M. Ando, H. Shibata, Y. Sasaki, T. Okubo, T. Wakihara, Unique crystallization behavior in zeolite synthesis under external high pressures. *Chem. Commun.* **56**, 2811–2814 (2020).
89. H. Wang, L. Wang, F.-S. Xiao, Metal@Zeolite Hybrid Materials for Catalysis. *ACS Cent. Sci.* **6**, 1685–1697 (2020).
90. I. V Markov, Crystal growth for beginners: fundamentals of nucleation. *Growth Ep. Singapore World Sci.* (2003).
91. J. J. De Yoreo, P. U. P. A. Gilbert, N. A. J. M. Sommerdijk, R. L. Penn, S. Whitlam, D. Joester, H. Zhang, J. D. Rimer, A. Navrotsky, J. F. Banfield, A. F. Wallace, F. M. Michel, F. C. Meldrum, H. Cölfen, P. M. Dove, Crystallization by particle attachment in synthetic, biogenic, and geologic environments. *Science* **349** (2015), doi:10.1126/science.aaa6760.
92. M. K. Choudhary, M. Kumar, J. D. Rimer, Regulating Nonclassical Pathways of Silicalite-1 Crystallization through Controlled Evolution of Amorphous Precursors. *Angew. Chemie Int. Ed.* **58**, 15712–15716 (2019).
93. A. E. S. Van Driessche, L. G. Benning, J. D. Rodriguez-Blanco, M. Ossorio, P. Bots, J. M. García-Ruiz, *Science* in press, doi:10.1126/science.1215648.

94. S.-T. Yau, P. G. Vekilov, Direct Observation of Nucleus Structure and Nucleation Pathways in Apoferritin Crystallization. *J. Am. Chem. Soc.* **123**, 1080–1089 (2001).
95. M. Kumar, R. Li, J. D. Rimer, Assembly and Evolution of Amorphous Precursors in Zeolite L Crystallization. *Chem. Mater.* (2016), doi:10.1021/acs.chemmater.5b04569.
96. M. Kumar, H. Luo, Y. Román-Leshkov, J. D. Rimer, SSZ-13 crystallization by particle attachment and deterministic pathways to crystal size control. *J. Am. Chem. Soc.* (2015), doi:10.1021/jacs.5b07477.
97. A. I. Lupulescu, J. D. Rimer, In situ imaging of silicalite-1 surface growth reveals the mechanism of crystallization. *Science* **344**, 729–732 (2014).
98. A. I. Lupulescu, W. Qin, J. D. Rimer, Tuning zeolite precursor interactions by switching the valence of polyamine modifiers. *Langmuir*. **32**, 11888–11898 (2016).
99. A. I. Lupulescu, J. D. Rimer, Tailoring silicalite-1 crystal morphology with molecular modifiers. *Angew. Chemie - Int. Ed.* **51**, 3345–3349 (2012).
100. Q. Zhang, G. Chen, Y. Wang, M. Chen, G. Guo, J. Shi, J. Luo, J. Yu, Supporting Information High-Quality Single-Crystalline MFI-Type Nanozeolites: A Facile Synthetic Strategy and MTP Catalytic Studies (available at https://pubs.acs.org/doi/suppl/10.1021/acs.chemmater.8b00527/suppl_file/cm8b00527_si_001.pdf).
101. J. Zheng, W. Zhang, Z. Liu, Q. Huo, K. Zhu, X. Zhou, W. Yuan, Unraveling the non-classic crystallization of SAPO-34 in a dry gel system towards controlling meso-structure with the assistance of growth inhibitor: Growth mechanism, hierarchical structure control and catalytic properties. *Microporous Mesoporous Mater.* **225**, 74–87 (2016).
102. D. Jin, Z. Liu, J. Zheng, W. Hua, J. Chen, K. Zhu, X. Zhou, Nonclassical from-shell-to-core growth of hierarchically organized SAPO-11 with enhanced catalytic performance in hydroisomerization of n-heptane. *RSC Adv.* **6**, 32523–32533 (2016).
103. R. Li, A. Smolyakova, G. Maayan, J. D. Rimer, Designed peptoids as tunable modifiers of zeolite crystallization. *Chem. Mater.* **29**, 9536–9546 (2017).
104. A. I. Lupulescu, M. Kumar, J. D. Rimer, A facile strategy to design zeolite L crystals with tunable morphology and surface architecture. *J. Am. Chem. Soc.* **135**, 6608–6617 (2013).
105. R. Das, S. Ghosh, M. K. Naskar, Effect of secondary and tertiary alkylamines for the synthesis of Zeolite L. *Mater. Lett.* **143**, 94–97 (2015).

106. Z. Chen, C. Chen, J. Zhang, G. Zheng, Y. Wang, L. Dong, W. Qian, S. Bai, M. Hong, Zeolite Y microspheres with perpendicular mesochannels and metal@ Y heterostructures for catalytic and SERS applications. *J. Mater. Chem. A*, **6**, 6273–6281 (2018).
107. L. Zhang, Y. Chen, J.-G. Jiang, L. Xu, W. Guo, H. Xu, X.-D. Wen, P. Wu, Facile synthesis of ECNU-20 (IWR) hollow sphere zeolite composed of aggregated nanosheets. *Dalt. Trans.* **46**, 15641–15645 (2017).
108. S. Jegatheeswaran, C.-M. Cheng, C.-H. Cheng, Effects of adding alcohols on ZSM-12 synthesis. *Microporous Mesoporous Mater.* **201**, 24–34 (2015).
109. S. Al Aani, C. J. Wright, A. Atieh, N. Hilal, Engineering nanocomposite membranes: Addressing current challenges and future opportunities (2017), doi:10.1016/j.desal.2016.08.001.
110. L. Qi, H. Cölfen, M. Antonietti, Control of barite morphology by double-hydrophilic block copolymers. *Chem. Mater.* **12**, 2392–2403 (2000).
111. A. C. Doxey, M. W. Yaish, M. Griffith, B. J. McConkey, Ordered surface carbons distinguish antifreeze proteins and their ice-binding regions. *Nat. Biotechnol.* **24**, 852–855 (2006).
112. S. Farmanesh, S. Ramamoorthy, J. Chung, J. R. Asplin, P. Karande, J. D. Rimer, Specificity of growth inhibitors and their cooperative effects in calcium oxalate monohydrate crystallization. *J. Am. Chem. Soc.* **136**, 367–376 (2014).
113. S. Farmanesh, J. Chung, R. D. Sosa, J. H. Kwak, P. Karande, J. D. Rimer, Natural promoters of calcium oxalate monohydrate crystallization. *J. Am. Chem. Soc.* **136**, 12648–12657 (2014).
114. S. Farmanesh, B. G. Alamani, J. D. Rimer, Identifying alkali metal inhibitors of crystal growth: a selection criterion based on ion pair hydration energy. *Chem. Commun.* **51**, 13964–13967 (2015).
115. C. H. Bartholomew, Mechanisms of catalyst deactivation. *Appl. Catal. A Gen.* **212**, 17–60 (2001).
116. H. S. Cerqueira, G. Caeiro, L. Costa, F. R. Ribeiro, Deactivation of FCC catalysts. *J. Mol. Catal. A Chem.* **292**, 1–13 (2008).
117. S. Bhatia, J. Beltramini, D. D. Do, Deactivation of zeolite catalysts. *Catal. Rev. Eng.* **31**, 431–480 (1989).
118. M. L. Poutsma, Zeolite Chemistry and Catalysis. *ACS Monogr.* **171**, 437 (1976).
119. M. Guisnet, L. Costa, F. R. Ribeiro, Prevention of zeolite deactivation by coking. *J. Mol. Catal. A Chem.* **305**, 69–83 (2009).

120. J. Goetze, B. M. Weckhuysen, Spatiotemporal coke formation over zeolite ZSM-5 during the methanol-to-olefins process as studied with: Operando UV-vis spectroscopy: A comparison between H-ZSM-5 and Mg-ZSM-5. *Catal. Sci. Technol.* **8** (2018), doi:10.1039/c7cy02459b.
121. J. E. Schmidt, J. D. Poplawsky, B. Mazumder, Ö. Attila, D. Fu, D. A. M. de Winter, F. Meirer, S. R. Bare, B. M. Weckhuysen, Coke formation in a zeolite crystal during the methanol-to-hydrocarbons reaction as studied with atom probe tomography. *Angew. Chemie Int. Ed.* **55**, 11173–11177 (2016).
122. J. Kim, M. Choi, R. Ryoo, Effect of mesoporosity against the deactivation of MFI zeolite catalyst during the methanol-to-hydrocarbon conversion process. *J. Catal.* **269**, 219–228 (2010).
123. M. Bjørgen, U. Olsbye, S. Kolboe, Coke precursor formation and zeolite deactivation: mechanistic insights from hexamethylbenzene conversion. *J. Catal.* **215**, 30–44 (2003).
124. M. Guisnet, P. Magnoux, “Coking and Deactivation of Zeolites Influence of the Pore Structure” (1989), (available at https://ac.els-cdn.com/S0166983400823507/1-s2.0-S0166983400823507-main.pdf?_tid=67c72a54-0692-43cf-af3d-7b1c29a3051c&acdnat=1534367279_45641e229858d587ee6fca147cb23086).
125. M. Zhang, S. Xu, Y. Wei, J. Li, J. Chen, J. Wang, W. Zhang, S. Gao, X. Li, C. Wang, Z. Liu, Methanol conversion on ZSM-22, ZSM-35 and ZSM-5 zeolites: effects of 10-membered ring zeolite structures on methylcyclopentenyl cations and dual cycle mechanism. *RSC Adv.* **6**, 95855–95864 (2016).
126. F. R. Ribeiro, F. Alvarez, C. Henriques, F. Lemos, J. M. Lopes, M. F. Ribeiro, Structure-activity relationship in zeolites. *J. Mol. Catal. A Chem.* **96**, 245–270 (1995).
127. C. D. Chang, A. J. Silvestri, The conversion of methanol and other O-compounds to hydrocarbons over zeolite catalysts. *J. Catal.* **47**, 249–259 (1977).
128. M. Yang, D. Fan, Y. Wei, P. Tian, Z. Liu, Recent Progress in Methanol-to-Olefins (MTO) Catalysts. *Adv. Mater.* **31**, 1902181 (2019).
129. P. Tian, Y. Wei, M. Ye, Z. Liu, Methanol to Olefins (MTO): From Fundamentals to Commercialization. *ACS Catal.* **5**, 1922–1938 (2015).
130. K.-Y. Lee, S.-W. Lee, S.-K. Ihm, Acid Strength Control in MFI Zeolite for the Methanol-to-Hydrocarbons (MTH) Reaction. *Ind. Eng. Chem. Res.* **53**, 10072–10079 (2014).
131. U. Olsbye, S. Svelle, M. Bjørgen, P. Beato, T. V. W. Janssens, F. Joensen, S. Bordiga, K. P. Lillerud, Conversion of Methanol to Hydrocarbons: How Zeolite Cavity and Pore Size Controls Product Selectivity. *Angew. Chemie Int. Ed.* **51**, 5810–5831 (2012).

132. Z. Li, J. Martínez-Triguero, P. Concepción, J. Yu, A. Corma, Methanol to olefins: activity and stability of nanosized SAPO-34 molecular sieves and control of selectivity by silicon distribution. *Phys. Chem. Chem. Phys.* **15**, 14670–14680 (2013).
133. Y. Wei, D. Zhang, L. Xu, F. Chang, Y. He, S. Meng, B. Su, Z. Liu, Synthesis, characterization and catalytic performance of metal-incorporated SAPO-34 for chloromethane transformation to light olefins. *Catal. Today.* **131**, 262–269 (2008).
134. S. Ilias, R. Khare, A. Malek, A. Bhan, A descriptor for the relative propagation of the aromatic- and olefin-based cycles in methanol-to-hydrocarbons conversion on H-ZSM-5. *J. Catal.* **303**, 135–140 (2013).
135. R. Khare, D. Millar, A. Bhan, A mechanistic basis for the effects of crystallite size on light olefin selectivity in methanol-to-hydrocarbons conversion on MFI. *J. Catal.* **321**, 23–31 (2015).
136. I. M. Dahl, S. Kolboe, On the reaction mechanism for hydrocarbon formation from methanol over SAPO-34: 2. Isotopic labeling studies of the co-reaction of propene and methanol. *J. Catal.* **161**, 304–309 (1996).
137. I. M. Dahl, S. Kolboe, On the reaction mechanism for propene formation in the MTO reaction over SAPO-34. *Catal. Letters.* **20**, 329–336 (1993).
138. I. M. Dahl, S. Kolboe, On the reaction mechanism for hydrocarbon formation from methanol over SAPO-34: I. Isotopic labeling studies of the co-reaction of ethene and methanol. *J. Catal.* **149**, 458–464 (1994).
139. W. Song, D. M. Marcus, H. Fu, J. O. Ehresmann, J. F. Haw, An oft-studied reaction that may never have been: Direct catalytic conversion of methanol or dimethyl ether to hydrocarbons on the solid acids HZSM-5 or HSAPO-34. *J. Am. Chem. Soc.* **124**, 3844–3845 (2002).
140. Z. Shi, M. Neurock, A. Bhan, Methanol-to-olefins catalysis on HSSZ-13 and HSAPO-34 and its relationship to acid strength. *ACS Catal.* **11**, 1222–1232 (2021).
141. A. Hwang, A. Bhan, Bifunctional strategy coupling Y₂O₃-catalyzed alkanal decomposition with methanol-to-olefins catalysis for enhanced lifetime. *ACS Catal.* **7**, 4417–4422 (2017).
142. P. Bollini, T. T. Chen, M. Neurock, A. Bhan, Mechanistic role of water in HSSZ-13 catalyzed methanol-to-olefins conversion. *Catal. Sci. Technol.* **9**, 4374–4383 (2019).
143. J. F. Haw, D. M. Marcus, Well-defined (supra) molecular structures in zeolite methanol-to-olefin catalysis. *Top. Catal.* **34**, 41–48 (2005).

144. T. V. W. Janssens, A new approach to the modeling of deactivation in the conversion of methanol on zeolite catalysts. *J. Catal.* **264**, 130–137 (2009).
145. F. L. Bleken, T. V. W. Janssens, S. Svelle, U. Olsbye, Product yield in methanol conversion over ZSM-5 is predominantly independent of coke content. *Microporous Mesoporous Mater.* **164**, 190–198 (2012).
146. M. W. Erichsen, S. Svelle, U. Olsbye, H-SAPO-5 as methanol-to-olefins (MTO) model catalyst: Towards elucidating the effects of acid strength. *J. Catal.* **298**, 94–101 (2013).
147. B. L. Foley, B. A. Johnson, A. Bhan, Kinetic evaluation of deactivation pathways in methanol-to-hydrocarbon catalysis on HZSM-5 with formaldehyde, olefinic, dieneic, and aromatic Co-Feeds. *ACS Catal.* **11**, 3628–3637 (2021).
148. J. D. Rimer, A. Chawla, T. T. Le, Crystal engineering for catalysis. *Annu. Rev. Chem. Biomol. Eng.* **9**, 283–309 (2018).
149. S. Mintova, V. Valtchev, in *Studies in surface science and catalysis* (Elsevier, 1999), vol. 125, pp. 141–148.
150. E.-P. Ng, D. Chateigner, T. Bein, V. Valtchev, S. Mintova, Capturing ultrasmall EMT zeolite from template-free systems. *Science* **335**, 70–73 (2012).
151. H. Y. Luo, V. K. Michaelis, S. Hodges, R. G. Griffin, Y. Román-Leshkov, One-pot synthesis of MWW zeolite nanosheets using a rationally designed organic structure-directing agent. *Chem. Sci.* **6**, 6320–6324 (2015).
152. A. Corma, V. Fornes, S. B. Pergher, T. L. M. Maesen, J. G. Buglass, Delaminated zeolite precursors as selective acidic catalysts. *Nature*. **396**, 353–356 (1998).
153. Y. Zhou, Y. Mu, M.-F. Hsieh, B. Kabius, C. Pacheco, C. Bator, R. M. Rioux, J. D. Rimer, Enhanced Surface Activity of MWW Zeolite Nanosheets Prepared via a One-Step Synthesis. *J. Am. Chem. Soc.* **142**, 8211–8222 (2020).
154. M. Choi, K. Na, J. Kim, Y. Sakamoto, O. Terasaki, R. Ryoo, Stable single-unit-cell nanosheets of zeolite MFI as active and long-lived catalysts. *Nature*. **461** (2009), doi:10.1038/nature08288.
155. W. J. Roth, P. Nachtigall, R. E. Morris, J. Čejka, Two-dimensional zeolites: Current status and perspectives. *Chem. Rev.* **114**, 4807–4837 (2014).
156. W. J. Roth, P. Nachtigall, R. E. Morris, P. S. Wheatley, V. R. Seymour, S. E. Ashbrook, P. Chlubná, L. Grajciar, M. Položij, A. Zukal, A family of zeolites with controlled pore size prepared using

- a top-down method. *Nat. Chem.* **5**, 628–633 (2013).
157. S. Zanardi, A. Alberti, G. Cruciani, A. Corma, V. Fornes, M. Brunelli, Crystal Structure Determination of Zeolite Nu-6 (2) and Its Layered Precursor Nu-6 (1). *Angew. chemie Int. Ed.* **43**, 4933–4937 (2004).
158. T. Moteki, W. Chaikittisilp, A. Shimojima, T. Okubo, Silica sodalite without occluded organic matters by topotactic conversion of lamellar precursor. *J. Am. Chem. Soc.* **130**, 15780–15781 (2008).
159. L. Schreyeck, P. Caullet, J.-C. Mougènel, J.-L. Guth, B. Marler, A layered microporous aluminosilicate precursor of FER-type zeolite. *J. Chem. Soc. Chem. Commun.*, 2187–2188 (1995).
160. W. J. Roth, C. T. Kresge, J. C. Vartuli, M. E. Leonowicz, A. S. Fung, S. B. McCullen, in *Catalysis by Microporous Materials*, H. K. Beyer, H. G. Karge, I. Kiricsi, J. B. B. T.-S. in S. S. and C. Nagy, Eds. (Elsevier, 1995; <https://www.sciencedirect.com/science/article/pii/S016729910681236X>), vol. 94, pp. 301–308.
161. G. G. Juttu, R. F. Lobo, Characterization and catalytic properties of MCM-56 and MCM-22 zeolites. *Microporous Mesoporous Mater.* **40**, 9–23 (2000).
162. J. Pérez-Ramírez, C. H. Christensen, K. Egeblad, C. H. Christensen, J. C. Groen, Hierarchical zeolites: enhanced utilisation of microporous crystals in catalysis by advances in materials design. *Chem. Soc. Rev.* **37**, 2530–2542 (2008).
163. W. Schwieger, A. G. Machoke, T. Weissenberger, A. Inayat, T. Selvam, M. Klumpp, A. Inayat, Hierarchy concepts: classification and preparation strategies for zeolite containing materials with hierarchical porosity. *Chem. Soc. Rev.* **45**, 3353–3376 (2016).
164. K. Li, J. Valla, J. Garcia-Martinez, Realizing the commercial potential of hierarchical zeolites: New opportunities in catalytic cracking. *ChemCatChem* (2014), , doi:10.1002/cctc.201300345.
165. D. Verboekend, G. Vilé, J. Pérez-Ramírez, Hierarchical Y and USY Zeolites Designed by Post-Synthetic Strategies. *Adv. Funct. Mater.* **22**, 916–928 (2012).
166. G. Pacheco-Malagón, P. Pérez-Romo, N. A. Sánchez-Flores, M. L. Guzmán-Castillo, C. López-Franco, J. M. Saniger, F. Hernández-Beltrán, J. J. Fripiat, Crystallization of Zeolites from Organo-Silicic Colloids. *Inorg. Chem.* **45**, 3408–3414 (2006).
167. M. L. Guzmán-Castillo, H. Armendáriz-Herrera, P. Pérez-Romo, F. Hernández-Beltrán, S. Ibarra, J. S. Valente, J. J. Fripiat, Y zeolite depolymerization–recrystallization: Simultaneous formation of hierarchical porosity and Na dislodging. *Microporous Mesoporous Mater.* **143**, 375–382 (2011).

168. Z. X. Yang, Y. D. Xia, R. Mokaya, Zeolite ZSM-5 with Unique Supermicropores Synthesized Using Mesoporous Carbon as a Template. *Adv. Mater.* **16**, 727–732 (2004).
169. S.-S. Kim, J. Shah, T. J. Pinnavaia, Colloid-Imprinted Carbons as Templates for the Nanocasting Synthesis of Mesoporous ZSM-5 Zeolite. *Chem. Mater.* **15**, 1664–1668 (2003).
170. A. H. Janssen, I. Schmidt, C. J. H. Jacobsen, A. J. Koster, K. P. de Jong, Exploratory study of mesopore templating with carbon during zeolite synthesis. *Microporous Mesoporous Mater.* **65**, 59–75 (2003).
171. W. Fan, M. A. Snyder, S. Kumar, P. S. Lee, W. C. Yoo, A. V. McCormick, R. Lee Penn, A. Stein, M. Tsapatsis, Hierarchical nanofabrication of microporous crystals with ordered mesoporosity. *Nat. Mater.* **7**, 984–991 (2008).
172. H. J. Cho, P. Dornath, W. Fan, Synthesis of Hierarchical Sn-MFI as Lewis Acid Catalysts for Isomerization of Cellulosic Sugars. *ACS Catal.* **4**, 2029–2037 (2014).
173. J. Xie, X. Yao, Q. Cheng, I. P. Madden, P. Dornath, C.-C. Chang, W. Fan, D. Wang, Three Dimensionally Ordered Mesoporous Carbon as a Stable, High-Performance Li–O₂ Battery Cathode. *Angew. Chemie Int. Ed.* **54**, 4299–4303 (2015).
174. D. H. Park, S. S. Kim, H. Wang, T. J. Pinnavaia, M. C. Papapetrou, A. A. Lappas, K. S. Triantafyllidis, Selective Petroleum Refining Over a Zeolite Catalyst with Small Intracrystal Mesopores. *Angew. Chemie Int. Ed.* **48**, 7645–7648 (2009).
175. Y. Jin, Y. Li, S. Zhao, Z. Lv, Q. Wang, X. Liu, L. Wang, Synthesis of mesoporous MOR materials by varying temperature crystallizations and combining ternary organic templates. *Microporous Mesoporous Mater.* **147**, 259–266 (2012).
176. Y. Tao, H. Kanoh, K. Kaneko, Synthesis of Mesoporous Zeolite A by Resorcinol–Formaldehyde Aerogel Templating. *Langmuir.* **21**, 504–507 (2005).
177. H. Wang, T. J. Pinnavaia, MFI Zeolite with Small and Uniform Intracrystal Mesopores. *Angew. Chemie Int. Ed.* **45**, 7603–7606 (2006).
178. K. Na, C. Jo, J. Kim, K. Cho, J. Jung, Y. Seo, R. J. Messinger, B. F. Chmelka, R. Ryoo, Directing zeolite structures into hierarchically nanoporous architectures. *Science* **333**, 328–332 (2011).
179. X. Zhang, D. Liu, D. Xu, S. Asahina, K. A. Cychosz, K. V. Agrawal, Y. Al Wahedi, A. Bhan, S. Al Hashimi, O. Terasaki, M. Thommes, M. Tsapatsis, Synthesis of self-pillared zeolite nanosheets by repetitive branching. *Science* **336**, 1684–1687 (2012).

180. D. Xu, O. Abdelrahman, S. H. Ahn, Y. Guefrachi, A. Kuznetsov, L. Ren, S. Hwang, M. Khaleel, S. Al Hassan, D. Liu, S. B. Hong, P. Dauenhauer, M. Tsapatsis, A quantitative study of the structure–activity relationship in hierarchical zeolites using liquid-phase reactions. *AIChE J.* **65**, 1067–1075 (2019).
181. R. Jain, A. Chawla, N. Linares, J. García Martínez, J. D. Rimer, Spontaneous Pillaring of Pentasil Zeolites. *Adv. Mater.* **33**, 2100897 (2021).
182. D. Erdemir, A. Y. Lee, A. S. Myerson, Nucleation of Crystals from Solution: Classical and Two-Step Models. *Acc. Chem. Res.* **42**, 621–629 (2009).
183. Y. Peng, F. Wang, Z. Wang, A. M. Alsayed, Z. Zhang, A. G. Yodh, Y. Han, Two-step nucleation mechanism in solid–solid phase transitions. *Nat. Mater.* **14**, 101–108 (2015).
184. M. K. Choudhary, R. Jain, J. D. Rimer, In situ imaging of two-dimensional surface growth reveals the prevalence and role of defects in zeolite crystallization. *Proc. Natl. Acad. Sci.*, 202011806 (2020).
185. V. Van Speybroeck, K. Hemelsoet, K. De Wispelaere, Q. Qian, J. Van der Mynsbrugge, B. De Sterck, B. M. Weckhuysen, M. Waroquier, Mechanistic Studies on Chabazite-Type Methanol-to-Olefin Catalysts: Insights from Time-Resolved UV/Vis Microspectroscopy Combined with Theoretical Simulations. *ChemCatChem.* **5**, 173–184 (2013).
186. J. Zhu, Y. Zhu, L. Zhu, M. Rigutto, A. van der Made, C. Yang, S. Pan, L. Wang, L. Zhu, Y. Jin, Q. Sun, Q. Wu, X. Meng, D. Zhang, Y. Han, J. Li, Y. Chu, A. Zheng, S. Qiu, X. Zheng, F.-S. Xiao, Highly Mesoporous Single-Crystalline Zeolite Beta Synthesized Using a Nonsurfactant Cationic Polymer as a Dual-Function Template. *J. Am. Chem. Soc.* **136**, 2503–2510 (2014).
187. Z. Bohström, K. P. Lillerud, Preparation of chabazite with mesopores templated from a cationic polymer. *Microporous Mesoporous Mater.* **271**, 295–300 (2018).
188. R. Li, A. Chawla, N. Linares, J. G. Sutjianto, K. W. Chapman, J. G. Martínez, J. D. Rimer, Diverse Physical States of Amorphous Precursors in Zeolite Synthesis. *Ind. Eng. Chem. Res.* **57**, 8460–8471 (2018).
189. K. N. Olafson, R. Li, B. G. Alamani, J. D. Rimer, Engineering Crystal Modifiers: Bridging Classical and Nonclassical Crystallization. *Chem. Mater.* **28**, 8453–8465 (2016).
190. P. C. Hiemenz, R. Rajagopalan, *Principles of Colloid and Surface Chemistry, revised and expanded* (CRC press, 2016).

191. N. J. W. Penfold, Y. Ning, P. Verstraete, J. Smets, S. P. Armes, Cross-linked cationic diblock copolymer worms are superflocculants for micrometer-sized silica particles. *Chem. Sci.* **7**, 6894–6904 (2016).
192. D. Bauer, E. Killmann, W. Jaeger, Flocculation and stabilization of colloidal silica by the adsorption of poly-diallyl-dimethyl-ammoniumchloride (PDADMAC) and of copolymers of DADMAC with N-methyl-N-vinyl- acetamide (NMVA). *Colloid Polym. Sci.* **276**, 698–708 (1998).
193. V. K. La Mer, Nucleation in Phase Transitions. *Ind. Eng. Chem.* **44**, 1270–1277 (1952).
194. V. K. LaMer, R. H. Dinegar, Theory, Production and Mechanism of Formation of Monodispersed Hydrosols. *J. Am. Chem. Soc.* **72**, 4847–4854 (1950).
195. C. B. Whitehead, S. Özkar, R. G. Finke, LaMer’s 1950 Model for Particle Formation of Instantaneous Nucleation and Diffusion-Controlled Growth: A Historical Look at the Model’s Origins, Assumptions, Equations, and Underlying Sulfur Sol Formation Kinetics Data. *Chem. Mater.* **31**, 7116–7132 (2019).
196. C. Paolucci, I. Khurana, A. A. Parekh, S. Li, A. J. Shih, H. Li, J. R. Di Iorio, J. D. Albarracin-Caballero, A. Yezerets, J. T. Miller, Dynamic multinuclear sites formed by mobilized copper ions in NOx selective catalytic reduction. *Science* **357**, 898–903 (2017).
197. E. M. Gallego, M. T. Portilla, C. Paris, A. León-Escamilla, M. Boronat, M. Moliner, A. Corma, *Science* in press, doi:10.1126/science.aal0121.
198. L. Karwacki, M. H. F. Kox, D. A. M. De Winter, M. R. Drury, J. D. Meeldijk, E. Stavitski, W. Schmidt, M. Mertens, P. Cubillas, N. John, Morphology-dependent zeolite intergrowth structures leading to distinct internal and outer-surface molecular diffusion barriers. *Nat. Mater.* **8**, 959–965 (2009).
199. H. Awala, J.-P. Gilson, R. Retoux, P. Boullay, J.-M. Goupil, V. Valtchev, S. Mintova, Template-free nanosized faujasite-type zeolites. *Nat. Mater.* **14**, 447–451 (2015).
200. A. Hwang, T. T. Le, Z. Shi, H. Dai, J. D. Rimer, A. Bhan, Effects of diffusional constraints on lifetime and selectivity in methanol-to-olefins catalysis on HSAPO-34. *J. Catal.* **369**, 122–132 (2019).
201. S. Mintova, M. Jaber, V. Valtchev, Nanosized microporous crystals: emerging applications. *Chem. Soc. Rev.* **44**, 7207–7233 (2015).
202. V. J. Margarit, M. R. Díaz-Rey, M. T. Navarro, C. Martínez, A. Corma, Direct Synthesis of Nano-Ferrierite along the 10-Ring-Channel Direction Boosts Their Catalytic Behavior. *Angew. Chemie Int. Ed.* **57**, 3459–3463 (2018).

203. E. M. Gallego, C. Paris, M. R. Díaz-Rey, M. E. Martínez-Armero, J. Martínez-Triguero, C. Martínez, M. Moliner, A. Corma, Simple organic structure directing agents for synthesizing nanocrystalline zeolites. *Chem. Sci.* **8**, 8138–8149 (2017).
204. Y. Shen, T. T. Le, D. Fu, J. E. Schmidt, M. Filez, B. M. Weckhuysen, J. D. Rimer, Deconvoluting the Competing Effects of Zeolite Framework Topology and Diffusion Path Length on Methanol to Hydrocarbons Reaction. *ACS Catal.* **8**, 11042–11053 (2018).
205. I. Yarulina, K. De Wispelaere, S. Bailleul, J. Goetze, M. Radersma, E. Abou-Hamad, I. Vollmer, M. Goesten, B. Mezari, E. J. M. Hensen, Structure–performance descriptors and the role of Lewis acidity in the methanol-to-propylene process. *Nat. Chem.* **10**, 804–812 (2018).
206. E. Borodina, F. Meirer, I. Lezcano-González, M. Mokhtar, A. M. Asiri, S. A. Al-Thabaiti, S. N. Basahel, J. Ruiz-Martinez, B. M. Weckhuysen, Influence of the reaction temperature on the nature of the active and deactivating species during methanol to olefins conversion over H-SSZ-13. *ACS Catal.* **5**, 992–1003 (2015).
207. N. Laloué, C. Laroche, H. Jobic, A. Methivier, Kinetic Monte Carlo study of binary diffusion in silicalite. *Adsorption.* **13**, 491–500 (2007).
208. P. D. Kolokathis, E. Pantatosaki, C.-A. Gatsiou, H. Jobic, G. K. Papadopoulos, D. N. Theodorou, Dimensionality reduction of free energy profiles of benzene in silicalite-1: calculation of diffusion coefficients using transition state theory. *Mol. Simul.* **40**, 80–100 (2014).
209. T. R. Forester, W. Smith, Bluemoon simulations of benzene in silicalite-1 Prediction of free energies and diffusion coefficients. *J. Chem. Soc. Faraday Trans.* **93**, 3249–3257 (1997).
210. M. J. Abraham, T. Murtola, R. Schulz, S. Páll, J. C. Smith, B. Hess, E. Lindahl, GROMACS: High performance molecular simulations through multi-level parallelism from laptops to supercomputers. *SoftwareX.* **1**, 19–25 (2015).
211. R. T. Cygan, J.-J. Liang, A. G. Kalinichev, Molecular models of hydroxide, oxyhydroxide, and clay phases and the development of a general force field. *J. Phys. Chem. B.* **108**, 1255–1266 (2004).
212. L. S. Dodda, I. Cabeza de Vaca, J. Tirado-Rives, W. L. Jorgensen, LigParGen web server: an automatic OPLS-AA parameter generator for organic ligands. *Nucleic Acids Res.* **45**, W331–W336 (2017).
213. P. D. Kolokathis, G. Káli, H. Jobic, D. N. Theodorou, Diffusion of aromatics in silicalite-1: Experimental and theoretical evidence of entropic barriers. *J. Phys. Chem. C.* **120**, 21410–21426 (2016).

214. G. Bussi, D. Donadio, M. Parrinello, Canonical sampling through velocity rescaling. *J. Chem. Phys.* **126**, 14101 (2007).
215. L. Wang, Z. Zhang, C. Yin, Z. Shan, F.-S. Xiao, Hierarchical mesoporous zeolites with controllable mesoporosity templated from cationic polymers. *Microporous mesoporous Mater.* **131**, 58–67 (2010).
216. Z. Ristanović, J. P. Hofmann, U. Deka, T. U. Schüllli, M. Rohnke, A. M. Beale, B. M. Weckhuysen, Intergrowth Structure and Aluminium Zoning of a Zeolite ZSM-5 Crystal as Resolved by Synchrotron-Based Micro X-Ray Diffraction Imaging. *Angew. Chemie.* **125**, 13624–13628 (2013).
217. K. Ding, A. Corma, J. A. Maciá-Agulló, J. G. Hu, S. Krämer, P. C. Stair, G. D. Stucky, Constructing hierarchical porous zeolites via kinetic regulation. *J. Am. Chem. Soc.* **137**, 11238–11241 (2015).
218. H. Zhu, Z. Liu, D. Kong, Y. Wang, Z. Xie, Synthesis and catalytic performances of mesoporous zeolites templated by polyvinyl butyral gel as the mesopore directing agent. *J. Phys. Chem. C.* **112**, 17257–17264 (2008).
219. H. Zhang, H. Zhang, Y. Zhao, Z. Shi, Y. Zhang, Y. Tang, Seeding Bundlelike MFI Zeolite Mesocrystals: A Dynamic, Nonclassical Crystallization via Epitaxially Anisotropic Growth. *Chem. Mater.* **29**, 9247–9255 (2017).
220. S. Kim, G. Park, M. H. Woo, G. Kwak, S. K. Kim, Control of Hierarchical Structure and Framework-Al Distribution of ZSM-5 via Adjusting Crystallization Temperature and Their Effects on Methanol Conversion. *ACS Catal.* **9**, 2880–2892 (2019).
221. A. Ghorbanpour, A. Gumidyala, L. C. Grabow, S. P. Crossley, J. D. Rimer, Epitaxial Growth of ZSM-5@Silicalite-1: A Core-Shell Zeolite Designed with Passivated Surface Acidity. **9**, 4006–4016 (2015).
222. E. C. Nordvang, E. Borodina, J. Ruiz-Martínez, R. Fehrmann, B. M. Weckhuysen, Effects of Coke Deposits on the Catalytic Performance of Large Zeolite H-ZSM-5 Crystals during Alcohol-to-Hydrocarbon Reactions as Investigated by a Combination of Optical Spectroscopy and Microscopy. *Chemistry.* **21**, 17324–17335 (2015).
223. D. M. Ruthven, M. Eic, E. Richard, Diffusion of C8 aromatic hydrocarbons in silicalite. *Zeolites.* **11**, 647–653 (1991).
224. K. Góra-Marek, K. Tarach, M. Choi, 2,6-Di-tert-butylpyridine Sorption Approach to Quantify

- the External Acidity in Hierarchical Zeolites. *J. Phys. Chem. C*. **118**, 12266–12274 (2014).
225. H. Awala, J. P. Gilson, R. Retoux, P. Boullay, J. M. Goupil, V. Valtchev, S. Mintova, Template-free nanosized faujasite-type zeolites. *Nat. Mater.* **14**, 447–451 (2015).
226. O. Muraza, Maximizing Diesel Production through Oligomerization: A Landmark Opportunity for Zeolite Research. *Ind. Eng. Chem. Res.* **54**, 781–789 (2015).
227. M. H. M. Ahmed, O. Muraza, A. M. Al-Amer, K. Miyake, N. Nishiyama, Development of hierarchical EU-1 zeolite by sequential alkaline and acid treatments for selective dimethyl ether to propylene (DTP). *Appl. Catal. A Gen.* **497**, 127–134 (2015).
228. S. S. Hassani, F. Salehirad, H. R. Aghabozorg, Z. Sobat, Synthesis and morphology of nanosized zeolite L. *Cryst. Res. Technol.* **45**, 183–187 (2010).
229. L. Schreyeck, P. Caullet, J. C. Mougénel, J. L. Guth, B. Marler, PREFER: a new layered (alumino) silicate precursor of FER-type zeolite. *Microporous Mater.* **6**, 259–271 (1996).
230. P. Kumar, K. V. Agrawal, M. Tsapatsis, K. A. Mkhoyan, Quantification of thickness and wrinkling of exfoliated two-dimensional zeolite nanosheets. *Nat. Commun.* **6**, 7128 (2015).
231. P. Wuamprakhon, C. Wattanakit, C. Warakulwit, T. Yutthalekha, W. Wannapakdee, S. Ittisanronnchai, J. Limtrakul, Direct synthesis of hierarchical ferrierite nanosheet assemblies via an organosilane template approach and determination of their catalytic activity. *Microporous Mesoporous Mater.* **219**, 1–9 (2016).
232. M. V Opanasenko, W. J. Roth, J. Čejka, Two-dimensional zeolites in catalysis: current status and perspectives. *Catal. Sci. Technol.* **6**, 2467–2484 (2016).
233. Y. Lee, M. B. Park, P. S. Kim, A. Vicente, C. Fernandez, I.-S. Nam, S. B. Hong, Synthesis and Catalytic Behavior of Ferrierite Zeolite Nanoneedles. *ACS Catal.* **3**, 617–621 (2013).
234. W. Chu, F. Chen, C. Guo, X. Li, X. Zhu, Y. Gao, S. Xie, S. Liu, N. Jiang, L. Xu, Synthesis of FER zeolite with piperidine as structure-directing agent and its catalytic application. *Chinese J. Catal.* **38**, 1880–1887 (2017).
235. H. Xu, W. Chen, G. Zhang, P. Wei, Q. Wu, L. Zhu, X. Meng, X. Li, J. Fei, S. Han, Q. Zhu, A. Zheng, Y. Ma, F.-S. Xiao, Ultrathin nanosheets of aluminosilicate FER zeolites synthesized in the presence of a sole small organic ammonium [†] (2019), doi:10.1039/c9ta04833b.
236. W. Chu, X. Li, X. Zhu, S. Xie, C. Guo, S. Liu, F. Chen, L. Xu, Size-controlled synthesis of hierarchical ferrierite zeolite and its catalytic application in 1-butene skeletal isomerization. *Microporous*

Mesoporous Mater. **240**, 189–196 (2017).

237. C. L. Kibby, A. J. Perrotta, F. E. Massoth, Composition and catalytic properties of synthetic ferrierite. *J. Catal.* **35**, 256–272 (1974).

238. J. Liu, H. Xue, X. Huang, Y. Li, W. Shen, Dimethyl Ether Carbonylation to Methyl Acetate over HZSM-35. *Catal. Letters.* **139**, 33–37 (2010).

239. L. Qi, J. Li, L. Xu, Z. Liu, Evolution of the reaction mechanism during the MTH induction period over the 2-dimensional FER zeolite. *RSC Adv.* **6**, 56698–56704 (2016).

240. A. Corma, U. Diaz, M. E. Domine, V. Fornés, AlITQ-6 and TiITQ-6: Synthesis, Characterization, and Catalytic Activity. *Angew. Chemie Int. Ed.* **39**, 1499–1501 (2000).

241. E. Catizzone, M. Migliori, A. Aloise, R. Lamberti, G. Giordano, Hierarchical Low Si/Al Ratio Ferrierite Zeolite by Sequential Postsynthesis Treatment: Catalytic Assessment in Dehydration Reaction of Methanol. *J. Chem.* **2019**, 3084356 (2019).

242. A. Bonilla, D. Baudouin, J. Pérez-Ramírez, Desilication of ferrierite zeolite for porosity generation and improved effectiveness in polyethylene pyrolysis. *J. Catal.* **265**, 170–180 (2009).

243. H. Dai, Y. Shen, T. Yang, C. Lee, D. Fu, A. Agarwal, T. T. Le, M. Tsapatsis, J. C. Palmer, B. M. Weckhuysen, P. J. Dauenhauer, X. Zou, J. D. Rimer, Finned zeolite catalysts. *Nat. Mater.* **19**, 1074–1080 (2020).

244. M. O. Cichocka, J. Ångström, B. Wang, X. Zou, S. Smeets, High-throughput continuous rotation electron diffraction data acquisition via software automation. *J. Appl. Crystallogr.* **51**, 1652–1661 (2018).

245. W. Wan, J. Sun, J. Su, S. Hovmöller, X. Zou, Three-dimensional rotation electron diffraction: software RED for automated data collection and data processing. *J. Appl. Crystallogr.* **46**, 1863–1873 (2013).

246. D. N. Mastronarde, S. R. Held, Automated tilt series alignment and tomographic reconstruction in IMOD. *J. Struct. Biol.* **197**, 102–113 (2017).

247. A. Hwang, D. Prieto-Centurion, A. Bhan, Isotopic tracer studies of methanol-to-olefins conversion over HSAPO-34: The role of the olefins-based catalytic cycle. *J. Catal.* **337**, 52–56 (2016).

248. W. Qin, Y. Zhou, J. D. Rimer, Deleterious effects of non-framework Al species on the catalytic performance of ZSM-5 crystals synthesized at low temperature. *React. Chem. Eng.* **4**, 1957–1968 (2019).

249. N. Danilina, F. Krumeich, S. A. Castelanelli, J. A. Van Bokhoven, Where Are the Active Sites

in Zeolites? Origin of Aluminum Zoning in ZSM-5, doi:10.1021/jp1006044.

250. P. A. Vaughan, The crystal structure of the zeolite ferrierite. *Acta Crystallogr.* **21**, 983–990 (1966).
251. A. A. Gabrienko, I. G. Danilova, S. S. Arzumanov, L. V. Pirutko, D. Freude, A. G. Stepanov, Direct Measurement of Zeolite Brønsted Acidity by FTIR Spectroscopy: Solid-State ^1H MAS NMR Approach for Reliable Determination of the Integrated Molar Absorption Coefficients. *J. Phys. Chem. C.* **122**, 25386–25395 (2018).
252. T. T. Le, A. Chawla, J. D. Rimer, Impact of acid site speciation and spatial gradients on zeolite catalysis. *J. Catal.* **391**, 56–68 (2020).
253. D. Jo, S. B. Hong, M. A. Camblor, Monomolecular Skeletal Isomerization of 1-Butene over Selective Zeolite Catalysts. *ACS Catal.* **5**, 2270–2274 (2015).
254. P. Lu, S. Ghosh, M. Dorneles de Mello, H. S. Kamaluddin, X. Li, G. Kumar, X. Duan, M. Abeykoon, J. A. Boscoboinik, L. Qi, H. Dai, T. Luo, S. Al-Thabaiti, K. Narasimharao, Z. Khan, J. D. Rimer, A. T. Bell, P. Dauenhauer, K. A. Mkhoyan, M. Tsapatsis, Few-Unit-Cell MFI Zeolite Synthesized using a Simple Di-quaternary Ammonium Structure-Directing Agent. *Angew. Chemie Int. Ed.* **n/a** (2021), doi:<https://doi.org/10.1002/anie.202104574>.
255. A. Molino, K. A. Łukaszuk, D. Rojo-Gama, K. P. Lillerud, U. Olsbye, S. Bordiga, S. Svelle, P. Beato, Conversion of methanol to hydrocarbons over zeolite ZSM-23 (MTT): exceptional effects of particle size on catalyst lifetime. *Chem. Commun.* **53**, 6816–6819 (2017).
256. H. van Heyden, S. Mintova, T. Bein, Nanosized SAPO-34 Synthesized from Colloidal Solutions. *Chem. Mater.* **20**, 2956–2963 (2008).

Appendix A Supplementary Information for Chapter 2

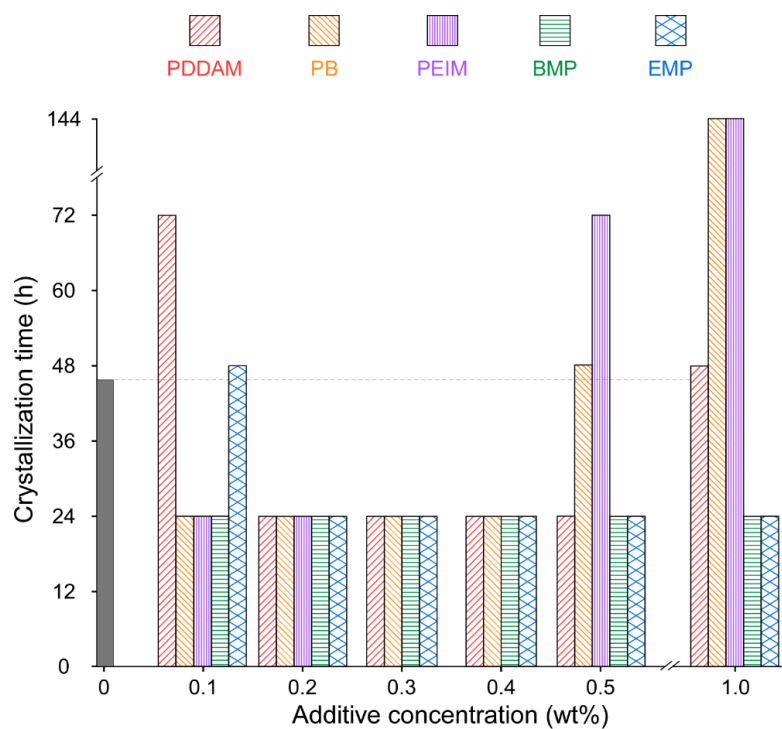


Figure A1. Powder X-ray diffraction patterns of SSZ-13 syntheses at 180 °C with the following modifiers: (A) PDDAM, (B) PB, (C) PEIM, (D) EMP, and (E) BMP.

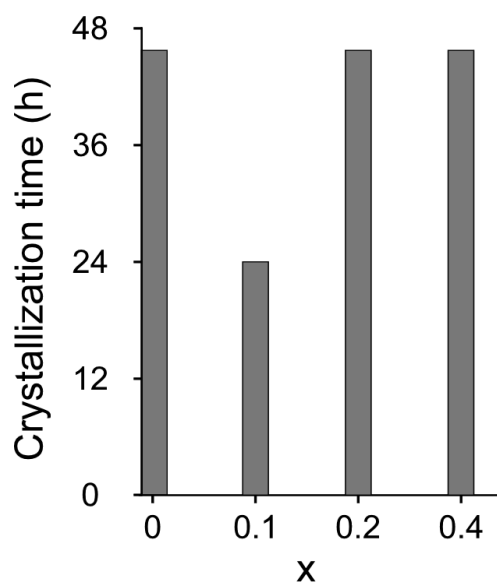


Figure A2. SSZ-13 crystallization time as a function of TMAda concentration for syntheses at 180 °C. The gel composition is 0.052 Al(OH)₃: 1 SiO₂: 0.2 NaOH: 44 H₂O: (0.1+x) TMAda: x HCl where x is the increased molar concentration of TMAda and/or HCl compared with the control.

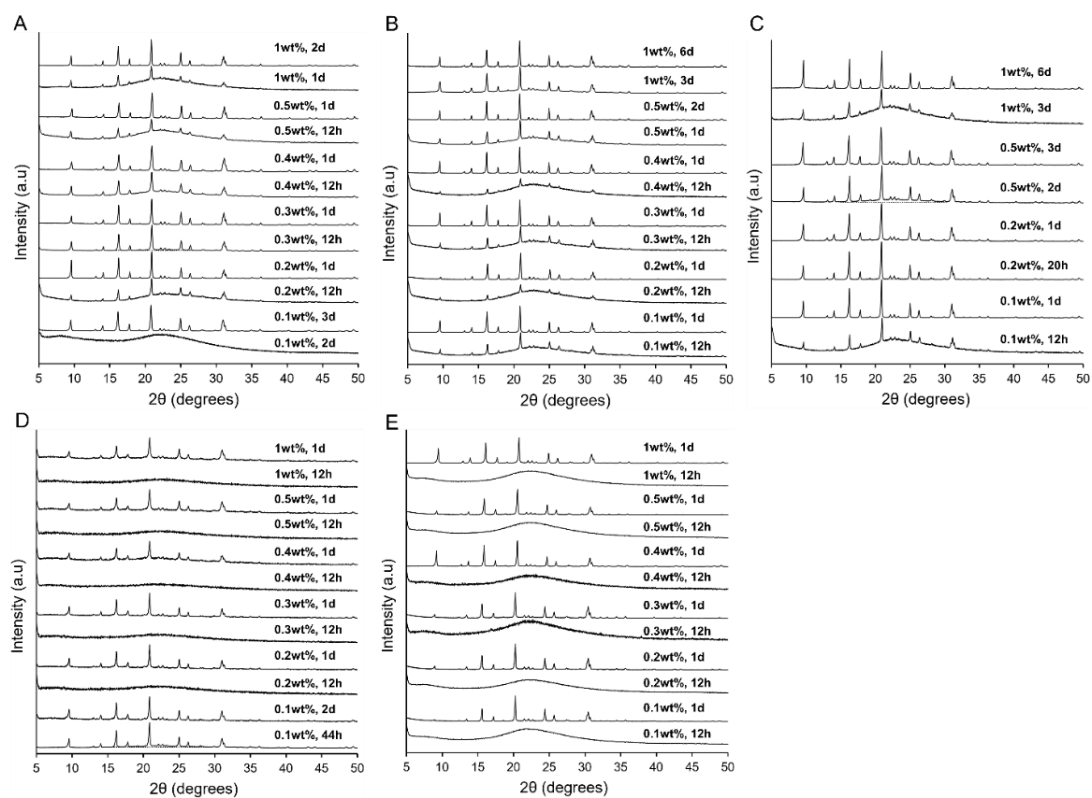


Figure A3. Powder X-ray diffraction patterns of SSZ-13 syntheses at 180 °C with the following modifiers: (A) PDDAM, (B) PB, (C) PEIM, (D) EMP, and (E) BMP.

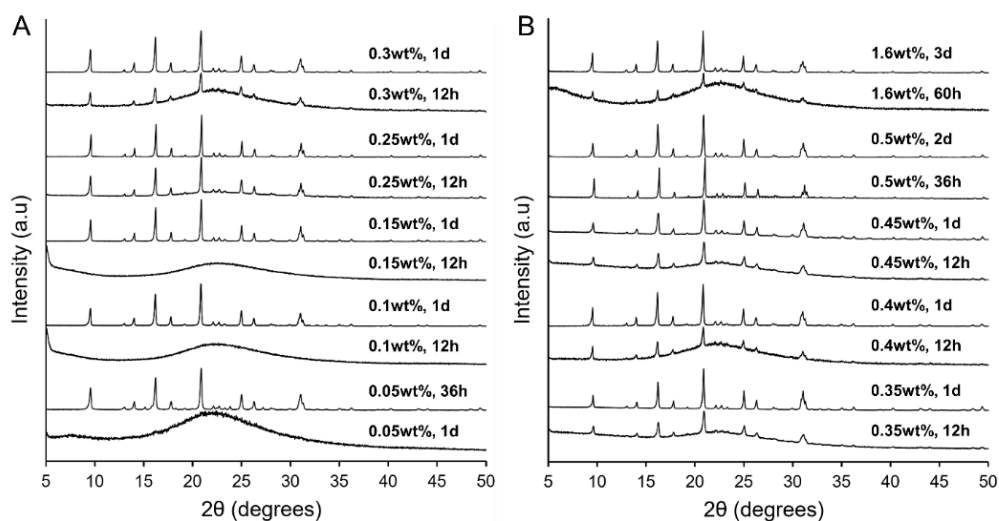


Figure A4. Powder X-ray diffraction patterns of SSZ-13 syntheses with PDDA at 180 °C ranging (A) from 0.05wt% to 0.3wt% and (B) from 0.35wt% to 1.6wt%.

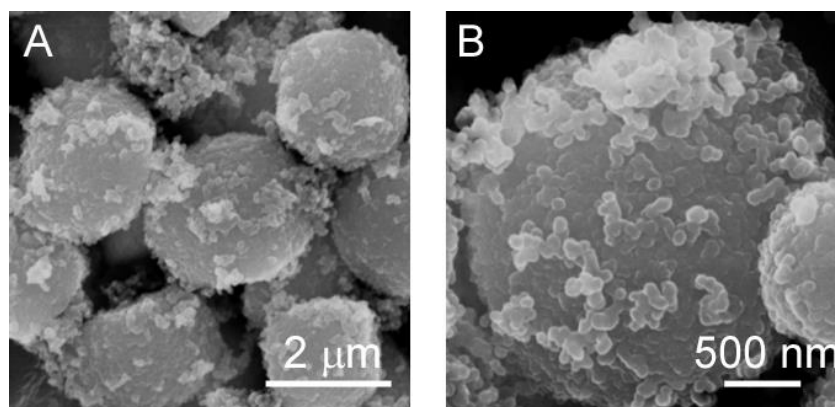


Figure A5. Scanning electron micrographs (SEM) of a partially crystalline SSZ-13 sample taken after 42 h of heating at 180°C. The images are replotted from the previous literature.⁽⁹⁶⁾

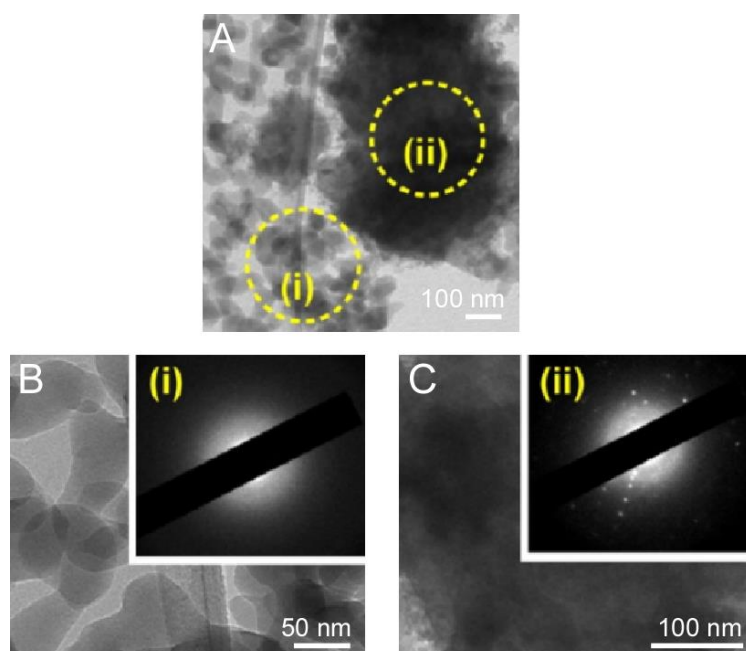


Figure A6. (A) Transmission electron micrographs (TEM) of a partially crystalline SSZ-13 sample taken after 42 h of heating at 180°C. Two population regions were found: (i) spheroidal crystals and (ii) WLP precursors. Selected area electron diffraction (SAED) patterns of regions i and ii in panel (A) demonstrate that (B) WLP precursors are amorphous and (C) spheroidal particles are crystalline, respectively. The images are replotted from the previous literature.⁶

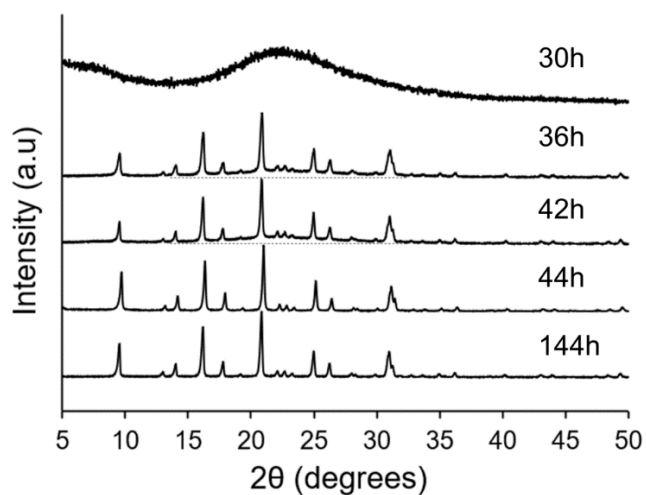


Figure A7. Powder X-ray diffraction patterns of samples extracted from a growth solution in the absence of additives at 180 °C from periodic times: 30, 36, 42, 44 and 144 h.

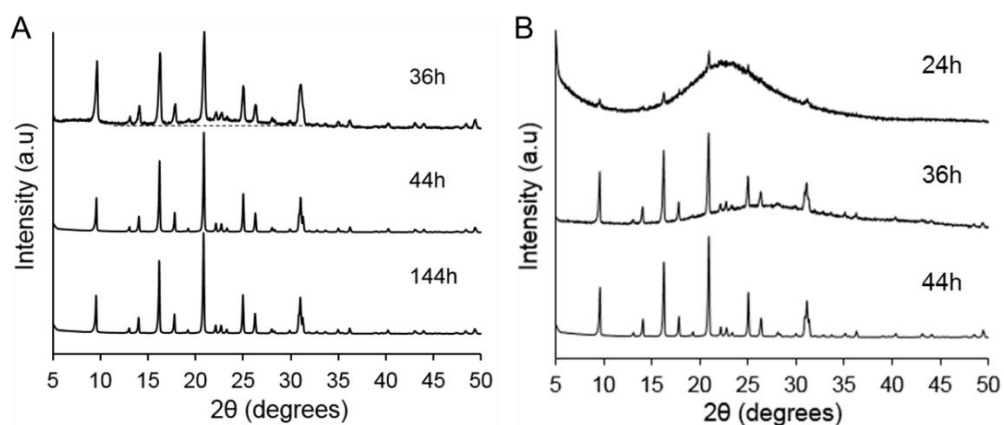


Figure A8. Powder X-ray diffraction patterns of samples extracted from a growth solution (A) in the absence of additives and (B) in the presence of PDDA with 0.5 wt.% heating at 170 °C.

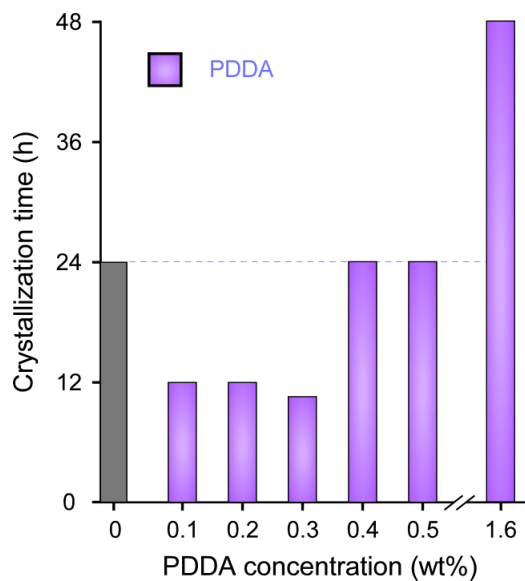


Figure A9. Relationship between SSZ-13 crystallization time and PDDA concentration at 180 °C using an alternative silicon source (LUDOX AS-40).

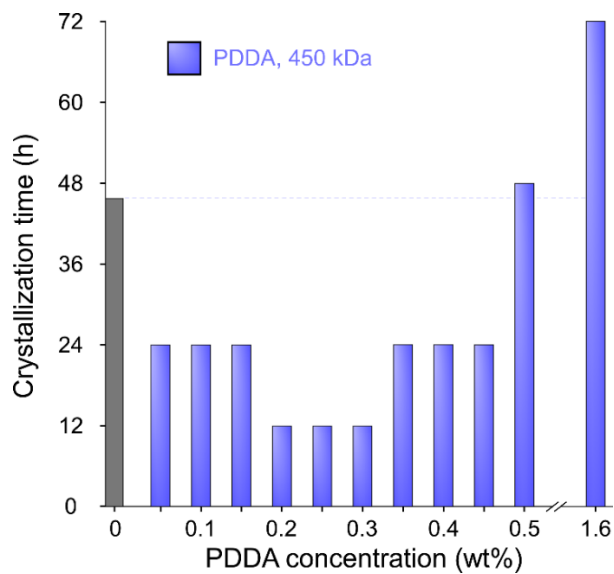


Figure A10. SSZ-13 crystallization time as a function of PDDA (450 kDa) concentration for syntheses at 180 °C using fumed silica as the silicon source.

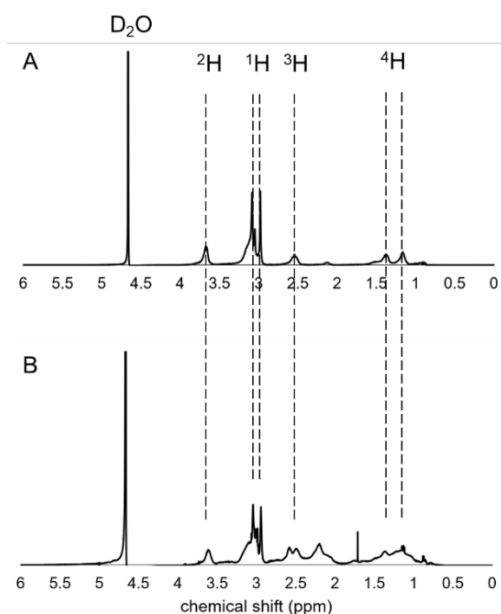


Figure A11. Liquid ^1H NMR spectrum (A) before and (B) after hydrothermal treatment using D_2O as solvent. PDDA was mixed with DI water to obtain a solution with similar pH as the synthesis condition and heated at $180\text{ }^\circ\text{C}$ for 1 day.

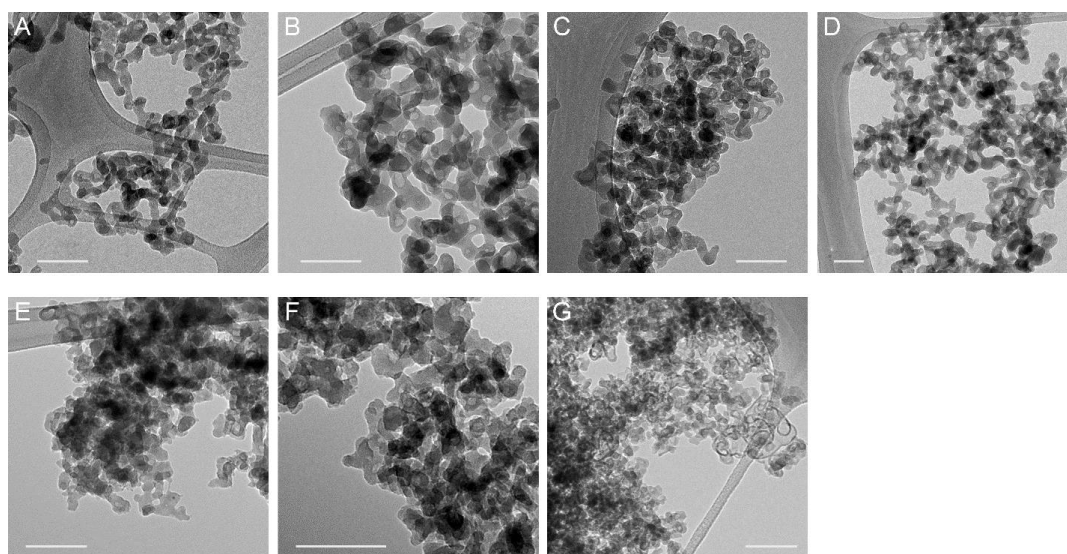


Figure A12. TEM images of SSZ-13 crystals prepared at $170\text{ }^\circ\text{C}$ using the following concentrations of additives: (A) 0wt% for 6 h; (B) 0wt% for 24 h; (C) 0.2wt% EMP for 6 h; (D) 0.2wt% EMP for 22.5 h; (E) 0.2wt% PDDA for 12 h; (F) 0.2wt% PDDA for 13 h; (G) 0.5wt% PDDA for 24h. All scale bars equal to 100 nm.

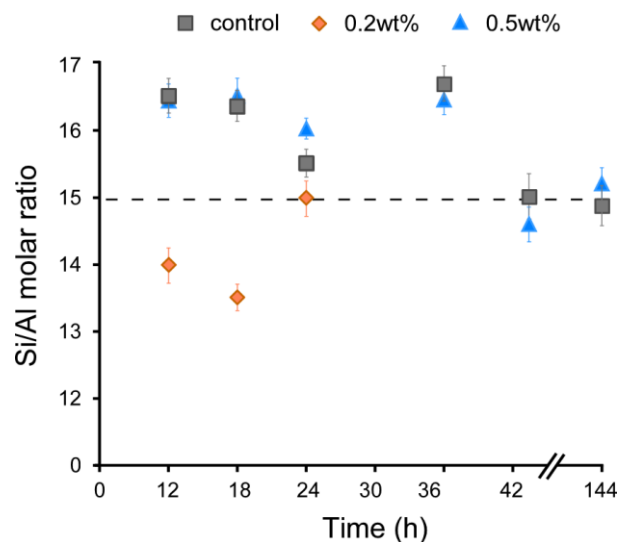


Figure A13. Elemental analysis of extracted solids using inductively coupled plasma-optical emission spectrometry (ICP-OES) for syntheses at 170 °C.

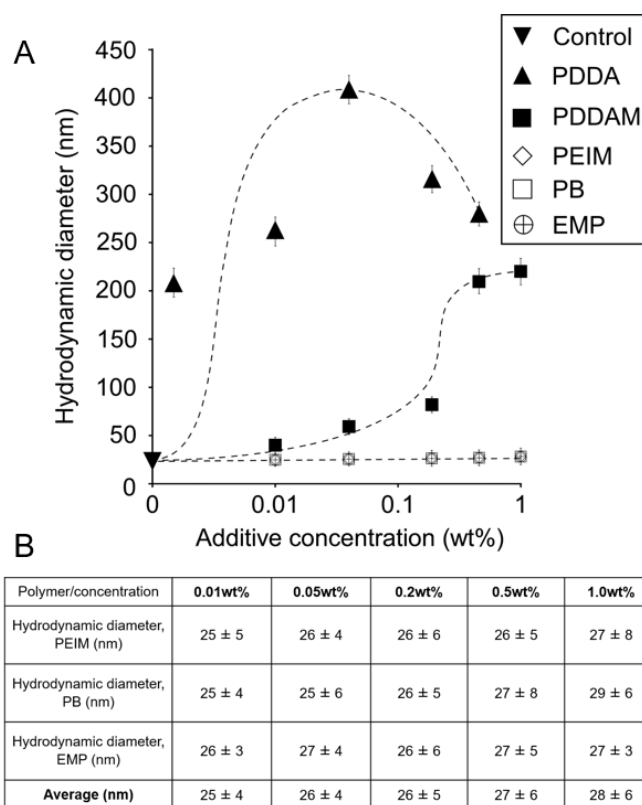


Figure A14. (A) Dynamic light scattering (DLS) measurements of colloidal silica particle size with different concentrations of polymer (PDDAM, PB and PEIM) or monomer (EMP). (B) Table for the overlapping data (PEIM, PB, and EMP) in panel A that exhibit no appreciable change in hydrodynamic diameter with increasing modifier concentration.

- Movie A1.** Time-elapsd sequence of oblique illumination microscopy (OIM) studies in clear solutions prepared from soluble silica source (sodium silicates) at a molar composition of 1 Na₂SiO₃: 1760 H₂O: 0.1 TMAda with 0.05 wt.% PDDA after 30 min mixing.
- Movie A2.** Time-elapsd sequence of oblique illumination microscopy (OIM) studies in clear solutions prepared from soluble silica source (sodium silicates) at a molar composition of 1 Na₂SiO₃: 1760 H₂O: 0.1 TMAda with 0.5 wt.% PDDA after 1h mixing.
- Movie A3.** Time-elapsd sequence of oblique illumination microscopy (OIM) studies in clear solutions prepared from soluble silica source (sodium silicates) at a molar composition of 1 Na₂SiO₃: 1760 H₂O: 0.1 TMAda with 0.05 wt.% EMP after 1h mixing.

Appendix B Supplementary Information for Chapter 3

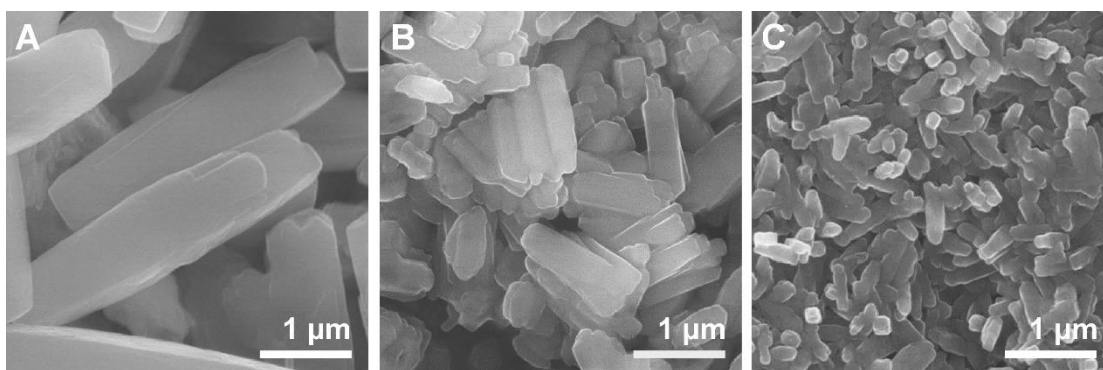


Figure B1. Scanning electron micrographs of conventional zeolite H-ZSM-11 samples listed in Table B1 with different crystal sizes: (A) MEL-C₁, (B) MEL-C₂, and (C) MEL-C₃, respectively.

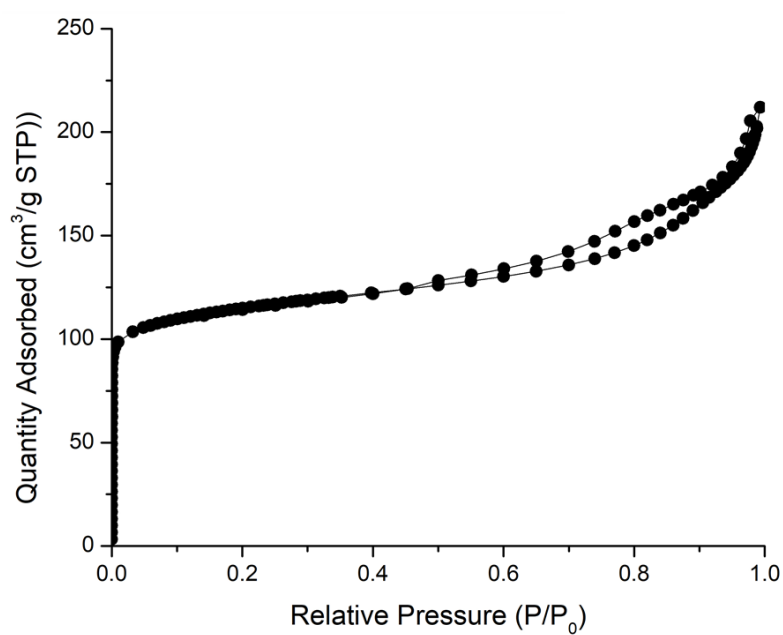


Figure B2. Nitrogen adsorption/desorption isotherm for the finned ZSM-11 sample prepared by a one-pot synthesis (sample MEL-F₁ in Table B1).

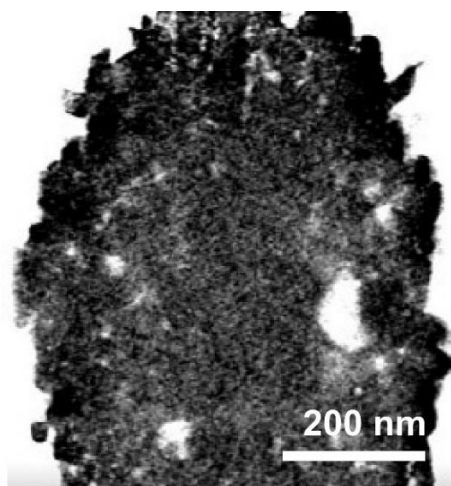


Figure B3. Transmission electron microscopy (TEM) tomography reveals the presence of isolated mesopores within the interior of finned ZSM-11 particles prepared via a one-pot synthesis (sample MEL-F₁).

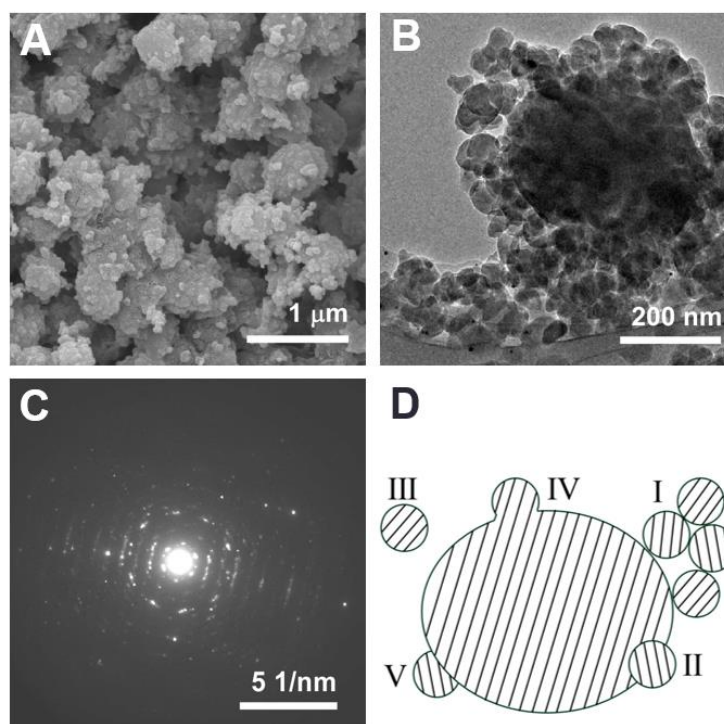


Figure B4. (A) Scanning electron microscopy (SEM) shows a typical “blackberry” morphology of MFI aggregates. (B) Transmission electron microscopy (TEM) shows clusters of small nanoparticles. (C) SAED pattern of a particle from the one-pot MFI synthesis reveals a polycrystalline sample. (D) An idealized scheme of a blackberry zeolite where the lines indicate crystallographic orientation.

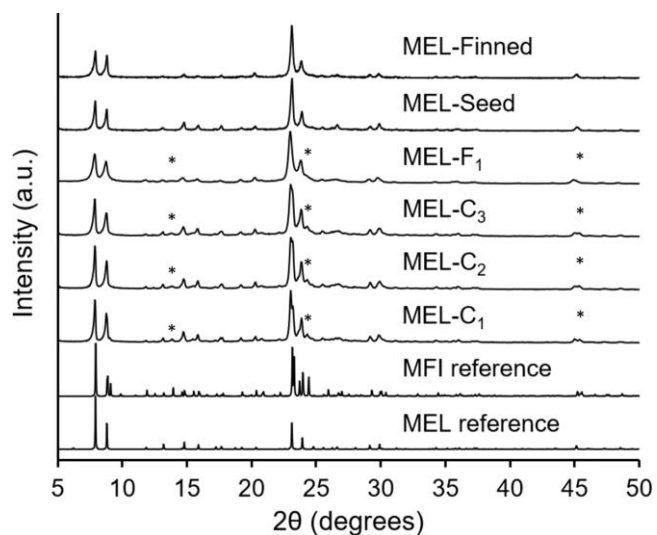


Figure B5. Powder X-ray diffraction patterns show that all as-synthesized ZSM-11 samples prepared for catalytic testing are fully crystalline.

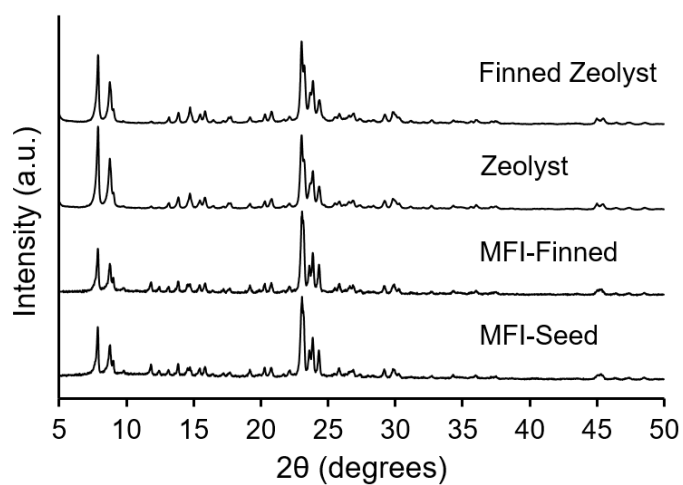


Figure B6. Powder X-ray diffraction patterns show that all as-synthesized ZSM-5 samples prepared for catalytic testing are fully crystalline.

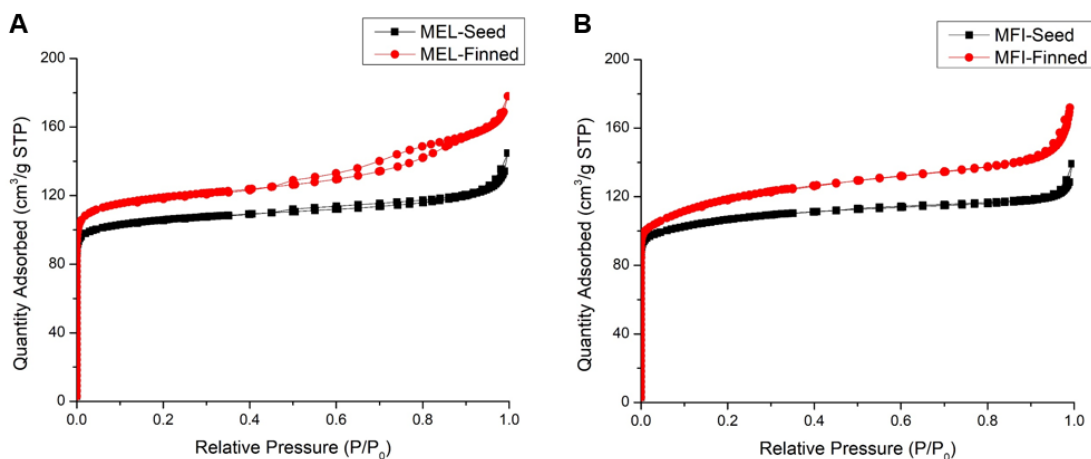


Figure B7. N_2 sorption isotherms for seed (black) and finned (red) samples of (A) H-ZSM-11 and (B) H-ZSM-5 catalysts. Each finned sample was prepared by seeded synthesis.

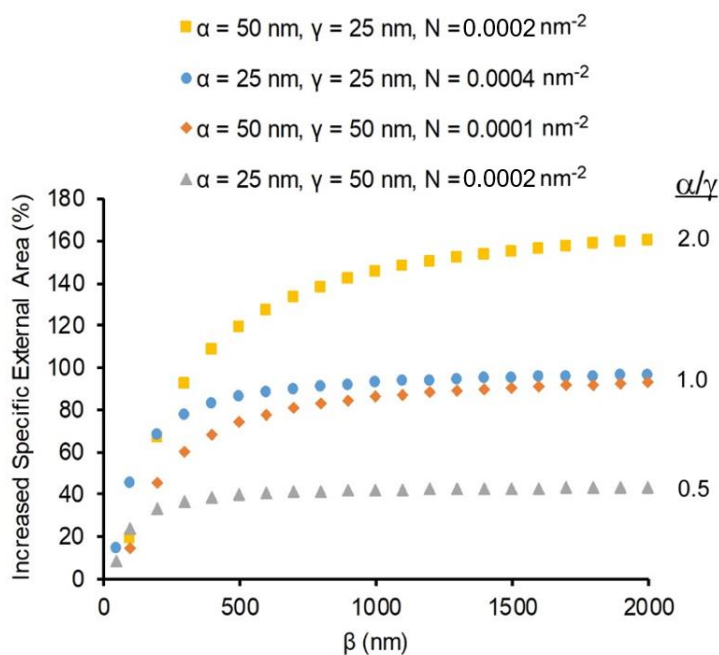


Figure B8. Calculated percent increase in specific surface area for finned zeolites compared to their original seeds as a function of seed crystal size, β . The relative increase in specific area is reported for four cases of varying fin size α and pitch γ along with the total number of fins per seed surface area, N .

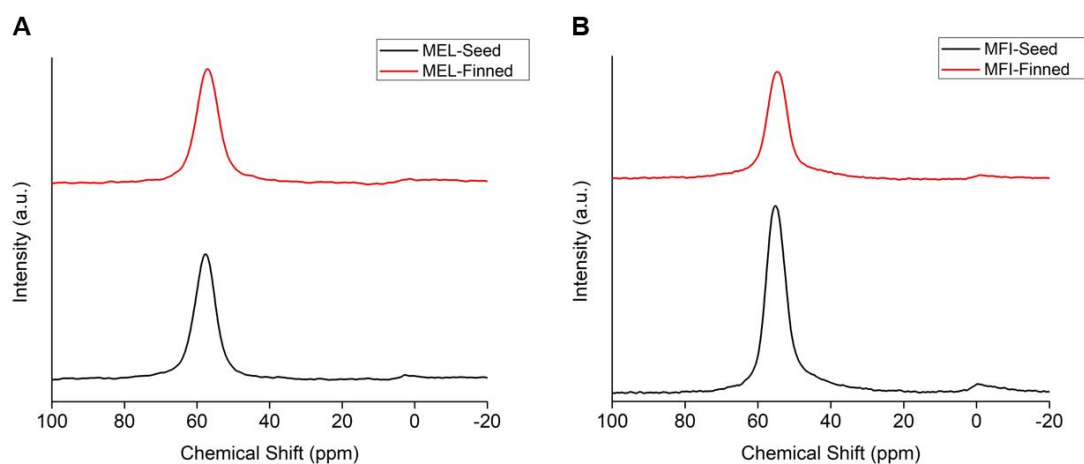


Figure B9. Solid state ^{27}Al NMR analysis for seed (black) and finned (red) samples of zeolite (A) H-ZSM-11 and (B) H-ZSM-5 catalysts. Each finned sample was prepared by seeded synthesis.

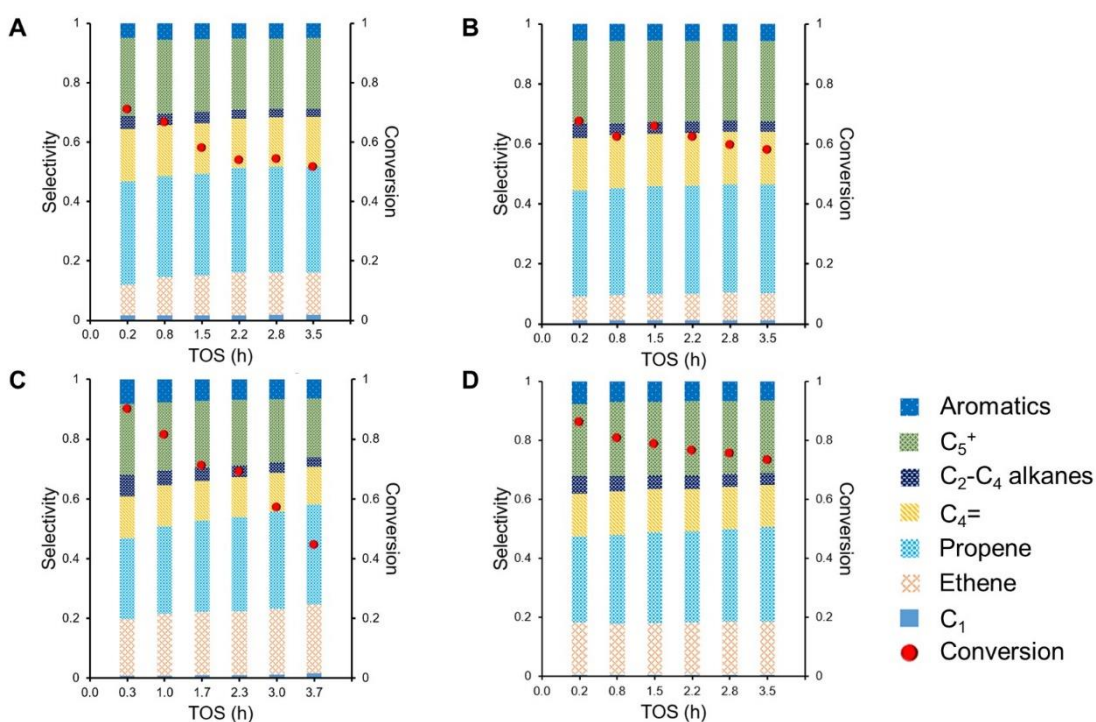


Figure B10. The results of methanol-to-hydrocarbon (MTH) reactions showing the product selectivities (bar graphs, left y-axes) and methanol conversion (red circles, right y-axes) as a function of time on stream (TOS) for the following H-form zeolites: (A) MEL-Seed, (B) MEL-Finned, (C) MFI-Seed, and (D) MFI-Finned. All reactions were performed at a weight hourly space velocity of 20 h^{-1} .

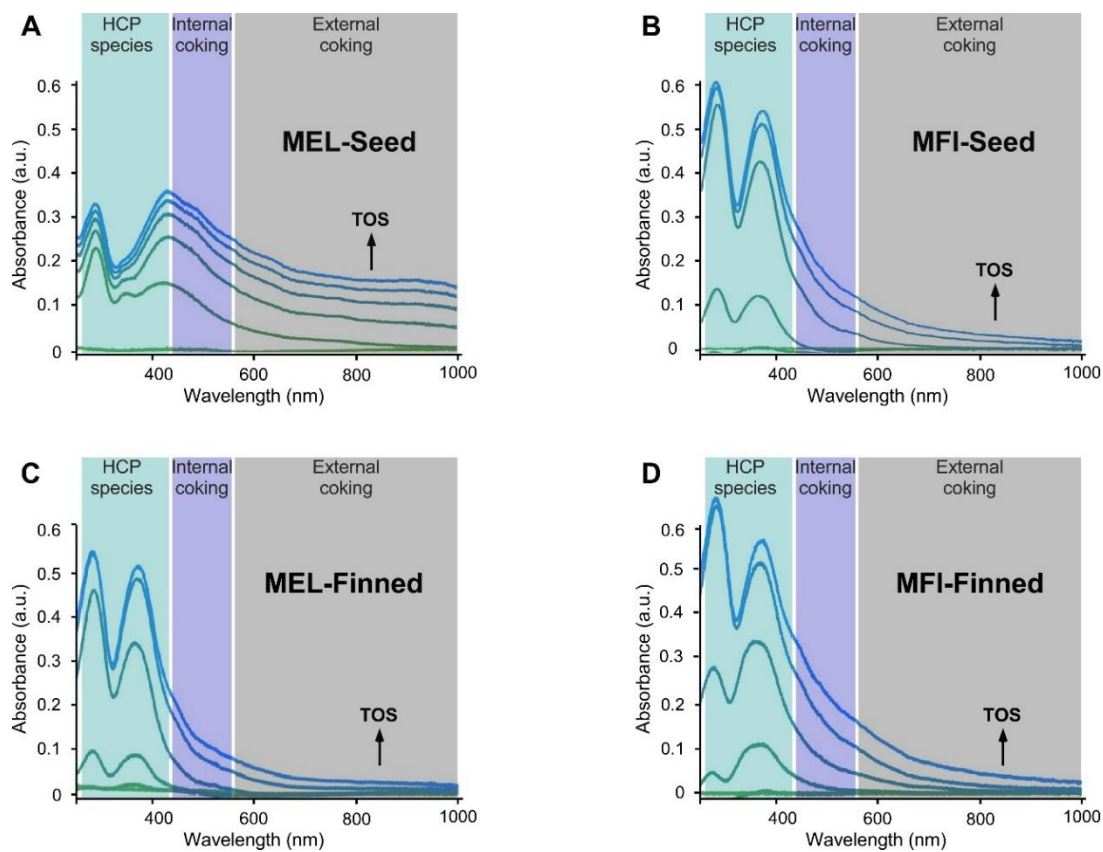


Figure B11. Operando UV-Vis diffuse reflectance spectroscopy data within 3 min TOS for zeolites (A) MEL-Seed, (B) MFI-Seed, (C) MEL-Finned, and (D) MFI-Finned. The spectra were measured in 30 s intervals.

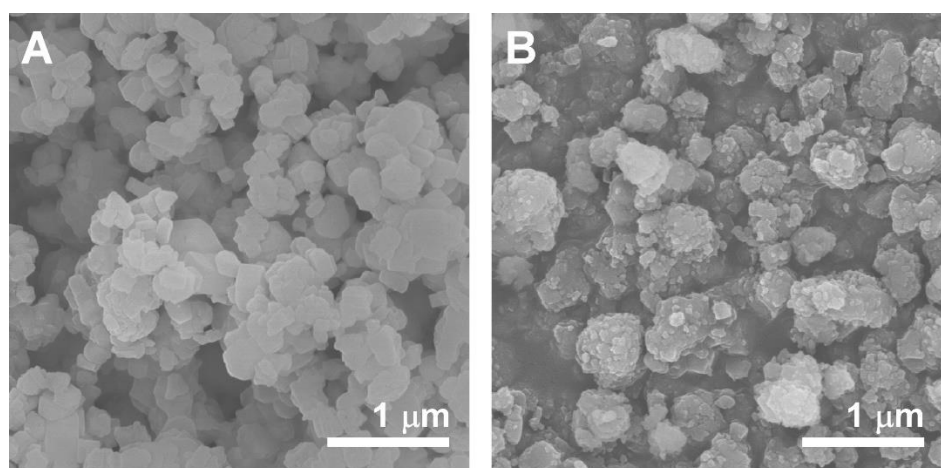


Figure B12. Scanning electron microscopy (SEM) images of (A) commercial H-ZSM-5 (Zeolyst CBV 5524G) and (B) the corresponding finned H-ZSM-5 sample prepared by secondary growth.

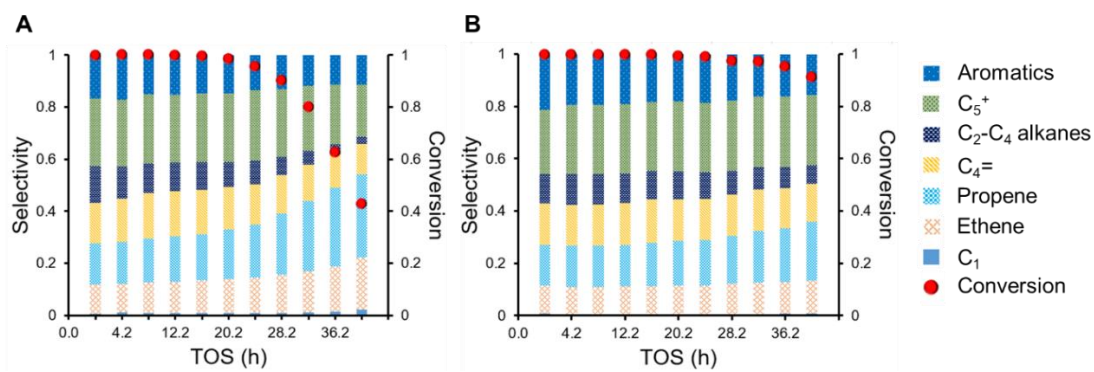


Figure B13. The results of methanol-to-hydrocarbon (MTH) reactions showing the product selectivities (bar graphs, left y-axes) and methanol conversion (red circles, right y-axes) as a function of time-on-stream (TOS) for the following H-form zeolites: (A) Zeolyst and (B) Finned Zeolyst. All reactions were performed at a weight hourly space velocity of 9 h^{-1} .

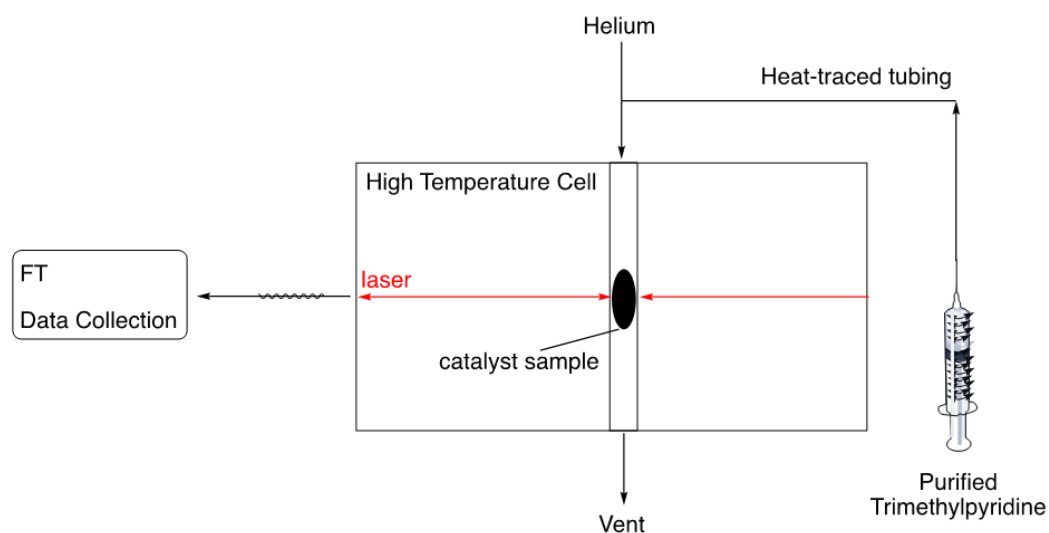


Figure B14. Simplified schematic of FTIR spectroscopy where 2,4,6-trimethylpyridinium is constantly flowed into the cell to be dosed onto the catalyst sample.

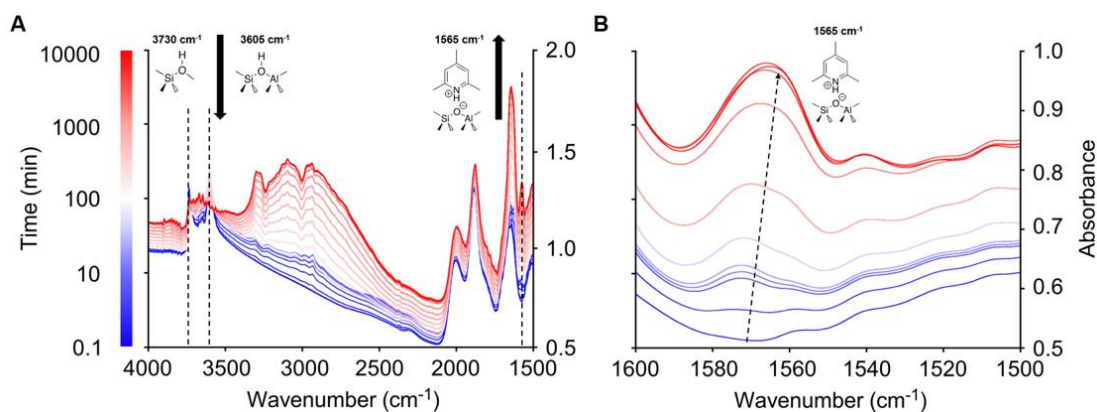


Figure B15. (A) Raw FTIR spectra of a catalyst sample highlighting peaks of interest. The percentage of Brønsted acid sites titrated corresponds to integration of 1565 cm^{-1} peak areas. (B) Temporal changes in the FTIR spectra showing an increased peak area at 1565 cm^{-1} over time.

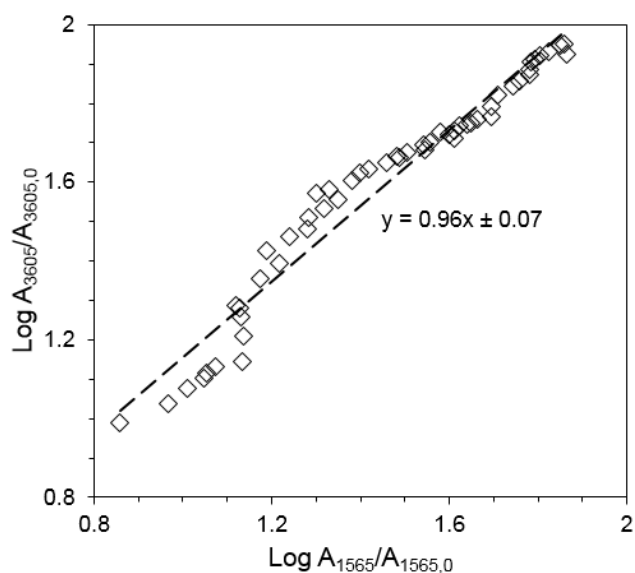


Figure B16. Parity plot showing loss of Brønsted acid sites (BAS) is linearly correlated to the increase in 2,4,6-trimethylpyridinium ions. The parameters A_x and $A_{x,0}$ are peak areas of the FTIR spectra at a particular time and the initial time, respectively, where $x = 1565\text{ cm}^{-1}$ for TMPyr-occupied BAS and $x = 3605\text{ cm}^{-1}$ for vacant BAS.

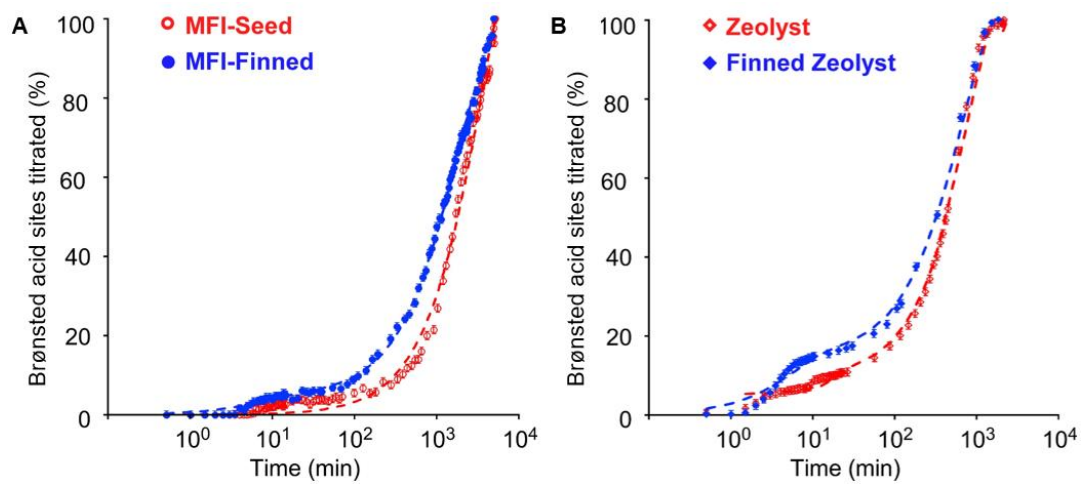


Figure B17. Time-resolved titration of Brønsted acid sites for (A) H-ZSM-5 seed/finned samples and (B) Zeolyst (CBV 5524G)/finned Zeolyst samples.

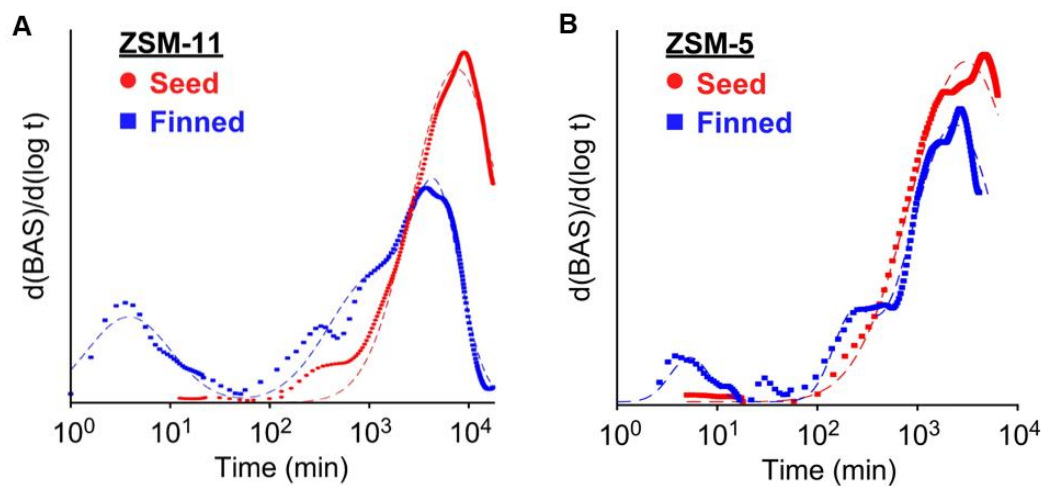


Figure B18. Differential plot of titrated Brønsted acid sites in (A) H-ZSM-11 seed/finned samples and (B) H-ZSM-5 seed/finned samples.

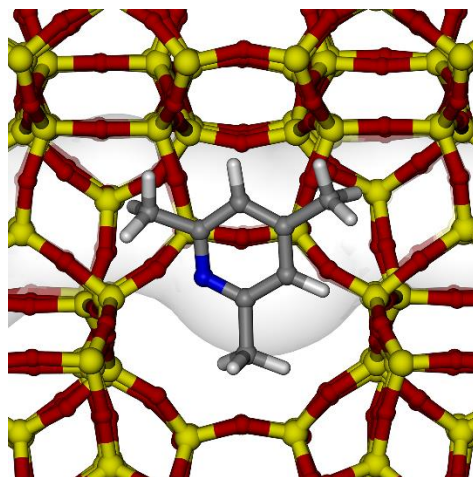


Figure B19. Snapshot from an SMD simulation (Supplementary Video B5) showing TMPyr within a silicalite-1 (MFI) straight channel.

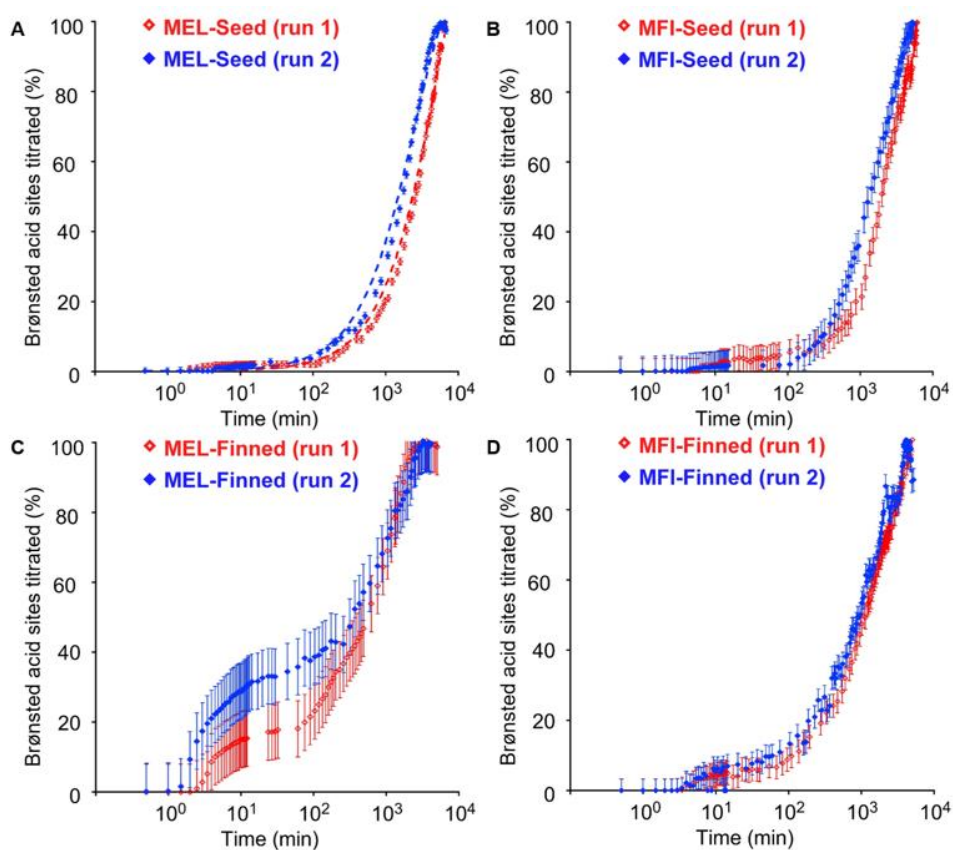


Figure B20. Uptake data of (A) MEL-Seed, (B) MFI-Seed, (C) MEL-Finned and (D) MFI-Finned from Brønsted acid site (BAS) titrations by 2,4,6-trimethylpyridine for two separate runs indicating run-to-run repeatability.

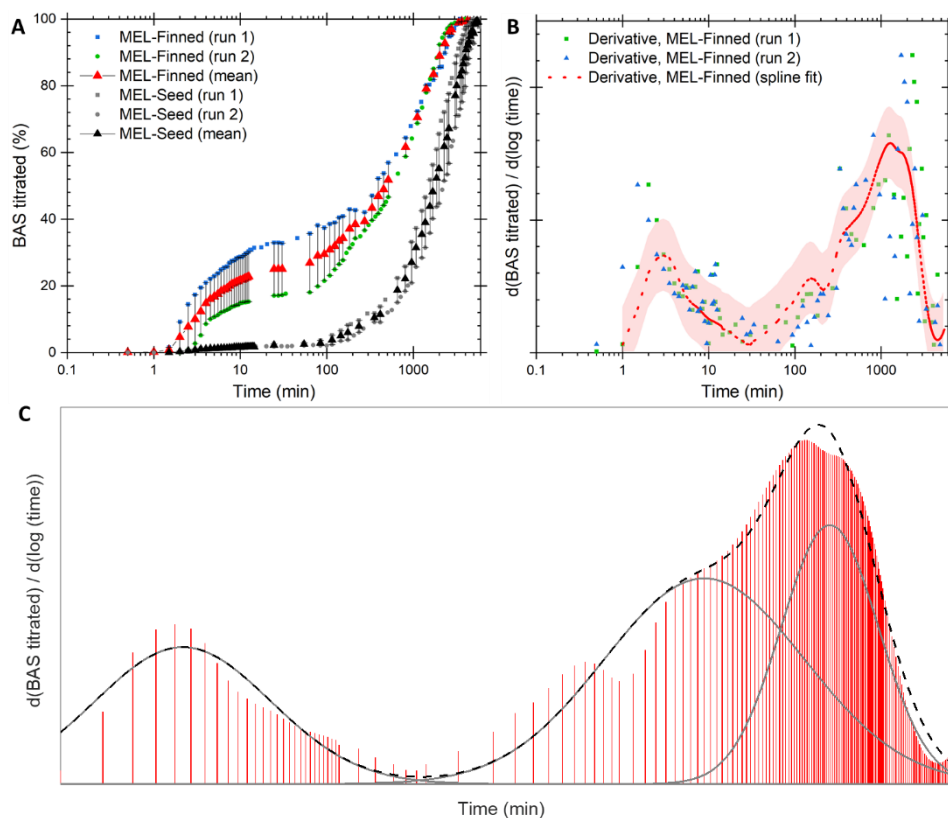


Figure B21. (A) Time-resolved Brønsted acid sites titrated in the MEL-Seed and MEL-Finned samples for two separate runs. (B) Derivative of Brønsted acid sites titrated for the MEL-Finned sample, with colors corresponding to the plots in panel A.

Table B1. Characterization of conventional and finned ZSM-11 samples prepared by a one-pot synthesis.

Sample	BET S_A (m^2/g)	S_{ext} (m^2/g)	V_{micro} (cm^3/g)	Si/Al (ICP)	Si/Al (XPS)	NH ₃ -TPD ($\mu mol/g$)
MEL-C ₁	448	109	0.13	24.6	22	621
MEL-C ₂	434	79	0.14	19.3	25	864
MEL-C ₃	429	99	0.13	22.5	21	803
MEL-F ₁	431	116	0.13	19.0	22	893

Table B2. Synthesis conditions for conventional and finned ZSM-11 samples by a one-pot synthesis.

Sample	Size (nm)	Molar Composition of Growth Mixture					T (°C)	Time (day)
		Al ₂ O ₃	SiO ₂	Na ₂ O	H ₂ O	TBAOH		
MEL-C ₁	750	2.5	100	4	2000	20	160	1
MEL-C ₂	300	2.5	100	4	1000	20	170	3
MEL-C ₃	150	2.5	100	4	600	20	170	3
MEL-F ₁ ^a	460	2.5	100	4	3000	20	160	1

a. Finned zeolite generated from a one-pot synthesis.

Table B3. Characterization of seeds and finned ZSM-11 and ZSM-5 samples prepared by seeded synthesis.

Sample	BET S_A (m^2/g)	S_{ext} (m^2/g)	V_{micro} (cm^3/g)	Si/Al (ICP)	Si/Al (XPS)	NH ₃ -TPD ($\mu mol/g$)	Al _{octahedral} (%)
MEL-Seed	408	61	0.14	43.5	37	536	2.0
MEL-Finned	447	90	0.14	40.0	38	524	2.7
MFI-Seed	405	87	0.13	29.2	35	613	7.9
MFI-Finned	438	152	0.12	32.6	37	588	7.7

Table B4. Synthesis conditions for seeds and growth solutions for finned ZSM-11 and ZSM-5 samples prepared by seeded synthesis.

Sample	Molar Composition of Growth Mixture					T (°C)	Time (day)
	Al ₂ O ₃	SiO ₂	M ₂ O ^a	H ₂ O	OSDA ^b		
MEL-Seed ^c	1	100	10	4000	10	160	3
MEL-Finned	1	90	11.9	3588	27.3	120	2
MFI-Seed	1.67	100	4	2500	15	170	2
MFI-Finned	1	63	1	3320	20	100	1

a. "M" = alkali ion; Na₂O is used for ZSM-5 and K₂O is used for ZSM-11, respectively.

b. TPAOH is used for ZSM-5 and DAO is used for ZSM-11.

c. Using 2 wt.% ZSM-11 calcined seed (relative to the SiO₂ content in the synthesis mixture).

Table B5. Characterization of commercial and finned H-ZSM-5 catalysts.

Sample	BET S_A (m^2/g)	S_{ext} (m^2/g)	V_{micro} (cm^3/g)	Si/Al (ICP)	Si/Al (XPS)	$\text{NH}_3\text{-TPD}$ ($\mu\text{mol}/\text{g}$)	$\text{Al}_{\text{octahedral}}$ (%)
Zeolyst	427	169	0.11	27.3	22.3	690	5.3
Finned Zeolyst	440	170	0.11	32.9	30.9	514	4.0

Table B6. Kinetic Monte Carlo rate constants for benzene transport in silicalite-1 at 300 K.

$k_{i \rightarrow j}$ ^a	s^{-1}
$k_{I \rightarrow Z}$	1.1×10^6
$k_{Z \rightarrow I}$	1.6×10^8
$k_{I \rightarrow S}$	2.3×10^6
$k_{S \rightarrow I}$	2.7×10^8

a. Subscripts denote transition from adsorption site i to j , where the indices specify sites in the straight pore (S), sinusoidal channel (Z), and at the intersections (I) of both pores in silicalite-1.

Table B7. Kinetic Monte Carlo (kMC) simulation results for benzene transport in silicalite-1 at 300 K for seed and finned crystals with linear dimensions of $\alpha \approx 50$ nm and $\beta \approx 500$ nm.

Model	γ (nm)	Fin surface density (nm^{-2})	Specific external surface area ($\text{m}^2 \text{g}^{-1}$)	$\langle r \rangle$ (nm)	$\langle \tau \rangle$ (s)
Seed	-	-	6.7	138	1.9×10^{-5}
Finned	4	3.3×10^{-4}	19.1	56	7.6×10^{-6}
Finned	10	2.6×10^{-4}	17.2	58	7.9×10^{-6}
Finned	25	1.5×10^{-4}	13.4	88	1.2×10^{-5}
Finned	50	1.0×10^{-4}	11.6	92	1.3×10^{-5}

- Movie B1.** Sequence of z stacks from electron tomography of the finned MEL-F₁ sample prepared by a one-pot synthesis, corresponding to the snapshot used in Figure 3.1c.
- Movie B2.** Sequence of z stacks from electron tomography of the MEL-Finned sample prepared by seeded growth, corresponding to snapshots at various positions along the c-direction used in Figure 3.2i.
- Movie B3.** Sequence of z stacks from electron tomography of the MFI-Finned sample prepared by seeded growth, corresponding to snapshots at various positions along the c-direction used in Figure 3.2j.
- Movie B4.** An SMD trajectory of TMPyr cage hopping in a straight channel of MEL (silicalite-2), viewed along the [001] direction of the framework
- Movie B5.** An SMD trajectory of TMPyr cage hopping in a straight channel of MFI (silicalite-1), viewed along the [100] direction of the framework.

Appendix C Supplementary Information for Chapter 4

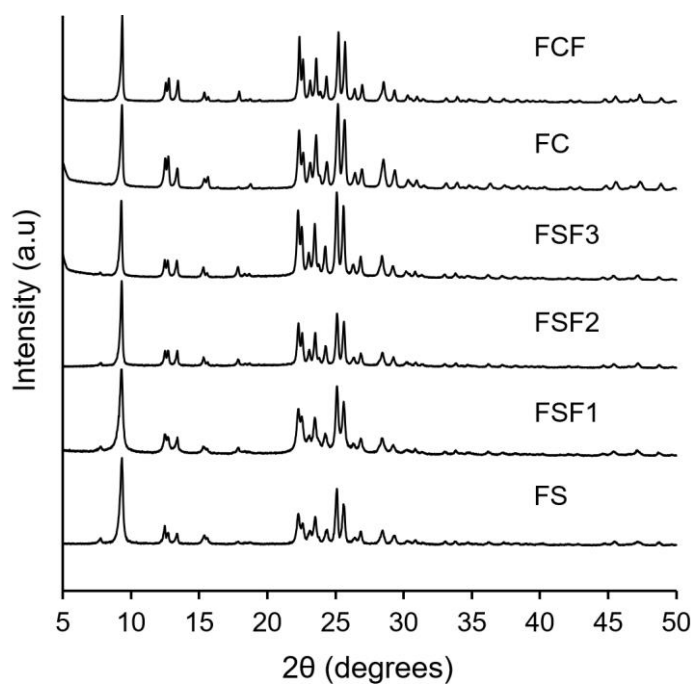


Figure C1. Powder X-ray diffraction patterns of all as-synthesized ferrierite zeolite samples (see Table S1 for synthesis conditions and Table 4.1 in the manuscript for physicochemical properties of each sample).

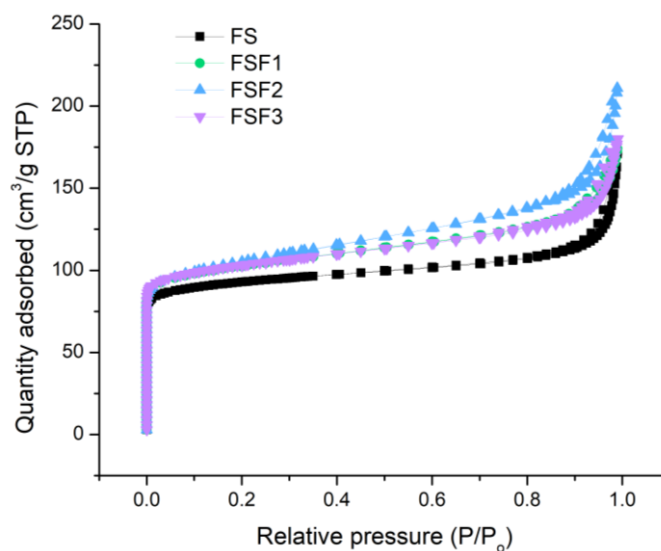


Figure C2. Nitrogen adsorption/desorption isotherms for the seed (FS) and corresponding finned ferrierite samples (FSF1, FSF2, and FSF3).

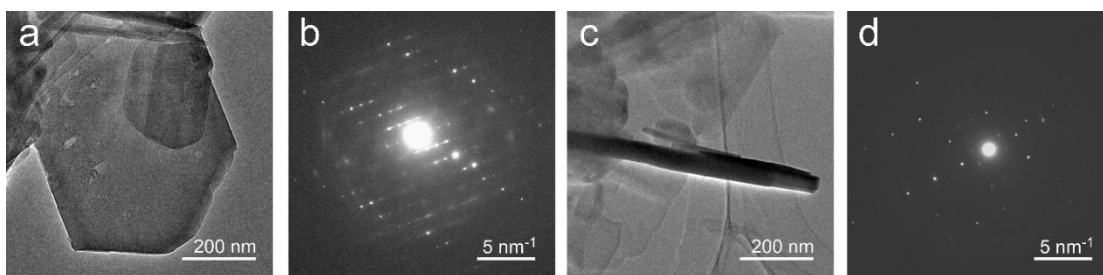


Figure C3. TEM images of sample FS viewed (a) facing the sheet (normal to the [100] direction) and (c) from the edge. (b and d) SAED patterns of respective images.

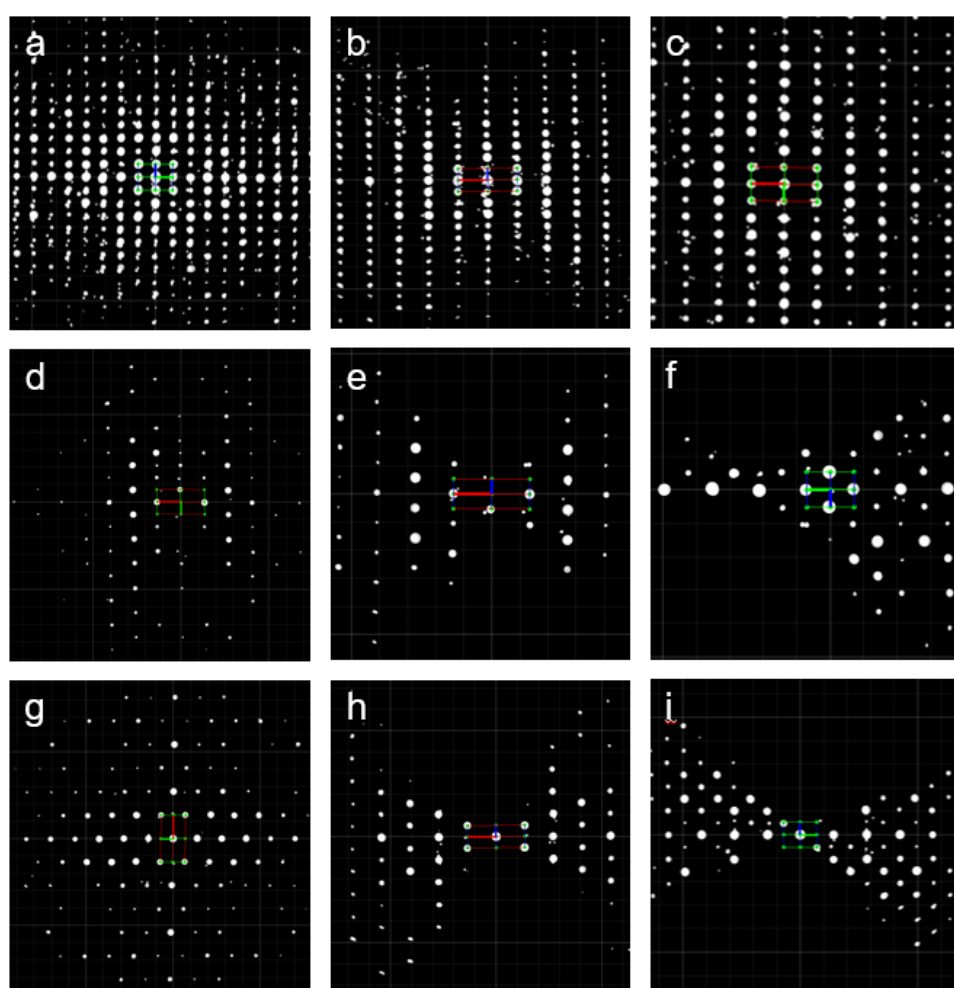


Figure C4. 3D reconstructed reciprocal lattice viewed from (a) a^* , (b) b^* and (c) c^* direction. 2D slice (d) $(hk1)$, (e) $(h1l)$, (f) $(1kl)$, (g) $(hk0)$, (h) $(h0l)$ and (i) $(0kl)$ face in the reciprocal lattice confirm the $Immm$ space group of the FER framework for the FSF2 sample. The corresponding unit cell parameter is $a = 19.11 \text{ \AA}$, $b = 14.45 \text{ \AA}$, $c = 7.40 \text{ \AA}$, $\alpha = 90.4^\circ$, $\beta = 89.5^\circ$, $\gamma = 89.5^\circ$. See Movie S4 for the whole 3D reconstructed reciprocal lattice.

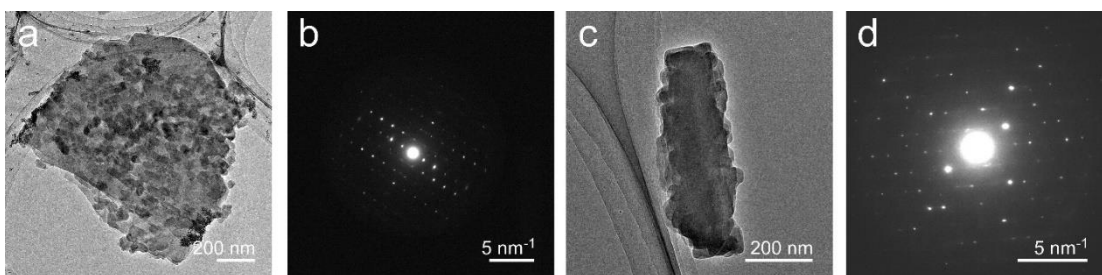


Figure C5. TEM images of sample FSF2 in two orientations: (a) facing the sheet (normal to the [100] direction); and (c) from the edge. SAED patterns of respective images (b, d) reveal that FSF2 is a single crystal.

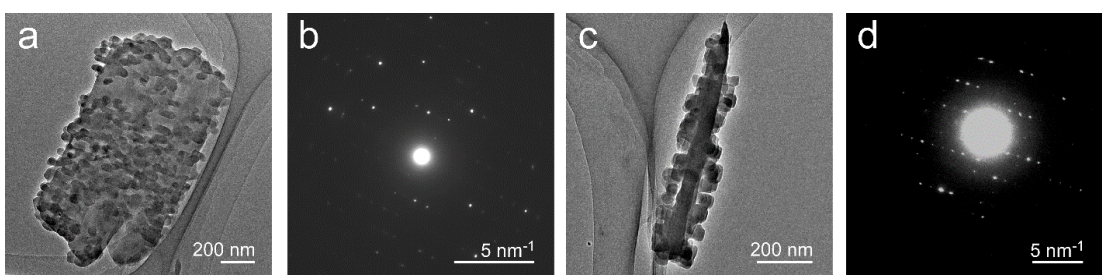


Figure C6. TEM images of sample FSF3 in two orientations: (a) facing the sheet (normal to the [100] direction); and (c) from the edge. SAED patterns of respective images (b and d) reveal that FSF3 is a single crystal.

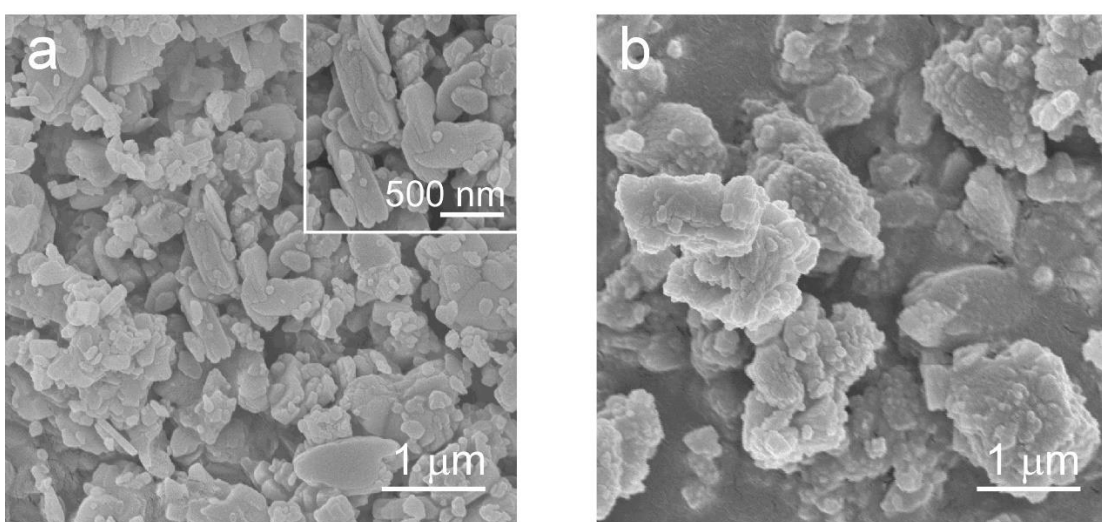


Figure C7. Scanning electron micrographs of samples (a) FC and (b) corresponding finned FCF.

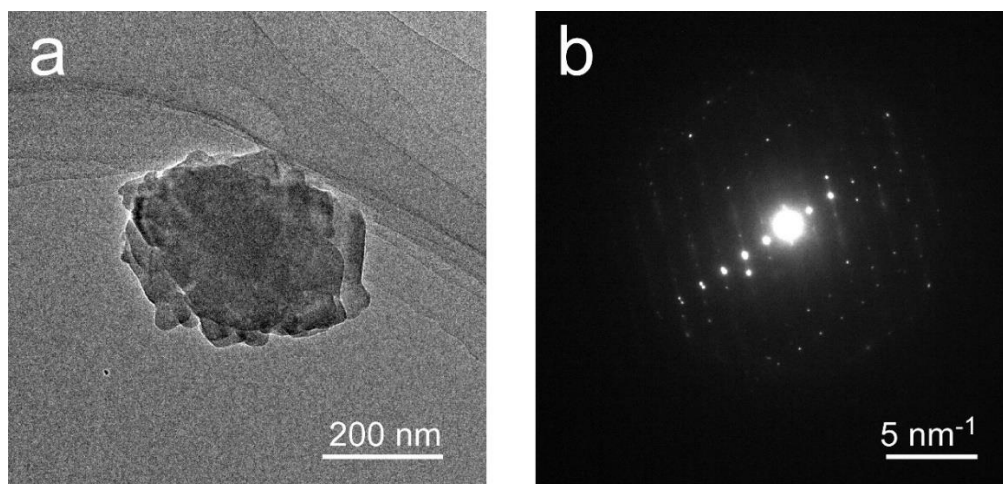


Figure C8. (a) Transmission electron micrograph of FCF. SAED patterns of respective images (b) reveal that FCF is a single crystal.

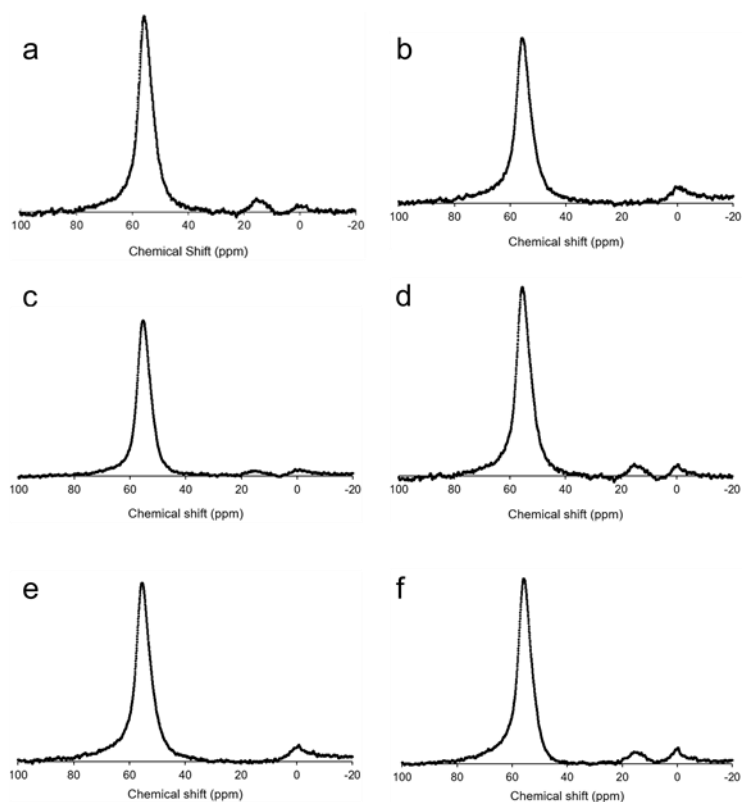


Figure C9. Solid state ^{27}Al MAS NMR analysis for samples (a) FS, (b) FSF1, (c) FSF2, (d) FSF3, (e) FC, and (f) FCF. See Table C1 for synthesis conditions and Table 4.1 for physicochemical properties of each sample (including the analysis of extra-framework Al species from these spectra).

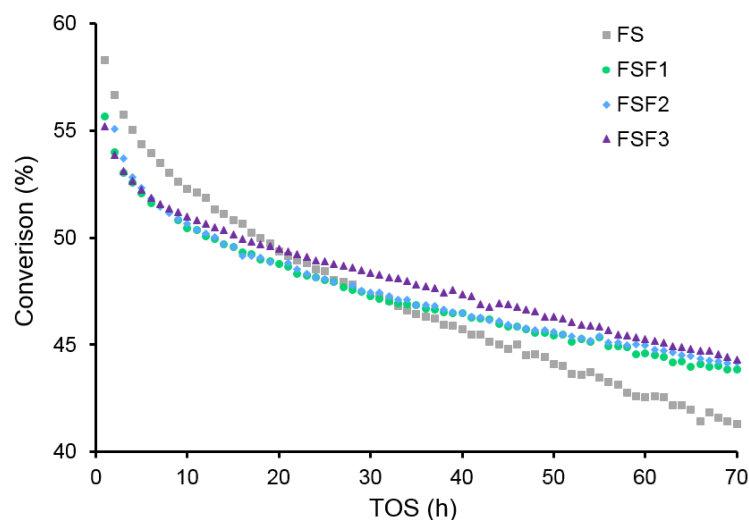


Figure C10. Conversion of 1-butene as a function of time on stream (TOS) for the seed (FS, square symbols) and finned ferrierite samples (FSF1, FSF2, and FSF3).

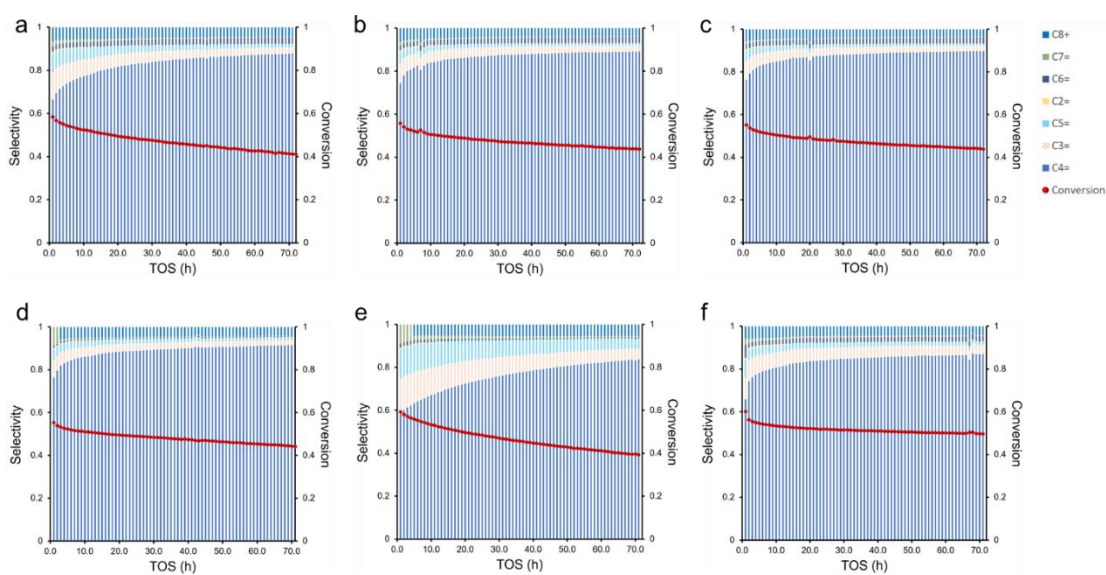


Figure C11. The results of isomerization of 1-butene reaction showing the product selectivities (bar graphs, left y-axis) and 1-butene conversion (red circles, right y-axis) as a function of time on stream (TOS) for the following H-form catalysts: (a) FS, (b) FSF1, (c) FSF2, (d) FSF3, (e) FC, and (f) FCF.

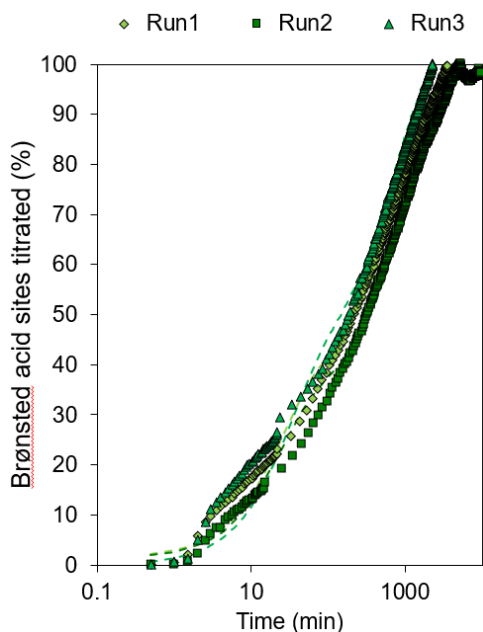


Figure C12. Titration of Brønsted acid sites (BAS) by 2,3-dimethylpyridine in sample FS over time. Three runs were performed to assess the reproducibility of the technique measured BAS titration within 2.5% error.

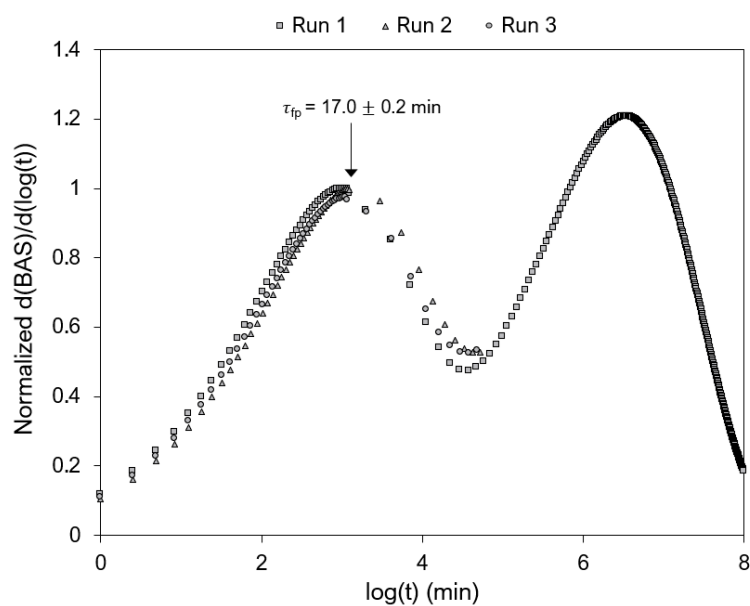


Figure C13. Derivative of Brønsted acid sites (BAS) titration by 2,3-dimethylpyridine on FSF2 over time, normalized by each run's respective peak at fast time-scale (τ_{fp}). Technique reproducibly measures τ_{fp} within 1.2% error.

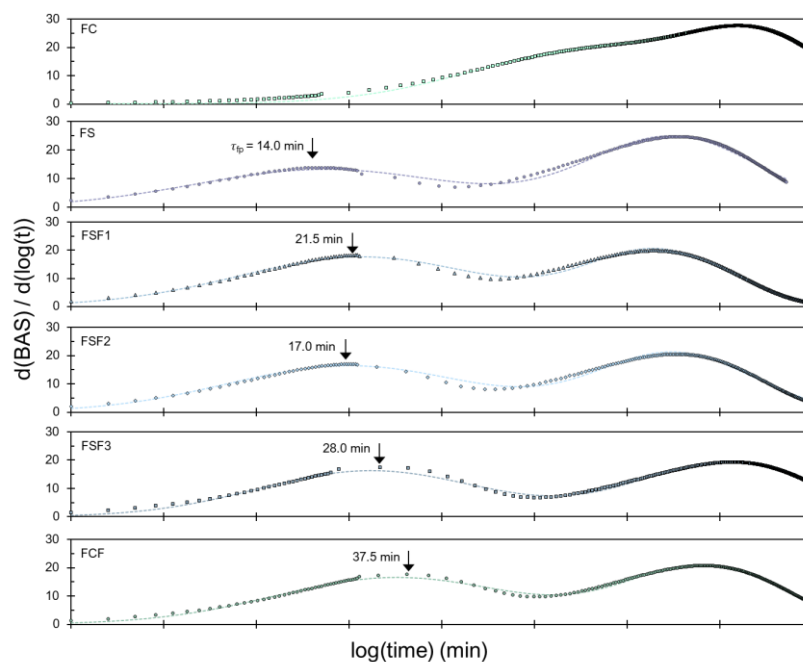


Figure C14. Derivative of Brønsted acid sites (BAS) titration by 2,3-dimethylpyridine over time. The area under the peaks represents the cumulative amount of Brønsted acid sites titrated at different time point, with the first peak's maxima indicated by τ_{fp} , or peak at fast time-scale. The derivative plot was obtained via the following procedure - fitting smoothing spline function over BAS titration over time, taking discrete derivative between each point, fitting the derivative plot with peak fitting function in MATLAB.

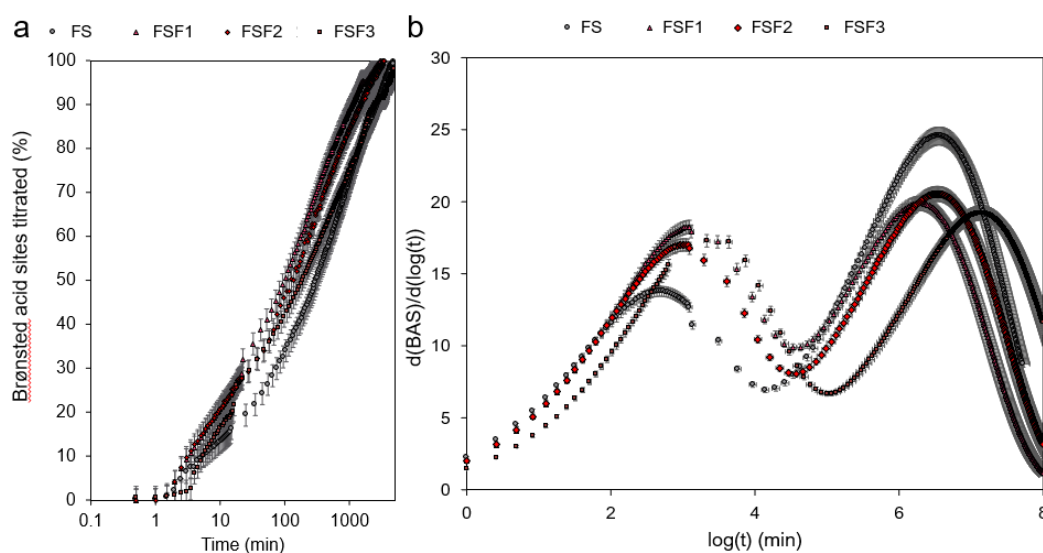


Figure C15. (a) Titration of Brønsted acid sites (BAS) by 2,3-dimethylpyridine in seed and finned ferrierite samples (FS, FSF1, FSF2 and FSF3) over time. (b) Derivative of BAS titration.

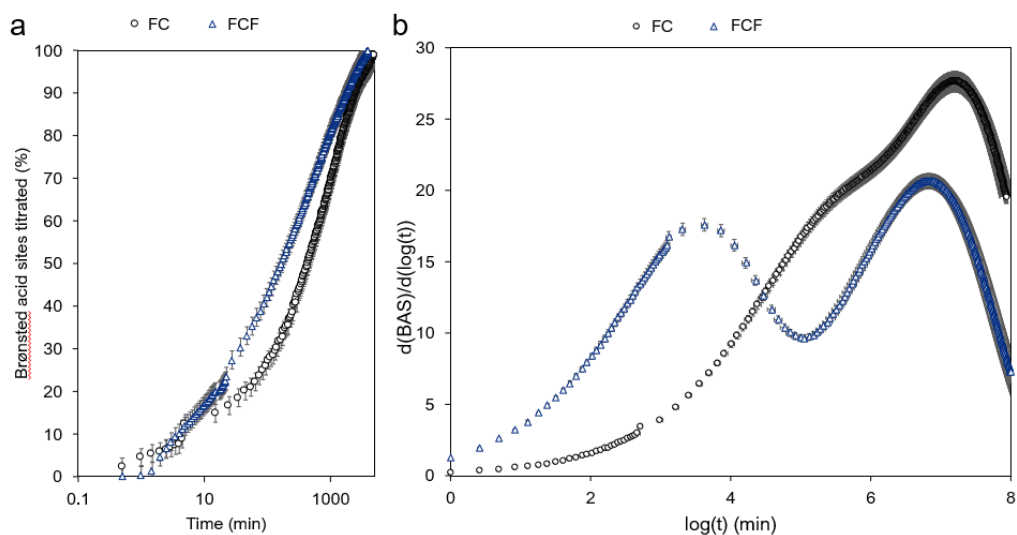


Figure C16. (a) Titration of Brønsted acid sites (BAS) by 2,3-dimethylpyridine in FC and FCF over time. (b) Derivative of BAS titration.

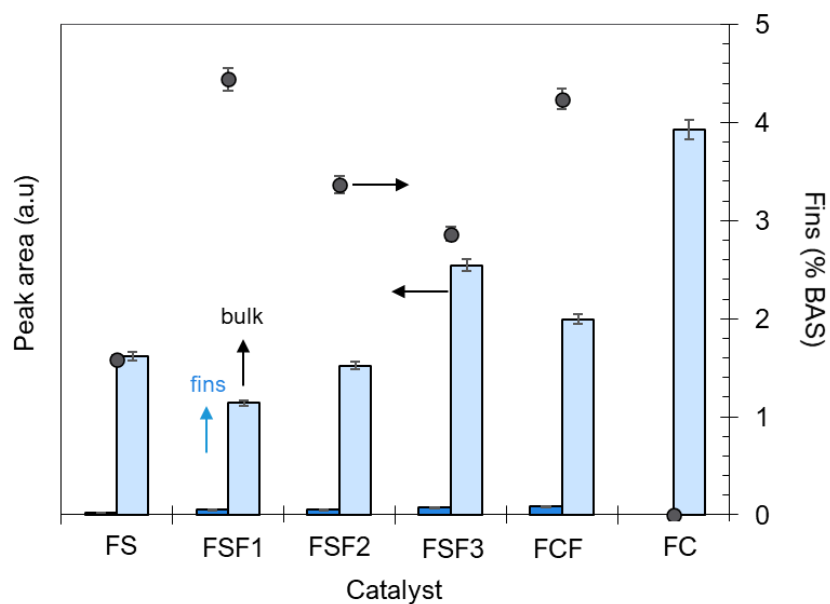


Figure C17. Absolute and relative peak areas of BAS titrated in fins and bulk catalyst. Technique reproducibly measures percentage of BAS uptake within 0.25% error. Error bars were computed from the sampling of three separate runs of different samples from the same synthesis batch.

Table C1. Synthesis conditions and growth solution of seed and finned ferrierite samples prepared by seeded synthesis.

Sample	Molar Composition of Growth Mixture						T (°C)	Time (day)
	Al ₂ O ₃	SiO ₂	Na ₂ O	K ₂ O	H ₂ O	OSDA ^a		
FS	1	20	2.4	0.6	750	5	165	2
FSF1	0.71	20	6.2	n.a.	800	14	120	1
FSF2	0.71	20	6.2	n.a.	800	14	130	1
FSF3	0.71	20	6.2	n.a.	800	14	140	1
FCF	0.71	20	6.2	n.a.	800	14	130	1

a. cyclohexylamine (CHA) is used as OSDA for FS and pyrrolidine (Pyr) is used for FSF1, FSF2, FSF3, and FCF.

Movie C1. Sequence of z stacks from electron tomography of the FSF2 sample prepared by seeded growth, corresponding to snapshots at various positions along the direction labelled in Figure 4.3e of the manuscript.

Movie C2. Sequence of z stacks from electron tomography of the FSF3 sample prepared by seeded growth, corresponding to snapshots at various positions along the direction labelled in Figure 4.3f of the manuscript.

Movie C3. Sequence of z stacks from electron tomography of the FSF1 sample prepared by seeded growth.

Movie C4. 3D electron diffraction pattern of the FS sample where the compilation of images within the movie shows scattering at different angles of rotation.

Appendix D Supplementary Information for Chapter 5

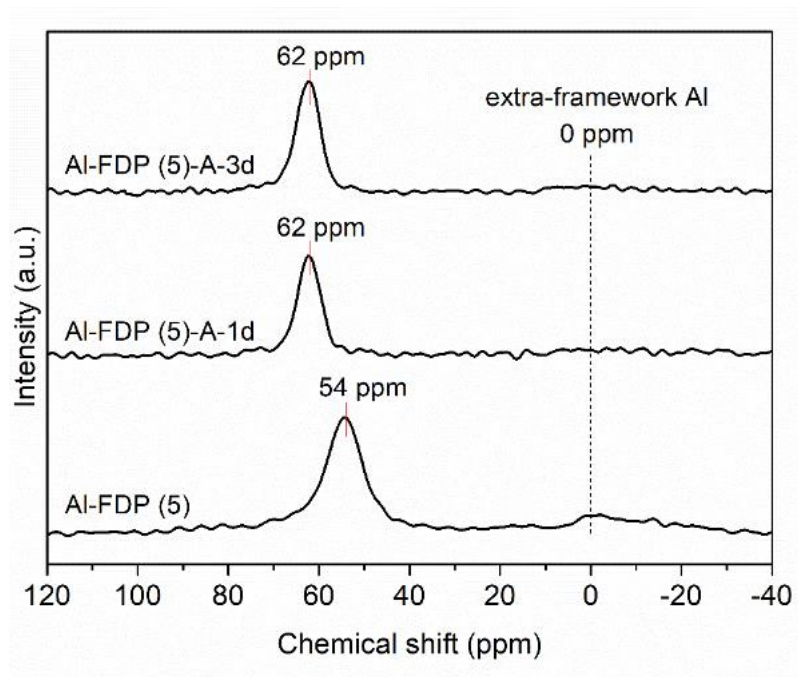


Figure D1. ^{27}Al MAS NMR of (a) Al-FDP (5), (b) Al-FDP (5)-A-1d, and (c) Al-FDP (5)-A-3d. Note that samples (b) and (c) are post-annealed for 1 and 3 days respectively. The intensity of resonance assigned to extra-framework Al species at ca. 0 ppm decreased after annealing, indicating the depletion of extra-framework Al species.